# Performance Bounds for Estimating Time Delay and Radial Velocity With Multiple Broadband Frequency-Modulated Pulses

D. A. Abraham

Technical Report
**APL-UW TR 2303**
August 2023

**Applied Physics Laboratory**
1013 NE 40th Street

**University of Washington**
Seattle, Washington 98105-6698

*Contract N00024-21-D-6400 under task order N00024-22-F-8714*

## Acknowledgements

This report was sponsored by the Office of Naval Research, Code 321US, Undersea Signal Processing. Funding was provided through Naval Sea Systems Command contract N00024-21-D-6400 under task order N00024-22-F-8714. The author thanks Dr. D. Hague for reviewing this report.

## Abstract

Estimation of the location and motion of an object of interest is one of the primary inferential objectives in underwater acoustical remote sensing. In active sensing systems, this often begins with estimation of range through time delay and radial velocity by exploiting the Doppler effect. In systems that project a sequence of pulses, radial velocity can also be estimated from multiple time-delay measurements using waveforms insensitive to Doppler. The focus of this report is on performance bounds for estimation of time delay and radial velocity when using multiple frequency-modulated pulses that are not restricted to being narrowband. An emphasis is placed on the case of estimating radial velocity when time delay is also unknown while using combinations of the basic sonar waveforms: continuous-wave (CW), linear-frequency-modulated (LFM), and hyperbolic-frequency-modulated (HFM) pulses. A review of single-pulse bounds on the variance of unbiased estimators (i.e., Cramér-Rao lower bounds) is presented to facilitate development of bounds when combining echoes from multiple pulses. The pulse characteristic time-frequency properties comprising the single-pulse bounds are employed to provide multiple-pulse bounds that are straightforward to evaluate. As might be expected, the case of coherent echoes (i.e., echoes having a common bulk phase) generally leads to a lower bound on estimation performance than when the echoes are incoherent (i.e., they have different bulk phases). A number of examples are used to demonstrate multiple-pulse estimation performance. An important theme seen throughout the examples is that diversity across multiple pulses can have an outsize effect on parameter estimation (i.e., the bound decreases by a factor greater than the number of pulses). For similar types of pulses, spectral diversity improves time-delay estimation and temporal diversity aids estimation of radial velocity. Independent of this, diversity in the time-frequency character of the pulses (e.g., combining up- and down-sweeping LFM or HFM pulses) can provide a similarly significant improvement over the performance of any of the pulses alone.

# Contents

**1 Introduction and background** **1**
1.1 Waveform choices for estimating radial velocity . . . 2
1.2 Cramér-Rao lower bounds . . . 5

**2 Single-pulse modeling of radial-velocity and time-delay estimation performance** **7**
2.1 Estimating radial velocity through Doppler . . . 7
2.2 Statistical modeling and analysis assumptions . . . 9
2.2.1 Signal and noise models . . . 9
2.2.2 Relating the SNR after coherent detection processing to terms in the sonar equation . . . 11
2.2.3 Fisher information matrix (FIM) for complex-Gaussian-distributed data . . . 12
2.3 Characteristic time-frequency parameters of frequency-modulated (FM) waveforms . 13
2.3.1 Basic waveform types (CW, LFM, & HFM) . . . 14
2.3.2 The power-law frequency-modulated (PLFM) waveform . . . 15
2.4 Single-pulse bounds for estimation of time delay (range) and Doppler scale (radial velocity) . . . 17
2.4.1 Basic sonar pulses when one parameter is known . . . 19
2.4.2 Basic sonar pulses when both radial velocity and time delay are unknown . . 21
2.4.3 Modifications for one-way and bistatic propagation . . . 24
2.4.4 Accounting for estimation of the angle of arrival . . . 25

**3 Time-delay-based multiple-pulse estimation of radial velocity** **28**
3.1 Geometric modeling for multiple pulses . . . 28
3.2 Modeling the delay measurements after matched filtering . . . 32
3.3 Least-squared-error estimators of range and radial velocity . . . 34
3.4 Performance bounds . . . 36
3.4.1 Radial-velocity estimation with a uniform pulse train . . . 37

**4 Cramér-Rao lower bounds when estimation employs multiple orthogonal pulses** **38**
4.1 Characterizing the pulses . . . 39
4.2 Bounds for coherent echoes . . . 40
4.3 Bounds for incoherent echoes . . . 41
4.4 Effect of changing the time of the reference pulse . . . 42

**5 Examples** **43**
5.1 CW comb waveform . . . 43
5.2 Sequences of identical pulses . . . 45
5.2.1 Characterizing the pulse train . . . 46
5.2.2 Coherent echoes . . . 47
5.2.3 Incoherent echoes . . . 48
5.2.4 Uniform LFM pulse trains . . . 49
5.2.5 Waveform triplets . . . 49
5.2.6 Up-sweeping FM pulses are better for predicting range . . . 50
5.2.7 Uniform PLFM pulse trains . . . 51
5.3 Reconstituting an LFM pulse . . . 54
5.3.1 Coherent echoes . . . 54

5.3.2 Incoherent echoes and the impact of spreading loss . . . . . 54
5.3.3 Time-delay-based estimation . . . . . 56
5.3.4 Characterizing the sub-pulses . . . . . 57
5.4 Pairs of up- and down-sweeping LFM pulses . . . . . 59
5.4.1 Up-down and down-up LFM waveforms . . . . . 60
5.4.2 X-LFM waveform . . . . . 61
5.5 FM-CW pulse pair . . . . . 62

**6 Summary** **64**

**References** **64**

**A FIM terms for multiple orthogonal pulses** **A1**
A.1 Coherent echoes . . . . . A2
A.2 Incoherent echoes . . . . . A4

# 1 Introduction and background

A common inferential objective in active sensing systems is estimation of the location and radial velocity of an object of interest (OOI). This is typically accomplished using time delay to obtain range, beamforming for the angle pointing to the OOI, and Doppler to estimate radial velocity. The focus of this report is on performance bounds for estimation of the OOI's time delay and radial velocity, with an emphasis on the latter when the former is unknown and when it is performed using multiple frequency-modulated pulses.

The primary bound evaluated in this report is the Cramér-Rao lower bound (CRLB) on the variance of unbiased parameter estimators [1, Sect. 6.3.3]. Uses for the CRLB and prior work related to estimation of time delay and radial velocity are described in Sect. 1.2. A review on modeling estimation performance when using a single pulse is presented in Sect. 2 for the basic sonar waveforms, which include continuous-wave (CW), linear-frequency-modulated (LFM), and hyperbolic-frequency-modulated (HFM) pulses. An introductory discussion on waveform choice when estimating radial velocity is paramount can be found in Sect. 1.1. Modifications of the analysis from the nominal two-way monostatic sensing geometry to one-way and bistatic propagation as well as accounting for simultaneous estimation of the angle of arrival are covered at the end of Sect. 2.

The single-pulse bounds for estimating time delay and radial velocity are defined in Sect. 2.4 using time-frequency characteristics extracted from the instantaneous frequency of the sensing waveform. When time delay is unknown, the CRLB on radial-velocity estimation is inversely proportional to the linear-quantity signal-to-noise power ratio (SNR), the square of the pulse duration, and the square of the center frequency for CW pulses or the square of the bandwidth for LFM pulses. This makes CW pulses a popular choice for estimating radial velocity. However, their detection performance suffers when reverberation dominates the background and the OOI has a low radial speed. In these scenarios, it is common to estimate radial velocity using time-delay measurements obtained from sequentially projected LFM or HFM pulses. This approach is reviewed and analyzed in Sect. 3, including a presentation of the geometric modeling required to estimate time delay and radial velocity from multiple pulses. The multiple-pulse performance bounds for this approach are constructed from the bounds on time-delay estimation using single pulses, the times at which the pulses are projected, and their Doppler-dependent biases in the measured time delays. Although the single-pulse bounds are inversely related to bandwidth, increasing the temporal spread over which the pulses are projected can improve estimation of radial velocity to be comparable to that achieved by CW pulses with their inverse dependence on center frequency.

When the time between pulses is large, the bulk phase[1] of an echo from the OOI is likely to change owing to variations in the sensing conditions (e.g., from platform motion or time-varying oceanographic conditions). The time-delay-based approach described in Sect. 3, which works in this scenario, can be described as incoherent processing because it does not exploit the bulk phase of each echo after matched-filtering. However, pulses that are projected near enough to each other in time and frequency are likely to have the same bulk phase in their echoes. This permits coherent processing between the echoes, which generally results in better estimation performance than incoherent processing. The CRLBs for joint estimation of time delay and radial velocity under these two conditions of coherency and incoherency between echoes from orthogonal pulses are presented

[1]The bulk phase of an echo represents the effect of propagation through the underwater acoustical channel and reflection off the OOI. For example, reflection off the surface imparts a sign inversion, which is a 180° phase shift. Total internal reflection from the bottom [1, Sect. 3.2.7.5] changes the phase in a manner dependent on the properties of the water column, bottom, and the angle of incidence.

in Sect. 4 using the characteristic time-frequency parameters and projection times of each pulse, with derivation relegated to the appendix. The goal of multiple-pulse radial-velocity estimation is often to shift the performance of broadband waveforms from being dominated (inversely) by bandwidth to being driven by center frequency, as is the case for CW pulses. The CRLBs for coherent echoes are seen to achieve this goal when they satisfy certain diversity conditions, whereas incoherent echoes maintain the bandwidth dependence and therefore rely on temporal spread to achieve high-quality estimates of radial velocity.

The bounds on performance for estimating radial velocity and/or time delay from coherent and incoherent echoes are evaluated for a number of examples in Sect. 5. These include comb waveforms (Sect. 5.1), sequences of identical pulses (Sect. 5.2), reconstitution of an existing LFM pulse (Sect. 5.3), combinations of up- and down-sweeping LFM pulses (Sect. 5.4), and FM-CW pulse pairs (Sect. 5.5). These examples illustrate the bandwidth or center-frequency dependence described above and elucidate how diversity in the projection times of the pulses or their time-frequency coupling can improve estimation performance.

Although there is novel material in this report, there is a significant amount of background on estimating time delay and radial velocity in active sensing systems. This is presented to allow the report to be reasonably self-contained, with the goal of providing enough details for the reader to apply the material to their own pulse or pulse combinations. The majority of results found in the journal articles cited in Sect. 1.2 are dense enough with mathematical derivations to inhibit their use by those primarily interested in the design or analysis of sensing systems employing multiple pulses for estimating time delay and radial velocity. In contrast, the performance bounds described in Sect. 4 for multiple coherent or incoherent echoes are straightforward enough to evaluate from the individual-pulse characteristic time-frequency parameters presented in Sect. 2.3 that they can be applied directly to the development and analysis of combinations of the standard sonar pulses for the purpose of estimating time delay and radial velocity.

## 1.1 Waveform choices for estimating radial velocity

Choosing active sensing waveforms is an important part of the sonar design process. Only a brief summary of some of the more common options is presented here; other resources include [2–4]. The sensing objectives of detecting an OOI and estimating its range and radial velocity robustly across diverse environmental conditions usually results in no single waveform being universally applicable. As seen below, this generally leads to projecting multiple similar or dissimilar waveforms in each "ping" (i.e., one cycle of projecting one or more pulses followed by a measurement period) or delaying radial-velocity estimation until echoes from multiple pings have been detected. In addition to choosing the sensing waveform(s), the associated detection processing (including normalization) and radial-velocity estimator need to be defined. For Doppler-sensitive waveforms or multiple-pulse combinations that are processed coherently, this generally involves implementation of a Doppler filter bank [1, Sect. 8.7.1] with the Doppler channel in which the peak occurs providing a coarse estimate of radial velocity. Although the Doppler filter bank is often adequate for detection, a refined estimation of time delay and Doppler is generally necessary to achieve the full potential in estimation performance, especially at high SNR where the accuracy can be significantly better than the size of a sonar resolution cell [1, Sect. 8.5.1.2].

The most popular waveform choice for estimating radial velocity is the CW pulse, owing to its simple projection and processing and the aforementioned inverse dependence on center frequency in

the CRLB. However, CW pulses have poor temporal resolution, which means their detection performance suffers when the background is dominated by reverberation. Because underwater acoustic reverberation arises from reflections off boundaries (which are stationary or slowly undulating) or slowly moving objects (e.g., bubbles or fish) it primarily impacts OOIs with a low radial speed (i.e., "low Doppler" echoes). When an OOI has a large enough radial speed (i.e., "high Doppler"), its echo is shifted spectrally away from the reverberation. This allows operation in a noise-limited regime where detection performance improves with the energy in the projected pulse.

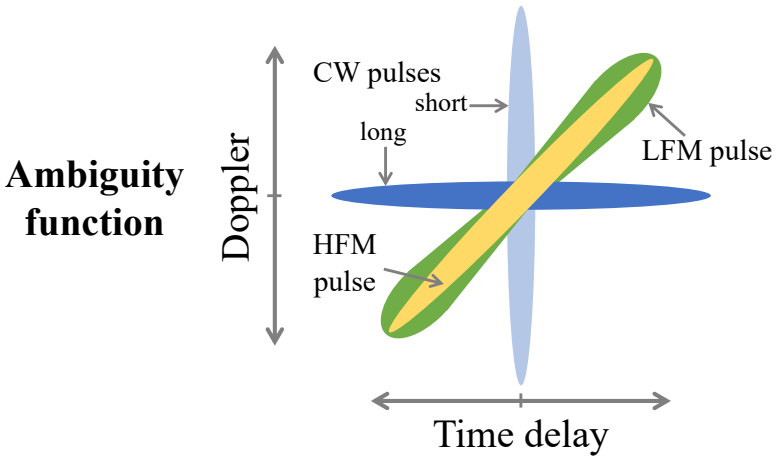


Figure 1: Depiction of the ambiguity function for the basic sonar pulse types.

The ambiguity function of a waveform [1, Sect. 8.3] is useful in interpreting its performance with respect to estimation of time delay and radial velocity. For example, the depictions in Fig. 1 illustrate how a long CW pulse is narrow in the Doppler dimension but broad in time. While shortening the CW pulse reduces its susceptibility to reverberation (by allowing fewer scattering points in its sonar resolution cell), it degrades estimation of radial velocity and potentially diminishes detection performance in ambient noise if there is a corresponding reduction in the projected energy.

When low-Doppler OOIs are a priority, broadband waveforms can improve detection in reverberation (again, by reducing the temporal extent of the sonar resolution cell, which is inversely proportional to bandwidth) and reduce the variance of the range estimate without affecting the projected energy. However, this comes at the expense of a more complicated estimation of radial velocity. For example, use of LFM or HFM pulses leads to a coupling between delay and Doppler, which is exhibited by the angled ridges in Fig. 1. This coupling makes it difficult to simultaneously obtain accurate estimates of time delay and radial velocity from a single LFM or HFM pulse. It has also earned the pulses a reputation for being insensitive to Doppler (e.g., see [5,6] or [1, Sect. 2.2.6]). The advantage of this Doppler tolerance comes from needing only a single matched filter to detect echoes having a wide span of radial velocities. The slow decay along the ridge of the ambiguity function implies there is only a small loss in SNR when there is mismatch in Doppler between the echo and the matched-filter replica. In applications where one parameter is known (e.g., the radial velocity), however, the narrowness of the ambiguity-function ridge in either dimension individually implies these waveforms will provide a high quality estimate of the unknown parameter.

When delay and Doppler are both unknown, the ambiguity function of an ideal waveform would be concentrated at the origin in both dimensions. Such ambiguity functions are usually referred

to as having a "thumbtack" shape, with a narrow main lobe at the origin above a broad plateau extending in both dimensions. Although there are a number of broadband Doppler-sensitive waveforms with thumbtack-like ambiguity functions that permit simultaneous high-quality estimation of both parameters, they often have detrimental effects that limit their applicability. As noted in [7], their implementation is hindered by the narrowness of the ambiguity function in the Doppler dimension, which requires many filter channels (and cannot exploit the fast Fourier transform as is done for CW-pulse Doppler filter banks [1, Sect. 8.7.1.4]). A compromise might be found in the multitone sinusoidal FM waveform designs found in [8], which provide control over the size of the main lobe in the thumbtack-like ambiguity function. The wide plateau of these ambiguity functions, however, causes such waveforms to be reverberation-limited for a much wider span of radial velocities than CW pulses. Although this is similar to LFM and HFM waveforms, it implies false alarms from clutter affect a larger number of Doppler channels than for CW pulses. Broadband Doppler sensitive waveforms with thumbtack-like ambiguity functions are not a focus of this report; however, the results can be applied to those formed by frequency modulation.

In some applications, radial velocity is estimated after projecting a sequence of identical LFM or HFM pulses. When these are spaced closely in time, they can be processed coherently using a Doppler filter bank constructed from replicas consisting of the full Doppler-scaled sequence of pulses. This produces a broadband Doppler-sensitive waveform with the desired inverse dependence on center frequency in the radial-velocity CRLB and a narrow main lobe in the ambiguity function. In contrast to the pedestal in thumbtack-like ambiguity functions, however, the FM-pulse-train ambiguity function exhibits very high sidelobes occurring at regular intervals. An alternative approach is to combine the echoes from the pulses incoherently, as would be required when the inter-pulse delay times are large (e.g., across multiple pings). In this approach, which is covered in detail in Sect. 3, a single matched filter provides time-delay estimates from the sequence of echoes. Mismatch in Doppler between the echoes and the matched-filter replica incurs a small loss in SNR, as was mentioned above, and a bias in the time-delay estimates that is unknown because it depends on the Doppler mismatch. Combining the biased time-delay estimates over multiple pulses, however, provides an unbiased estimate of the time delay (and therefore an unbiased estimate of the OOI range) and a potentially high-quality estimate of the radial velocity. However, only the echoes that are detected and associated with the OOI can be exploited and the association process is prone to errors in high-clutter environments. Nevertheless, this is a popular approach to handling low-Doppler echoes.

A generalization of the basic sonar pulses (CW, LFM, and HFM) can be found in the power-law-frequency-modulation (PLFM) waveform presented in [7]. The PLFM allows some adjustment of the Doppler sensitivity, at the expense of slightly poorer performance in reverberation and potentially requiring more than one matched filter (e.g., a small Doppler filter bank). In addition to providing an overarching framework to describe the basic sonar pulses, the PLFM waveforms have the potential to provide a computationally lighter detector structure than many broadband Doppler-sensitive waveforms (i.e., fewer Doppler channels) and competitive multiple-pulse radial-velocity estimation.

It is quite common to use more than one type of pulse in an active sensing system. The most common example [9, 10] is the combination of a CW pulse for estimating radial velocity and an FM pulse for accurate range estimation and protection against reverberation. Although the waveforms are processed separately in most applications, they can be combined coherently to some advantage (Sect. 5.5). Simultaneous projection of multiple CW pulses in a "comb" waveform can provide

improved time-delay estimation (Sect. 5.1). Finally, an example of a broadband pulse pair that achieves the desired center-frequency dependence of the radial-velocity CRLB can be found when combining up- and down-sweeping LFM or HFM pulses (Sect. 5.4).

The tools presented in this report allow evaluation of the potential that different multiple-pulse combinations might have in estimating time delay and radial velocity. However, it is important to consider all aspects of the sensing problem, which starts with detection processing (e.g., banks of matched filters and normalization) and includes post-detection information processing such as tracking and classification. The impact of waveform properties on tracking performance illustrated in [11] and the frequent use of motion to classify OOIs through moving target indicators [12, Sect. 1.7.2] demonstrate how important it is to the overall system design.

## 1.2 Cramér-Rao lower bounds

When designing an active sonar system to meet a specification, the first priority in choosing sensing waveforms is detection performance, which is controlled by the projected energy in noise-limited environments and by bandwidth when reverberation dominates. Owing to the inherent difficulty in predicting the performance of tracking and classification algorithms, the most important consideration after detection is typically how well range (via time delay) and radial velocity are estimated. The Cramér-Rao lower bound (CRLB) provides a metric for estimation performance that is straightforward to evaluate, even when the design exploits multiple pulses either coherently or incoherently (Sect. 4).

The CRLB describes the minimum variance attainable by any unbiased estimator of a parameter. The reader is referred to [13, Ch. 3] for a thorough description of the CRLB or [1, Sect. 6.3.3] for a brief introduction. An unbiased estimator is one whose average error is zero. An example of a biased estimator is when there is Doppler mismatch between an LFM or HFM echo and the replica used in the matched filter. The peak response of the matched filter will on average occur at a time offset from the true delay, so the time-delay estimate is biased. In Fig. 1, the matched filter response under mismatch is (essentially[2]) represented by a horizontal slice above or below the origin, where the peak response does not occur at the correct delay.

When the variance of an estimator achieves the CRLB, it is called an "efficient" estimator. Unfortunately, the theory surrounding the CRLB does not dictate which estimator might be efficient, except for maximum likelihood estimators (MLEs) when taken asymptotically as the number of measurements grows infinite. Estimators using a finite number of measurements need to be assessed individually to determine if they are efficient or not. However, the asymptotic result is useful in the present application at high SNR because estimates of time delay and radial velocity formed by maximizing the matched-filter response can be treated as an MLE employing a large number of weaker measurements, so it is therefore approximately efficient. Under the assumption that a parameter estimator is efficient or nearly so, the CRLB can be used to approximate its variance. Coupling this with an assumption of Gaussian-distributed errors (which also arise asymptotically for MLEs) allows formation of confidence intervals for parameter estimates [1, Sect. 6.3.8]. Confidence intervals or the CRLB itself can also be useful when designing waveforms or pulse trains to achieve a desired level of estimation performance.

[2] As described in [1, Sect. 8.3.1.3], the response of a single filter to an echo with a given Doppler is represented by a time-reversed ambiguity function evaluated at the relative Doppler of the echo; see [1, eq. 8.137].

It is important to note that CRLBs represent the variance of what are termed "small" errors, which arise when the estimate is within half the Rayleigh resolution [1, Sect. 8.5.1] of the true value of the parameter. This inherently takes some minimum amount of SNR to occur reliably. As SNR decreases, the probability of a "large" error increases and the variance in any practical estimator tends to exhibit a sharp rise above the CRLB at some "threshold" SNR. One approach for representing the large errors can be found in [14] where the estimator is modeled as having a mixture of small and large errors, with the latter depending on the extent of a pre-defined search region. Only the CRLB and its small-error interpretation are considered in this report.

An advantage of CRLBs is that they are often easier to evaluate than a theoretical analysis of the bias and variance of a parameter estimator. The process starts with a statistical model for the measurements that depends on the parameters of interest and any other unknown parameters required to describe the signal and noise. When there are multiple parameters, their CRLBs are obtained from the diagonal elements of the inverse of the Fisher information matrix (FIM). The FIM characterizes how the information in the measurement applies to each unknown parameter individually and how it is coupled across each pair of parameters. More information on an individual parameter (i.e., a higher-valued diagonal element in the FIM) implies a higher quality parameter estimate when all other parameters are known. By employing the inverse FIM, the CRLB captures the coupling (identified by non-zero cross terms in the FIM) across all of the unknown parameters. When two unknown parameters are coupled, lack of knowledge about one degrades estimation of the other. For example, the CRLB for estimating radial velocity when using an LFM pulse is inversely proportional to the square of the center frequency when time delay is known. However, when time delay is unknown, the coupling changes the inverse dependence to be on the squared bandwidth, which is usually significantly smaller than the center frequency. The lack of knowledge about time delay adversely affects estimation of the radial velocity and vice versa. When evaluating the CRLB for a parameter, only unknown and coupled parameters need to be included.

In many systems, the angle of arrival of the echo is also unknown and must be estimated using an array of sensors. CRLBs for the joint estimation of the delay, Doppler, and arrival-angle parameters can be found in [15]. A classic analysis of angle estimation using a line array can be found in [16], as well as in [14] for the closely related problem of estimating the frequency of a sinusoid. When the OOI is in the far-field of the array and the signal is considered narrowband with respect to the array processing, it is shown in Sect. 2.4.4 that an appropriate choice of the origin of the sensor array decouples arrival angle from both time delay and Doppler. This permits the omission of arrival angle among the unknown and coupled parameters in the analysis.

In active sensing, the FIM and CRLBs for estimating delay and a Doppler parameter depend on temporal and spectral characteristics of the projected pulse that can be crafted in terms of derivatives of the waveform ambiguity function [17, Ch. 5], [18, Sect. 10.2.1], [3, pg. 180] or the instantaneous frequency of constant-envelope frequency-modulated pulses [1, Sect. 8.5]. Waveforms with amplitude shading are only marginally more difficult to evaluate [3, pg. 188]. These terms essentially capture the width of the ambiguity function in the Doppler and time-delay dimensions and any coupling between the parameters. Prior to the now common CRLB analysis, earlier approaches (e.g., [19] as summarized in [20]), approximated the variances of joint delay and Doppler estimators formed using matched filters. Although both of these approaches handle the problem of simultaneous estimation of time delay and Doppler, they are commonly restricted to narrowband waveforms, for which the Doppler parameter is a frequency shift. CRLB formulations accounting for the Doppler scale required for broadband waveforms are relatively rare (e.g., [7, 21, 22], [3, Ch.

4] or [1, Sect. 8.5]). This report presents the broadband formulations.

The CRLB for $M$ multiple independent and identically distributed measurements is simply that for one measurement divided by $M$. When an active sensing system projects multiple pulses, however, the echoes from the different pulses are not necessarily identical. In particular, the time delay between the echoes of pulses projected at different times is altered by the time-compression or dilation for OOIs having non-zero radial velocity. This implies that the radial velocity of the OOI is encoded in both the Doppler scale and the time delays between echoes. Although the frequency-domain representation of a Doppler shift in the narrowband approximation can obscure this, it is overt in the Doppler scale formulation and must be accounted for in the analysis. A number of CRLB analyses exist for multiple pulses (e.g., [15, 22, 23]). However, they are usually restricted to the narrowband case and often consider specific waveforms with no coupling between delay and Doppler. The multiple-pulse CRLBs derived in this report account for the effect of Doppler on the delays between echoes within the context of a broadband analysis that permits delay-Doppler coupling. They are also formulated using the characteristic time-frequency parameters of the individual pulses, which enables a straightforward analysis of arbitrary combinations of the basic sonar pulses.

# 2 Single-pulse modeling of radial-velocity and time-delay estimation performance

A review of performance bounds for estimating radial velocity and time delay from a single pulse observed in a monostatic active sonar system is presented in this section. The mathematical model of the echo and its relationship to Doppler scale are presented in Sect. 2.1. Statistical models for the signal and noise are described in Sect. 2.2, along with the corresponding Fisher information matrix (FIM), from which Cramér-Rao lower bounds can be constructed. The elements of the FIM depend on a suite of parameters describing the time-frequency characteristics of the sonar pulse. The definitions of these parameters for frequency-modulated pulses, including specific results for the basic sonar pulses (CW, LFM, & HFM) and the more general power-law FM (PLFM) pulse, are found in Sect. 2.3. Bounds on the variance of unbiased estimators of the parameters are then presented in Sect. 2.4 and discussed for the basic sonar pulses when one parameter is known (Sect. 2.4.1) and when both are unknown (Sect. 2.4.2). An adaptation of the results to account for one-way or bistatic propagation is presented in Sect. 2.4.3 and the impact of estimating angle of arrival is assessed in Sect. 2.4.4.

## 2.1 Estimating radial velocity through Doppler

In active sensing systems, the relative radial velocity between a sonar platform and an OOI is straightforward to estimate from a single echo by exploiting the Doppler effect or through the arrival times of multiple echoes when at least two pulses are projected at different times. In this section, the focus is on exploiting the Doppler effect using a single pulse in a mono-static sonar system. In a basic ocean model,[3] the analytic form[4] of the measured data can be represented by

$$\mathring{x}(t) = Ae^{j\psi}\mathring{s}(\eta[t-\tau]) + \mathring{v}(t) \quad \text{[units: } \mu\text{Pa]}, \tag{1}$$

[3]The basic ocean model assumes the propagation environment is boundaryless, homogeneous, lossless, and dispersionless [1, pg. 96].

[4]The analytic form of a signal [1, Sect. 7.3.1] strips away the negative-frequency spectral components to produce a complex-valued representation that is often easier to use in mathematical analysis.

where $\mathring{s}(t)$ and $\mathring{v}(t)$ are, respectively, the analytic forms of the projected pulse and the measured background noise, $\tau$ [units: s] is the two-way propagation delay, $\eta$ [unitless] is the Doppler scale, $A$ is the amplitude of the echo in field-quantity units (e.g., pressure or a quantity proportional to pressure), and $\psi$ [units: rad] is the bulk phase. Estimates of the primary two unknown parameters ($\tau$ and $\eta$) are obtained by maximizing the squared modulus of a matched filter [1, Sect. 8.2.8.2]. The estimators are typically implemented in concert with a detector in a Doppler filter bank [1, Sect. 8.7.1], which consists of a suite of matched filters running in parallel with replicas tuned to span the Doppler scales expected to be observed. The Doppler channel in which the maximum response occurs and its time provide coarse estimates of $\eta$ and $\tau$ that can be refined either with a local search or from a parametric fitting to a function approximating the ambiguity function near its peak.

The Doppler scale [1, Sect. 2.2.5] arises from an assumption of constant relative radial velocity in the active-sonar sensing problem (e.g., see [24, Sect. 11.2] or [1, Sect. 3.2.3.3] for its derivation by solving the inhomogenous wave equation for a moving source). For narrowband waveforms in a two-way monostatic geometry, the Doppler scale simplifies to a Doppler shift of $\delta_f \approx (\eta-1)f_c \approx 2vf_c/c_w$ [units: Hz] where $f_c$ [units: Hz] is the center frequency, $c_w$ [units: m/s] is the speed of sound in water, and $v$ [units: m/s] is the relative radial velocity.

Although the echo is characterized in terms of its time delay and Doppler, they are often converted to, respectively, range and relative radial velocity,

$$r = \frac{c_w\tau}{2} \quad \text{[units: m] and } v = \frac{c_w(\eta-1)}{2} \quad \text{[units: m/s].} \tag{2}$$

The equation for radial velocity is obtained from an approximation to the monostatic Doppler scale found in [1, pg. 53, eq. 2.31],

$$\eta = \frac{(c_w - v_o)(c_w + v_a)}{(c_w + v_o)(c_w - v_a)} \approx 1 + \frac{2v}{c_w}, \tag{3}$$

where $v = v_a - v_o$ with $v_o$ the radial velocity of the OOI and $v_a$ the radial velocity of the active sonar platform. The relative radial velocity is assumed to be constant (i.e., there is no acceleration component). The approximation in (3) is accurate when the speeds of the sonar platform and OOI are much less than the speed of sound, which is generally the case in underwater acoustical sensing. With the sonar platform at the origin and the OOI at a range $r$ in the positive direction of the radial axis, $v > 0\,\text{m/s}$ implies the range between the two objects is decreasing (i.e., they are "closing"). Similarly, they are "opening" when $v < 0\,\text{m/s}$. Although the opposite definition is also common, it requires a change to (3) because the time scale $\eta > 1$ for closing objects and $\eta < 1$ for opening ones. In this report, the relative radial velocity ($v$) will generally be referred to as a radial velocity, assuming the sonar platform is stationary.

The approach taken in this report to assess estimation performance is to obtain bounds on the variance of estimators for time delay and Doppler scale. The results presented here follow those found in [1, Sect. 8.5]. Owing to the linear relationships seen in (2), the variances (or bounds) of range and radial-velocity estimators can be obtained by multiplying those for time delay and Doppler scale by $(c_w/2)^2$ (e.g., $\text{Var}\{\hat{v}\} = \text{Var}\{\hat{\eta}\}\,(c_w/2)^2$, where the notation $\hat{v}$ represents an estimate of $v$, unless noted otherwise). The results presented for specific examples will generally be for time delay ($\tau$) and radial velocity ($v$) owing to their ubiquitousness in the field.

## 2.2 Statistical modeling and analysis assumptions

In a sonar system, the estimation of radial velocity from a single sonar pulse is typically done after an echo is detected by identifying the value of $v$ (or $\eta$) for which the matched-filter intensity is maximized. When time-delay is unknown, the maximization occurs in both $\tau$ and $v$. These estimators can be derived through the maximum likelihood approach under certain statistical models for the signal and noise. Analysis of the estimation performance similarly requires assumptions for the statistical models of the signal and noise. The Gaussian-based models typically used to evaluate estimation performance are described in Sect. 2.2.1.

In this report, estimation performance is quantified through the Cramér-Rao lower bound (CRLB), which describes the minimum variance attainable by an unbiased estimator. Although the CRLB does not indicate what estimator might achieve its limit on performance, maximum-likelihood estimators are known to achieve the bound asymptotically as the number of observations increases to infinity [13, Sect. 7.5]. As is the case in many applications, the asymptotic result requiring a large number of observations also applies here to single observations with an asymptotically large SNR (i.e., a single high-SNR observation can be described as a large number of observations with lower SNRs). The point at which the CRLB-based analysis fails is when too many "large errors" occur. A large error occurs when the magnitude of the estimation error is (approximately) more than half the Rayleigh resolution, which puts it out of the main-lobe of the ambiguity function. Although these can be accounted for in the analysis (e.g., see [14]), the focus here is strictly on the CRLB.

The CRLB is formed from the Fisher information matrix (FIM), which represents how much knowledge about each of the unknown parameters is contained in the measurements and reveals the connections between parameters. The FIM is a square matrix whose size is equal to the number of unknown parameters. However, ancillary parameters that are uncoupled from the others can be ignored because they do not impact estimation of the parameters of interest. The general form of an FIM entry for complex-Gaussian-distributed data is presented in Sect. 2.2.3 along with its simplification for estimating parameters in a deterministic-signal model subject to additive Gaussian noise. The application to estimating time delay and Doppler scale is then presented in Sect. 2.4.

### 2.2.1 Signal and noise models

When the performance of a parameter estimator is analyzed, it is important to account for all parts of the estimation process. With the present focus on radial velocity, this implies accounting for estimation of time delay, which is usually also unknown. For some waveforms (e.g., linear- and hyperbolic-frequency-modulated ones), errors in time-delay estimation can adversely impact estimation of Doppler scale. For these waveforms, the two parameters are coupled, which also impacts how the performance bounds are evaluated. In addition to the time delay, the amplitude and bulk phase of the echo and any parameters defining the noise are also generally unknown. In systems employing a sensor array, the angle of arrival of the echo must also be estimated. As seen in Sect. 2.4.4, the angle of arrival can be completely decoupled from the other parameters when the OOI is in the far-field of the sensor array by defining the array origin as its geometric center. However, any parameters that are unknown and coupled with time delay or Doppler scale must be accounted for in the analysis. This process starts by defining statistical models for the signal and noise.

The noise is typically assumed to be a bandpass Gaussian random process with a constant

power spectral density within the frequency band of the projected pulse. The statistical model of the signal depends on the assumptions made for the amplitude ($A$) and bulk phase ($\psi$) of the echo. As described in [1, Sect. 7.5], propagation conditions play an important role in this choice. For example, extensive unresolved multipath can lead to a Gaussian-fluctuating signal where $A$ follows a Rayleigh distribution and $\psi$ is uniformly random on $[0, 2\pi)$. More benign propagation allows the amplitude to be considered deterministic, where repeated observations produce the same result. The bulk phase of the signal in these situations might be taken as deterministic or uniformly random. Spanning these two extremes is the Rician signal, which has deterministic and Gaussian-random components. In the application considered here, where echoes from multiple pulses are combined to estimate radial velocity, it is appropriate for the echo to be deterministic with unknown, non-random amplitude and phase. Performance bounds for the scenarios of constant and varying bulk phase across multiple echoes are presented in, respectively, Sects. 4.2 and 4.3.

In order to derive performance bounds, statistical models of the signal and noise need to be defined explicitly for the measured data. This is most easily done by demodulating the analytic form of the measurement in (1) to form the complex-envelope,

$$\tilde{x}(t) = e^{-j2\pi f_c t}\mathring{x}(t) = \tilde{u}(t) + \tilde{v}(t), \tag{4}$$

where $\tilde{u}(t)$ and $\tilde{v}(t)$ represent the signal and noise components, respectively, and $f_c$ [units: Hz] is the center frequency of the signal. This process converts bandpass Gaussian noise to be low-pass, complex, zero-mean Gaussian noise. The signal component is obtained by demodulating the Doppler-scaled and time-delayed analytic signal (i.e., $\mathring{s}(\eta[t-\tau])$) from the center frequency of the original pulse to yield the complex envelope

$$\tilde{u}(t) = Ae^{j\psi}\mathring{s}(\eta[t-\tau])\, e^{-j2\pi f_c t}. \tag{5}$$

Note that this differs from the derivation in [1, Sect. 8.5] in that it does not include the delay in the demodulation.[5] The next step is to sample the complex envelope $\tilde{x}(t)$ to form a vector $\mathbf{x}$ spanning the time over which the echo is observed, which generally has an extent equal to the pulse duration, $T_p$ [units: s]. If the signal bandwidth is $W$ [units: Hz], sampling every $1/W$ [units: s] produces noise samples that are uncorrelated,[6] which simplifies evaluation of the Fisher information matrix.

A key parameter in modeling estimation performance is the signal-to-noise power ratio (SNR). Following the modeling approach found in [1, Sect. 8.2], the sampled analytic-signal (i.e., just the samples of $\mathring{s}(t)$) is assumed to be scaled to have unit energy; that is, the vector comprising the samples has unit length.[7] The SNR after coherent detection processing is then $S^{\mathrm{d}} = A^2/\lambda$ [unitless], where $\lambda$ [units: $\mu\mathrm{Pa}^2$] is the variance of $\tilde{v}(t)$. It is possible to relate $A^2$ and $\lambda$ to parameters such as the energy of the measured signal and the noise power spectral density (e.g., see [1, Sects. 8.2 &

[5] The effect of this is that the frequency averages used in the Fisher information matrix come from the analytic signal rather than the complex envelope. It does not alter the single-pulse bounds; however, it simplifies the analysis presented in Sect. 4 for multiple pulses that might have different center frequencies.

[6] After limiting the spectrally flat noise to the frequency band of the signal, the autocorrelation function of its complex envelope is proportional to $\mathrm{sinc}(\tau W)$, which is zero when $\tau$ is a non-zero-integer multiple of $1/W$.

[7] Specifically, if the signal is defined to exist over the interval $t \in [-T_p/2, T_p/2]$, this implies

$$\sum_{n=1}^{T_p W} \left|\mathring{s}\left(\frac{-T_p}{2} + \frac{n-1}{W}\right)\right|^2 = 1 \approx W \int_{-T_p/2}^{T_p/2} |\mathring{s}(t)|^2 \, \mathrm{d}t, \tag{6}$$

where the approximation comes from the Riemann-sum definition of an integral and $\mathrm{d}t \approx 1/W$.

8.2.1]). However, this is often complicated by scale choices in the signal processing that affect the absolute levels of the signal and noise, but not their power-quantity ratio (i.e., $S^{\mathrm{d}}$). The relationship between $S^{\mathrm{d}}$ and the terms of the sonar equation found in Sect. 2.2.2 is therefore more relevant in the broader context of waveform design in the presence of ambient noise and reverberation.

The choice of a deterministic-signal model allows analysis of the multiple-pulse case with explicit control over the bulk-phase in the echo from each pulse. However, it requires including the bulk phase as an unknown parameter, which follows the analysis presented in [17, Ch. 5] for narrowband waveforms or [1, Sect. 8.5] for broadband ones. This differs from the CRLB derivations found in [18, Sect. 10.2.1], which are based on the Gaussian-fluctuating signal. The Gaussian-fluctuating signal model does not require including the bulk phase of the signal as a parameter because it is treated as uniformly random. However, the derivation of its FIM is more complicated because the signal enters through the covariance matrix of $\mathbf{x}$ rather than its mean. The Gaussian-fluctuating signal also presents difficulties in multiple-pulse scenarios when the complex amplitude is expected to be the same for each, but still random (e.g., see [25]). For single-pulse analysis, however, the two signal models tend to the same result as SNR increases: the CRLB for a Gaussian-fluctuating signal is proportional to $(1+S^{\mathrm{d}})/[S^{\mathrm{d}}]^2$, whereas it is proportional to $1/S^{\mathrm{d}}$ for a deterministic signal.

### 2.2.2 Relating the SNR after coherent detection processing to terms in the sonar equation

The signal-to-noise power ratio (SNR) can be determined at different points in the signal processing chain and using different definitions [1, Sect. 2.3], so it is important to define it explicitly. In this report, the SNR used in evaluating estimation performance is defined as the unitless ratio ($S^{\mathrm{d}}$) of the signal power to the noise power after coherent detection processing, which here entails matched filtering. Using a basic active-sonar equation, it can be defined as

$$S^{\mathrm{d}} = \frac{U_o G_{\mathrm{t}} G^{\mathrm{a}} T_p W}{L_{p,a} L_{p,b} (N_0 W + R_0 T_p)}, \quad \text{[unitless]} \tag{7}$$

where the linear-quantity terms from the sonar equation include the

- source factor, $U_o$ [units: $\mu\mathrm{Pa}^2\mathrm{m}^2$],
- propagation loss factor from the sonar projector to the OOI, $L_{p,a}$ [units: $\mathrm{m}^2$],
- target gain, $G_{\mathrm{t}}$ [units: $\mathrm{m}^2$],
- propagation loss factor from the OOI to the sonar sensor array, $L_{p,b}$ [units: $\mathrm{m}^2$],
- (one-sided) noise power spectral density, $N_0$ [units: $\mu\mathrm{Pa}^2/\mathrm{Hz}$],
- pulse bandwidth, $W$ [units: Hz],
- reverberation pulsing rate, $R_0$ [units: $\mu\mathrm{Pa}^2/\mathrm{s}$],
- pulse duration, $T_p$ [units: s], and
- array gain, $G^{\mathrm{a}}$ [unitless].

It is clear from the units that this form of the sonar equation is based on mean square pressure (MSP) rather than energy. The typical restrictions to the coherent processing band and assumptions of constant spectral densities apply. The relationships to the more familiar logarithmic-quantity terms are straightforward for the

- source level, $\mathsf{SL} = 10\log_{10} U_o$ [units: dB re $\mu\mathrm{Pa}^2\mathrm{m}^2$],
- propagation loss, $\mathsf{PL}_a = 10\log_{10} L_{p,a}$ [units: dB re $\mathrm{m}^2$],

- target strength, $\mathsf{TS} = 10\log_{10} G_{\mathrm{t}}$ [units: dB re $\mathrm{m}^2$], and
- array gain, $\mathsf{AG} = 10\log_{10} G^{\mathrm{a}}$ [units: dB].

When noise and reverberation level are defined as their total MSP in the coherent processing band at a hydrophone, as is done in [1, Sect. 2.3], then the

- noise level is $\mathsf{NL} = 10\log_{10}(N_0 W)$ [units: dB re $\mu\mathrm{Pa}^2$] and the
- reverberation level is $\mathsf{RL} = 10\log_{10}(R_0 T_p)$ [units: dB re $\mu\mathrm{Pa}^2$].

The form of (7) clearly illustrates that in noise-limited scenarios SNR increases in proportion to $U_o$ and $T_p$ and that it is precisely $\mathcal{E}/N_0$ where $\mathcal{E}$ [units: $\mu\mathrm{Pa}^2\mathrm{s}$] is the energy in the echo. In reverberation-limited conditions $S^{\mathrm{d}}$ is proportional to bandwidth, as expected, and not dependent on $U_o$ (for simple models in which $U_o/R_0$ is approximately constant).

### 2.2.3 Fisher information matrix (FIM) for complex-Gaussian-distributed data

The most common approach for assessing the performance potential in an estimation problem is to evaluate the Cramér-Rao lower bound (CRLB), which defines the minimum variance attainable by an unbiased estimator. More details on the CRLB can be found in [13, Ch. 3] & [1, Sect. 6.3.3]. The first step in obtaining the CRLB for a parameter is to evaluate the Fisher information matrix (FIM) for all unknown parameters in the estimation problem. The CRLB for a single parameter is then the corresponding diagonal element of the inverse of the FIM.

Suppose the unknown parameters are placed in the vector $\boldsymbol{\theta}$ and let the measured data ($\mathbf{x}$) be complex-Gaussian distributed with mean $\boldsymbol{\mu}(\boldsymbol{\theta})$ and covariance matrix $\boldsymbol{\Sigma}(\boldsymbol{\theta})$. This allows the parameters to enter either the mean or covariance matrix of the measured data. From [1, eq. 6.75] or [13, App. 15C], the $(i,j)$ element of the Fisher information matrix is then

$$\mathrm{FIM}_{\theta_i,\theta_j} = 2\,\mathrm{Real}\left\{\frac{\partial \boldsymbol{\mu}^H(\boldsymbol{\theta})}{\partial\theta_i}\boldsymbol{\Sigma}^{-1}(\boldsymbol{\theta})\frac{\partial \boldsymbol{\mu}(\boldsymbol{\theta})}{\partial\theta_j}\right\} + \mathrm{trace}\left\{\boldsymbol{\Sigma}^{-1}(\boldsymbol{\theta})\frac{\partial \boldsymbol{\Sigma}(\boldsymbol{\theta})}{\partial\theta_i}\boldsymbol{\Sigma}^{-1}(\boldsymbol{\theta})\frac{\partial \boldsymbol{\Sigma}(\boldsymbol{\theta})}{\partial\theta_j}\right\}. \tag{8}$$

The deterministic-signal model described in Sect. 2.2.1 implies the parameters only enter the distribution of the data through the mean, where the elements of $\boldsymbol{\mu}(\boldsymbol{\theta})$ are samples of $\tilde{u}(t)$ from (5). Because the covariance matrix $\boldsymbol{\Sigma}$ does not depend on $\boldsymbol{\theta}$, the latter term in (8) is zero. Sampling the complex envelope data at the signal bandwidth implies the covariance matrix is proportional to an identity matrix, $\boldsymbol{\Sigma}(\boldsymbol{\theta}) = \lambda\mathbf{I}$, where $\lambda$ is the noise power. As seen in [1, eq. 8.256], the $(i,j)$ element of the Fisher information matrix for this scenario can then be approximated by the integral

$$\mathrm{FIM}_{\theta_i,\theta_j} \approx \frac{2W}{\lambda}\mathrm{Real}\left\{\int_{-\infty}^{\infty}\frac{\partial\tilde{u}^*(t)}{\partial\theta_i}\frac{\partial\tilde{u}(t)}{\partial\theta_j}\,\mathrm{d}t\right\}. \tag{9}$$

This result is straightforward to obtain by noting that $\mathrm{d}t \approx 1/W$ and using the Riemann-sum approximation to an integral. Although the technique used to obtain the result in (9) entailed sampling of the data in such a way as to simplify the statistical analysis (in particular keeping the noise uncorrelated), oversampling the data does not change the result if the noise continues to have a flat spectral density outside of the signal band. This suggests the integral approximation may be less accurate for low time-bandwidth-product waveforms in a reverberation-limited background.

### 2.3 Characteristic time-frequency parameters of frequency-modulated (FM) waveforms

For frequency-modulated waveforms, the FIM entries formed using (9) are conveniently described using a set of parameters distilling the time-frequency characteristics of the projected pulse. These simple characterizations are also exploited in Sect. 4 to describe the results when using multiple pulses to estimate radial velocity or time delay. The terms that follow, which were based on the broadband analysis in [21], can be found in various subsections of [1, Sect. 8.5]; they are collated here for convenience. Although the frequency characteristics ($\bar{f}$ and $\sigma_f^2$) are the same as those found in [17, Ch. 5] or [18, Sect. 10.2.1], the broadband derivation requires defining time in units of periods (i.e., $tf(t)$) rather than seconds, which affects the definitions for $\rho$, $\bar{c}$, and $\sigma_c^2$ (the latter two replace $\bar{t}$ and $\sigma_t^2$ in the narrowband case, for which $\bar{c} = \bar{t} f_c$ and $\sigma_c^2 = \sigma_t^2 f_c^2$).

As described in [1, Sect. 8.5.3.1], the following forms were derived for frequency-modulated pulses having the form

$$\mathring{s}(t) = a(t) e^{j\phi(t)} \tag{10}$$

where the amplitude $a(t)$ [unitless][8] is assumed to vary slowly over time and the phase $\phi(t)$ [units: rad] can be differentiated to obtain the instantaneous frequency: $f(t) = \phi'(t)/(2\pi)$ [units: Hz]. The average and power of the instantaneous frequency of the signal are

$$\bar{f} = \frac{\int_{-\infty}^{\infty} f(t) |\mathring{s}(t)|^2 \, \mathrm{d}t}{\int_{-\infty}^{\infty} |\mathring{s}(t)|^2 \, \mathrm{d}t} \quad \text{[units: Hz]} \quad \text{and} \quad P_f = \frac{\int_{-\infty}^{\infty} f^2(t) |\mathring{s}(t)|^2 \, \mathrm{d}t}{\int_{-\infty}^{\infty} |\mathring{s}(t)|^2 \, \mathrm{d}t} \quad \text{[units: Hz}^2\text{]}, \tag{11}$$

respectively, from [1, eq. 8.284] and using [1, eq. 8.280]. The average and power of the time (in units of periods) are

$$\bar{c} = \frac{\int_{-\infty}^{\infty} tf(t) |\mathring{s}(t)|^2 \, \mathrm{d}t}{\int_{-\infty}^{\infty} |\mathring{s}(t)|^2 \, \mathrm{d}t} \quad \text{[unitless]} \quad \text{and} \quad P_c = \frac{\int_{-\infty}^{\infty} [tf(t)]^2 |\mathring{s}(t)|^2 \, \mathrm{d}t}{\int_{-\infty}^{\infty} |\mathring{s}(t)|^2 \, \mathrm{d}t} \quad \text{[unitless]}, \tag{12}$$

respectively, from [1, eq. 8.296] and using [1, eq. 8.299]. The coupling between the instantaneous frequency and time (in units of periods) of the waveform is captured by the correlation parameter

$$\bar{r} = \frac{\int_{-\infty}^{\infty} tf^2(t) |\mathring{s}(t)|^2 \, \mathrm{d}t}{\int_{-\infty}^{\infty} |\mathring{s}(t)|^2 \, \mathrm{d}t} \quad \text{[units: Hz]}. \tag{13}$$

The above parameters are then used to form the variance of the instantaneous frequency,

$$\sigma_f^2 = P_f - \bar{f}^2 \quad \text{[units: Hz}^2\text{]}, \tag{14}$$

[8] The scaling described in (6) implies $a(t)$ is unitless.

the variance of the time (in units of periods),

$$\sigma_c^2 = P_c - \bar{c}^2 \quad \text{[unitless]}, \tag{15}$$

and the correlation coefficient between the parameters,

$$\rho = \frac{\bar{r} - \bar{c}\bar{f}}{\sigma_c \sigma_f} \quad \text{[unitless]}. \tag{16}$$

From (10) it can be seen that $|\mathring{s}(t)|^2 = a^2(t)$. For a constant-envelope pulse, this simplifies the integrands in the above equations to only the $t$ and/or $f(t)$ components, limits the integral to the temporal support of the pulse (e.g., $t \in [-T_p/2, T_p/2]$), and forms an average by introducing a $T_p$ in the denominator. For example, a constant-envelope waveform results in

$$\bar{f} = \frac{1}{T_p} \int_{-T_p/2}^{T_p/2} f(t)\, \mathrm{d}t \quad \text{[units: Hz]} \tag{17}$$

for the average frequency. Although it is feasible to derive the results for some of the common amplitude shadings, it is also straightforward to evaluate shaded waveforms through numerical integrals. In these scenarios, including the derivative of the amplitude (as is done in [3, pg. 188]) can provide a more accurate bound. However, these may not be of practical utility when the derivative-based components dominate the result as it implies the amplitude shading provides the key information required for parameter estimation (e.g., using the onset time of a signal before matched filtering to estimate time delay).

When deriving the characteristic time-frequency parameters from the broadband formulations, the time origin of the pulse plays a subtle role. The time delay being estimated is that corresponding to when the part of the pulse at its temporal origin reflects off the OOI. For example, if the time origin is the beginning of the pulse, the time delay (and corresponding range estimate) represent when the pulse first encounters the OOI. In Sect. 3.1, where multiple pulses are first considered, this time is described as the onset of a (hypothetical) reference pulse.

For waveforms with time-varying frequency content, the results for $\bar{c}$, $\sigma_c^2$, and $\rho$ depend on the time origin. In this report, the time origin has been defined as the center of the pulse so its temporal support is on $[-T_p/2, T_p/2]$. Note that the results in [1, Sect. 8.5] utilize the beginning of the pulse. As seen in the following sections, using the center of the pulse results in similar forms for up- and down-sweeping pulses (other than a difference in sign) and identical bounds. Placing the time origin at the beginning of the pulse results in different performance bounds on time-delay estimation for up- and down-sweeping LFM and HFM pulses. Equations for the characteristic time-frequency parameters when the time origin is shifted from the center of the pulse are presented in Sect. 4.4.

### 2.3.1 Basic waveform types (CW, LFM, & HFM)

The primary sensing waveforms in active sonar systems are the continuous-wave (CW) pulse, the linear-frequency-modulated (LFM) pulse, and the hyperbolic-frequency-modulated (HFM) pulse. These can be characterized as special cases of the power-law-frequency-modulated (PLFM) pulses described in [7]. The instantaneous frequency of a PLFM pulse is

$$f(t) = f_0 \left[1 + a\left(t + \frac{T_p}{2}\right)\right]^p \quad \text{[units: Hz]} \quad \text{for} \quad t \in \left[-\frac{T_p}{2}, \frac{T_p}{2}\right] \tag{18}$$

where

$$a = \frac{1}{T_p}\left[\left(\frac{f_1}{f_0}\right)^{1/p} - 1\right] \quad \text{[units: 1/s]}. \tag{19}$$

The pulse starts at frequency $f_0$ when $t = -T_p/2$ and ends at frequency $f_1$ when $t = T_p/2$ with the power-law $p$ characterizing the trajectory. An LFM pulse is obtained by setting $p = 1$, which is seen to produce a linear progression in the instantaneous frequency and a quadratic progression in the phase. An HFM pulse arises when $p = -1$, leading to an instantaneous frequency in the form of a rectangular hyperbola. A CW pulse can be produced by collapsing the bandwidth (i.e., forcing $f_0$ and $f_1$ to tend to $f_c$) while letting $p \to 0$. Up-sweeping pulses have $f_0 < f_1$, whereas down-sweeping pulses require $f_1 < f_0$.

The characteristic time-frequency parameters of the PLFM waveform are presented in Sect. 2.3.2. The results for the basic sonar waveforms (CW, LFM, & HFM), which can be derived from the PLFM results, are presented in Table 1. The LFM results for the frequency average and variation ($\bar{f}$ and $\sigma_f^2$) can be found in [1, Sect. 8.5.3.1]; however, the results related to the time-in-units-of-periods ($\bar{c}$, $\sigma_c^2$, and $\rho$) differ from those in [1, Sect. 8.5.5.1] owing to the different time origin. To cover up- and down-sweeping LFM and HFM pulses, the pulse bandwidth is defined as $W = |f_1 - f_0|$ [units: Hz]. For the LFM, the ratio of the bandwidth to center frequency from [1, Sect. 8.5.5.1] is $\zeta = W/f_c$ [unitless].

### 2.3.2 The power-law frequency-modulated (PLFM) waveform

The time-frequency parameters used in the FIM to characterize the PLFM waveform are obtained by using the instantaneous frequency from (18) in (11)–(13). Before presenting the results, it is convenient to define the parameter

$$\gamma = \left(\frac{f_1}{f_0}\right)^{1/p} = 1 + aT_p \quad \text{[unitless]}. \tag{20}$$

The characteristic time-frequency parameters of the PLFM waveform are then

$$\bar{f} = \frac{\gamma f_1 - f_0}{(p+1)(\gamma - 1)} \quad \text{[units: Hz]}, \tag{21}$$

$$P_f = \frac{\gamma f_1^2 - f_0^2}{(2p+1)(\gamma - 1)} \quad \text{[units: Hz}^2\text{]}, \tag{22}$$

$$\bar{c} = \frac{T_p f_1}{2(p+1)(\gamma-1)}\left[\gamma + \frac{f_0}{f_1} - \frac{2(\gamma^2 - f_0/f_1)}{(p+2)(\gamma-1)}\right] \quad \text{[unitless]}, \tag{23}$$

$$P_c = \frac{T_p^2 f_1^2}{4(2p+1)(\gamma-1)}\left\{\gamma - \frac{f_0^2}{f_1^2} - \frac{2}{(p+1)(\gamma-1)}\left[\gamma^2 + \frac{f_0^2}{f_1^2} - \frac{2(\gamma^3 - f_0^2/f_1^2)}{(2p+3)(\gamma-1)}\right]\right\} \quad \text{[unitless], and} \tag{24}$$

$$\bar{r} = \frac{T_p f_1^2}{2(2p+1)(\gamma-1)}\left[\gamma + \frac{f_0^2}{f_1^2} - \frac{[\gamma^2 - f_0^2/f_1^2]}{(p+1)(\gamma-1)}\right] \quad \text{[units: Hz]}. \tag{25}$$

These equations clearly exclude the $p = -1$ case where there is a $(p+1)$ in the denominator and the $p = -1/2$ case when there is a $(2p+1)$ in the denominator. One approach to obtaining them

Table 1: Characteristic time-frequency parameters used in the CRLB for the standard sonar pulses (CW, LFM, & HFM). All pulses have center frequency $f_c$ [units: Hz] and duration $T_p$ [units: s]. The LFM and HFM pulses start at frequency $f_0$ [units: Hz], end at frequency $f_1$ [units: Hz], and have bandwidth $W = |f_1 - f_0|$ [units: Hz]. Up- and down-sweeping frequency trajectories in the LFM and HFM pulses are indicated by the upper and lower signs in the '$\pm$' and '$\mp$' symbols, respectively. Note that these results are obtained using the approximations for frequency-modulated constant-envelope pulses as described in [1, Sect. 8.5] but use a time origin at the center of the pulse rather than the beginning.

| **Parameter** | **CW pulse** | **LFM pulse** | **HFM pulse** |
|---|---|---|---|
| $f(t)$ for $t \in \left[\frac{-T_p}{2}, \frac{T_p}{2}\right]$ | $f_c$ | $f_c \pm \frac{tW}{T_p}$ | $\frac{f_0 f_1 T_p}{f_c T_p \mp W t}$ |
| $\bar{f}$ | $f_c$ | $\frac{f_0 + f_1}{2} = f_c$ | $\frac{f_0 f_1 \log(f_1/f_0)}{f_1 - f_0}$ |
| $\sigma_f^2$ | 0 | $\frac{W^2}{12}$ | $f_0 f_1 - \bar{f}^2 \left(\approx \frac{W^2}{12} \text{ if } W \ll f_c\right)$ |
| $\bar{c}$ | $\frac{T_p f_c}{2}$ | $\frac{\pm T_p W}{12}$ | $\frac{T_p \bar{f}}{2}\left[\frac{f_1 + f_0}{f_1 - f_0} - \frac{2}{\log(f_1/f_0)}\right]$ |
| $\sigma_c^2$ | $\frac{T_p^2 f_c^2}{12}$ | $\frac{T_p^2 f_c^2}{12}\left(1 + \frac{\zeta^2}{15}\right)$ | $\frac{T_p^2 f_c^2}{12}\left(\frac{\sigma_f^2}{W^2/12}\right)$ |
| $\rho$ | 0 | $\frac{\pm 1}{\sqrt{1 + \zeta^2/15}}$ | $\pm 1 = \text{sign}\{f_1 - f_0\}$ |
| Notes: | | $\zeta = \frac{W}{f_c}$ | |

is to apply L'Hôpital's rule, noting that $\partial\gamma/\partial p = -\gamma \log(f_1/f_0)/p^2$. The results for an HFM pulse ($p = -1$) can also be found in Table 1.

When $p \to 0$ without a corresponding reduction in the bandwidth, the PLFM pulse is essentially a CW pulse at one edge of the frequency band with an infinitesimally small amount of time spent at the other. Taking the limit of $p \to 0$ from above (i.e., $p \searrow 0$) with $f_1 > f_0$, it can be seen that $\gamma \to \infty$. This results in $\bar{f} \to f_1$, $\sigma_f^2 \to p^2 f_1^2 \to 0$, $\sigma_c^2 \to T_p^2 f_1^2/12$, and

$$\rho \to \frac{pT_p f_1^2}{4\sigma_c \sigma_f} \to \frac{\sqrt{3}}{2}, \tag{26}$$

which is not zero (the CW-pulse result) because of the small amount of time the pulse spends at $f_0$. If the limit $p \to 0$ is taken from below ($p \nearrow 0$) with $f_1 > f_0$, the PLFM similarly simplifies to a CW pulse at frequency $f_0$ while spending an infinitesimally small amount of time at $f_1$. To properly obtain a CW pulse at $f_c$ from the PLFM framework, the frequency band must also be collapsed about $f_c$ as $p \to 0$.

## 2.4 Single-pulse bounds for estimation of time delay (range) and Doppler scale (radial velocity)

The single-pulse bounds presented here are from [1, Sect. 8.5.5], which utilizes the deterministic signal model and accounts for the waveform being broadband. The latter requires use of Doppler scale as a parameter rather than the frequency shift found under the narrowband assumption. The Cramér-Rao lower bounds on estimation of radial velocity or delay are formed from the Fisher information matrix (FIM), which has a dimension equal to the number of unknown parameters in the statistical model of the measurement. As described in [1, pg. 535, Table 8.6], the amplitude and the noise variance are uncoupled from the other parameters (i.e., any cross terms containing them are zero) and therefore can be excluded from the analysis. For a deterministic signal in Gaussian noise, this leaves the time delay ($\tau$), the Doppler scale ($\eta$), and the bulk phase ($\psi$) as the relevant unknown parameters.

The FIM for joint estimation of delay, Doppler scale, and bulk phase for this scenario is

$$\mathrm{FIM}(\tau, \eta, \psi) = 8\pi^2 S^{\mathrm{d}} \begin{bmatrix} P_f & -\bar{r} & -\bar{f}/(2\pi) \\ -\bar{r} & P_c & \bar{c}/(2\pi) \\ -\bar{f}/(2\pi) & \bar{c}/(2\pi) & 1/(4\pi^2) \end{bmatrix}, \tag{27}$$

where the parameters, which are described in Sect. 2.3, represent time-frequency characteristics of the waveform. Note that this differs slightly from the FIM found in [1, pg. 559, eq. 8.314] in that the average frequency of the analytic signal is used rather than that of the complex envelope (see footnote 5). However, the two-by-two partition of the inverse of the FIM associated with $\tau$ and $\eta$ is the same as that found in [1, eq. 8.315],

$$\left\{\mathrm{FIM}^{-1}(\tau, \eta, \psi)\right\}_{\tau,\eta} = \frac{\begin{bmatrix} \frac{1}{\sigma_f^2} & \frac{\rho}{\sigma_c \sigma_f} \\ \frac{\rho}{\sigma_c \sigma_f} & \frac{1}{\sigma_c^2} \end{bmatrix}}{8\pi^2 S^{\mathrm{d}}(1-\rho^2)}. \tag{28}$$

As described in [1, Sect. 6.3.3.1], the diagonal terms in (28) provide lower bounds on the variance of unbiased estimates of the unknown parameters, yielding

$$\mathrm{Var}\{\hat{\tau}\} \geq \frac{1}{8\pi^2 S^{\mathrm{d}} \sigma_f^2 (1-\rho^2)} \quad \text{[units: s}^2\text{]} \tag{29}$$

from [1, eq. 8.316] for the time delay and

$$\mathrm{Var}\{\hat{\eta}\} \geq \frac{1}{8\pi^2 S^{\mathrm{d}} \sigma_c^2 (1-\rho^2)} \quad \text{[unitless]} \tag{30}$$

from [1, eq. 8.317] for the Doppler scale. The CRLBs on delay and Doppler scale can be converted to range and radial velocity, respectively, by multiplying (29) and (30) by $c_w^2/4$, which is the squared derivative of the transformed parameter with respect to the original (recall that $r = \tau c_w/2$ and $v = (\eta - 1)c_w/2$). For example, the bound for radial-velocity estimation is

$$\mathrm{Var}\{\hat{v}\} \geq \frac{c_w^2}{32\pi^2 S^{\mathrm{d}} \sigma_c^2 (1-\rho^2)} \quad \text{[units: m}^2\text{/s}^2\text{]}. \tag{31}$$

It is interesting to contrast these results to those assuming one of the parameters is known. When Doppler scale is known, the CRLB for time-delay estimation is $1/(8\pi^2 S^{\mathrm{d}} \sigma_f^2)$ from [1, pg. 549, eq. 8.270]. This is obtained from the FIM in (27) by removing the row and column associated with $\eta$ and then taking the diagonal term related to $\tau$ in the inverse of the resulting two-by-two matrix. The result for estimating Doppler scale when time delay is known is similarly $1/(8\pi^2 S^{\mathrm{d}} \sigma_c^2)$ from [1, pg. 555, eq. 8.301] or by following the above procedure with (27) when removing the row and column associated with $\tau$. It can also be seen that these results are identical to when both parameters are unknown and there is no coupling between time and frequency in the pulse, which is represented by the parameter $\rho$ being equal to zero. Noting that $\rho \in [-1, 1]$, this result reinforces the expectation that performance can only degrade when an additional coupled parameter (i.e., $\rho \neq 0$) is treated as unknown.

The remainder of this section presents the CRLBs on radial-velocity and time-delay estimation for the basic sonar pulses (CW, LFM, & HFM) when one parameter is known (Sect. 2.4.1) and when both parameters are unknown (Sect. 2.4.2). The depictions of the waveform ambiguity functions found in Fig. 1 can be useful in discerning where each waveform excels or struggles. These cartoons illustrate the general shape of the ambiguity function; see [1, Sect. 8.3] for specific examples. Ambiguity functions have a peak at the origin, where the signal echo and matched-filter replica are identical. The decay from the origin generally occurs with sidelobes (i.e., not monotonically), which can be nearly as high as the peak in some waveforms. As seen in Fig. 1, the decay is not necessarily identical in every direction. Here the ambiguity functions provide insight into how performance changes when the Doppler and time-delay parameters are both unknown compared to when one is known. If one parameter is known, the performance is driven by the decay of the ambiguity function in the dimension of the unknown parameter. When both parameters are unknown, estimation performance for the FM waveforms is driven by the slow decay along the slanted ridge of the ambiguity function for both time delay and Doppler owing to the coupling. However, for the CW pulse it can be seen that errors in time-delay estimation do not degrade performance for radial-velocity estimation and vice versa.

### 2.4.1 Basic sonar pulses when one parameter is known

The CRLB for estimating radial velocity or time delay using a single pulse is presented here when the alternative parameter is known. For example, the relative radial velocity of an OOI is known to be zero if it and the sensing platform are stationary and the time delay must be estimated if the OOI is at an unknown range. Although examples of radial-velocity estimation when time delay is known are rare, the results found here can still be useful when the time and frequency dimensions are uncoupled or as lower bounds on performance when both parameters are unknown, noting that they might not be particularly tight. The bounds obtained when both parameters are unknown are presented in Sect. 2.4.2.

The relevant characteristic time-frequency parameters ($\sigma_c^2$ and $\sigma_f^2$) for the basic sonar pulses are obtained from Table 1 (pg. 16). The underlying parameters required to define the time-frequency parameters and the CRLBs for these waveforms are

- the pulse duration, $T_p$ [units: s],
- the pulse bandwidth, $W$ [units: Hz],
- the center frequency of the pulse, $f_c$ [units: Hz],
- the speed of sound, $c_w$ [units: m/s], and
- the SNR after coherent detection processing, $S^{\mathrm{d}}$ [unitless].

A specific definition for the SNR after coherent detection processing using terms from the sonar equation was presented in Sect. 2.2.2.

**CW Pulses:** For the CW pulse, there is no time-frequency coupling (i.e., $\rho = 0$), which implies the bounds are the same when one or both of the parameters (time delay and radial velocity) are unknown. As seen in Fig. 1, the ambiguity function of a long-duration CW pulse is narrow in the Doppler dimension and broad in time delay. This implies that it is useful for estimating radial velocity but may not excel at time-delay estimation unless it is short in duration, in which case it is a poor estimator of velocity. Using $\sigma_c^2 = f_c^2 T_p^2/12$ from Table 1 (pg. 16) for the CW pulse, the CRLB on radial-velocity estimation is seen to be

$$\mathrm{Var}\{\hat{v}\} \geq \frac{3c_w^2}{8\pi^2 S^{\mathrm{d}} T_p^2 f_c^2} \quad \text{[units: m}^2\text{/s}^2\text{]}. \tag{32}$$

Recall that this is obtained by multiplying the bound for Doppler scale by $c_w^2/4$ to account for the transformation. As expected, this result illustrates how increasing SNR, pulse duration, or center frequency improves estimation of radial velocity. In some applications, this can be driven below the Doppler spreading induced by random motion of the ocean boundaries, sonar platform or OOI.

The CRLB shown in (32) can be placed into perspective by describing it in terms of the Rayleigh resolution [1, Sect. 8.5.1], which is the distance from the peak to the first zero in the average response function. For a CW pulse, this is easily understood to be a Doppler shift in frequency equal to $1/T_p$ [units: Hz], which maps to a radial velocity of

$$v_{\mathrm{Ray}} = \frac{c_w}{2 f_c T_p} \quad \text{[units: m/s]} \tag{33}$$

for two-way monostatic sensing. Using this in (32) and taking the square root to describe a bound on the standard deviation of the estimator results in

$$\mathrm{Std}\{\hat{v}\} \geq \frac{v_{\mathrm{Ray}}}{2.56\sqrt{S^{\mathrm{d}}}} \quad \text{[units: m/s]}. \tag{34}$$

Similar to the time-delay-estimation example in [1, Sect. 8.5.1.2], this illustrates how the CRLB characterizes accuracy in the estimation (of unbiased estimators) as opposed to the resolution, which is a more rudimentary measure. A high SNR enables estimation accuracy significantly below the Rayleigh resolution

For the CW pulse, the "frequency-variation" parameter is zero ($\sigma_f^2 = 0\,\mathrm{Hz}^2$) when it is constructed from the instantaneous frequency, which implies the CRLB for time-delay estimation (e.g., (29) with $\rho = 0$) is infinite. This does not imply that time delay cannot be estimated from CW-pulse echoes, only that the regularity conditions required by the CRLB are not satisfied and so it does not apply. Modifying the pulse through amplitude modulation (e.g., tapering the pulse at its beginning and end, for which the characteristic time-frequency parameters can be found in [3, Sect. 4.4.1]) or restricting the frequency content (e.g., see the example in [1, Sect. 8.5.3.2]) can yield values of $\sigma_f^2 > 0\,\mathrm{Hz}^2$ that capture some of the pertinent relationships (e.g., proportionality to the squared pulse duration and inverse dependence on SNR; i.e., the CRLB is $\propto T_p^2/S^{\mathrm{d}}$). However, they may not be particularly tight lower bounds.[9]

Evaluation of other bounds (e.g., Barankin bounds in [26] or Ziv-Zakai bounds in [27]) exhibits a similar dependence on pulse duration, but yields an inverse dependence on the squared SNR. For example, the Ziv-Zakai bound is

$$\mathrm{Var}\{\hat{\tau}\} \geq 1.62\left[\frac{T_p}{S^{\mathrm{d}}}\right]^2 \quad \text{[units: s}^2\text{]} \;\text{ for }\; S^{\mathrm{d}} > 6.48 \approx 8.1\,\mathrm{dB}, \tag{35}$$

from [27, pg. 389]. This proportionality to $[T_p/S^{\mathrm{d}}]^2$ is also seen in the approximations of [19, App. I] where the probability density function of the time-delay estimation error was approximated as following a double-exponential or Laplace distribution with a variance equal to $0.5[T_p/S^{\mathrm{d}}]^2$ [units: s$^2$]. This illustrates an important impact of scenarios for which the CRLB does not exist: the asymptotic distribution of the estimator is not necessarily Gaussian (see some additional discussion of this topic in Sect. 2.4.2 under HFM pulses).

In noise-limited scenarios, $S^{\mathrm{d}}$ is proportional to $T_p$ and the source factor[10] for a constant-envelope pulse. This implies that effective time-delay estimation from CW pulses requires a high source level and to a lesser degree short pulses (the inverse dependence on $S^{\mathrm{d}}$ in the Ziv-Zakai bound [27] was not as strong as squaring when the SNR was below 8.1 dB). When time-delay estimation is paramount and the source level cannot be made high enough to provide adequate SNR after matched filtering for the ranges of interest, one typically needs to utilize LFM or HFM pulses.

[9] For example, bounds for CW time-delay estimation formed through amplitude shading suggest the information comes from sharp transitions such as at the beginning and end of the pulse. Estimating time delay from the onset of an echo, however, does not exploit matched filtering where a high SNR can equate to many observations and therefore be representative of asymptotic conditions. This suggests that the estimator may be far from efficient; i.e., that CRLB is not necessarily tight.

[10] The source factor is the linear quantity formed from the logarithmic source-level term in the sonar equation; see Sect. 2.2.2, [28, Sect. 3.2.2] or [1, Sect. 3.2.3.4].

**LFM Pulses:** For an LFM pulse, the frequency-variation parameter from Table 1 (pg. 16) is $\sigma_f^2 = W^2/12$ [units: Hz$^2$], which results in the lower bound

$$\mathrm{Var}\{\hat{\tau}\} \geq \frac{3}{2\pi^2 S^{\mathrm{d}} W^2} \quad \text{[units: s}^2\text{]} \tag{36}$$

on time-delay estimation when radial velocity is known. Compared to the CW-pulse bound in (35), bandwidth can be increased to improve estimation performance without altering SNR in noise-limited scenarios. This makes broadband pulses a popular choice when time-delay estimation is paramount.

Using the value of $\sigma_c^2 = T_p^2 f_c^2 (1 + \zeta^2/15)/12$ [unitless] from Table 1 (pg. 16) with $\zeta = W/f_c$ for the LFM pulse results in

$$\mathrm{Var}\{\hat{v}\} \geq \frac{3c_w^2}{8\pi^2 S^{\mathrm{d}} T_p^2 (f_c^2 + W^2/15)} \quad \text{[units: m}^2\text{/s}^2\text{]} \tag{37}$$

as the CRLB on radial-velocity estimation when time delay is known. Setting the bandwidth $W$ to zero causes (37) to simplify to the CW result in (32). Similar to the CW pulse, the bound here is essentially inversely proportional to $S^{\mathrm{d}}(T_p f_c)^2$, indicating SNR, pulse duration and center frequency drive performance.

In both of these cases, the assumed knowledge of the alternative parameter implies performance depends on how the ambiguity function decays from the origin in the dimension of the unknown parameter. As seen in Fig. 1, this is narrow in both dimensions for the LFM and HFM pulses. However, the requirement that one parameter be known limits the utility of this result because it is usually not satisfied.

A case where the bound on time-delay estimation in (36) can be applied when both range and radial velocity are unknown arises when estimation is performed using time delays over multiple consecutive pulses. By exploiting the Doppler tolerance of the LFM or HFM waveform, detection and biased time-delay estimation can be performed using a single matched filter. Mismatch in Doppler between the echo and the replica results in a small loss in SNR and a bias in the time-delay estimates. In terms of the ambiguity functions in Fig. 1, the decay in the temporal dimension at a Doppler corresponding to the mismatch drives the estimation performance. Transmitting the same pulse multiple times then allows estimating both the radial velocity and an unbiased time delay. The performance of these estimators is examined in Sect. 3.

**HFM Pulses:** It can be seen from the equations for $\sigma_f^2$ and $\sigma_c^2$ in Table 1 (pg. 16) that the HFM pulse yields approximately the same performance as the LFM when the bandwidth is small compared to the center frequency. In these scenarios, the result in (36) can be used for estimating time delay. For estimating radial velocity, it is better to use the approximation $\sigma_f^2 \approx W^2/12$ to obtain $\sigma_c^2 \approx T_p^2 f_c^2/12$, which produces the same bound as that found in (32) for the CW pulse. With these approximations, the relative absolute errors are less than 10% when $\zeta \leq 0.8$.

### 2.4.2 Basic sonar pulses when both radial velocity and time delay are unknown

CRLBs for the joint estimation of radial velocity and time delay are presented in this section when using a single basic sonar pulse. The relevant characteristic time-frequency parameters ($\sigma_c^2$, $\sigma_f^2$ and $\rho$) are obtained from Table 1 (pg. 16).

**CW Pulses:** As previously noted, the time-delay and radial-velocity parameters are decoupled (i.e., $\rho = 0$) for CW pulses. This implies the CRLBs for their joint estimation are the same as those described in Sect. 2.4.1 when assuming the alternate parameter is known.

**LFM Pulses:** The ambiguity function for the LFM pulse seen in Fig. 1 illustrates the classic coupling [29] between time delay and Doppler for which LFM and HFM waveforms are known. It can also be seen that the LFM pulse is subject to some spreading when the echo and replica are mismatched in Doppler. Although this can degrade detection performance when there is mismatch in Doppler, it is indicative of improved joint estimation of time delay and Doppler relative to the HFM pulse. From [30, eqs. 9 & 10], the "Doppler tolerance" (essentially defined in [30] as the distance in Doppler from the peak to the 3-dB-down point along the ridge in the ambiguity function) is

$$v^{\star} = \pm\frac{1.74}{WT_p}\cdot\frac{c_w}{2} \quad \approx \pm\frac{2600}{WT_p} \quad \text{[units: kn]} \quad \approx \pm\frac{1300}{WT_p} \quad \text{[units: m/s]}, \tag{38}$$

which shows that useful Doppler sensitivity from the LFM pulse requires a high time-bandwidth product.

Using the values of $\sigma_f^2$ and $\rho$ from Table 1 (pg. 16) for the LFM pulse, the CRLB on time-delay estimation when radial velocity is also unknown can be shown to result in

$$\mathrm{Var}\{\hat{\tau}\} \geq \left[\frac{3}{2\pi^2 S^{\mathrm{d}} W^2}\right]\left[1+\frac{15f_c^2}{W^2}\right] \quad \text{[units: s}^2\text{]}, \tag{39}$$

where the first term in brackets is the bound when radial velocity is known from (36). This relationship illustrates the degradation in performance when it is necessary to estimate both parameters—a multiplicative factor large enough to make relying on a single LFM pulse to obtain an unbiased estimate of time delay (when radial velocity is unknown) a poor design choice except when the bandwidth-to-center-frequency ratio is large.

The CRLB for radial-velocity estimation when delay is also unknown can be shown to be

$$\mathrm{Var}\{\hat{v}\} \geq \frac{45c_w^2}{8\pi^2 S^{\mathrm{d}} T_p^2 W^2} \quad \text{[units: m}^2\text{/s}^2\text{]}, \tag{40}$$

which illustrates an inverse dependence on bandwidth. Similar to the construction of the bound in (39), which was for estimating time delay, (40) can be re-written as

$$\mathrm{Var}\{\hat{v}\} \geq \left[\frac{3c_w^2}{8\pi^2 S^{\mathrm{d}} T_p^2 (f_c^2 + W^2/15)}\right]\left[1+\frac{15f_c^2}{W^2}\right] \quad \text{[units: m}^2\text{/s}^2\text{]}, \tag{41}$$

which is the product of the bound from (37) for estimating radial velocity when time delay is known (the first term in brackets) and $1+15f_c^2/W^2$. As might be expected, the CRLB in (40) has a similar relationship to the resolution capability of the waveform (e.g., using (38)) and SNR as that seen for the CW pulse in (34). Compared to the improvement seen in (32) with center frequency for a CW pulse, the LFM pulse is driven here by bandwidth and starts out with a much larger constant in the numerator (45 versus 3). A CW pulse with equivalent signal statistics, SNR, duration, and center frequency will always have a lower CRLB for radial-velocity estimation.

This significant degradation in estimation performance is explained by the ambiguity function in Fig. 1 where joint estimation of the parameters is driven by the slow decay along the ridge as opposed to the rapid decay seen in either dimension when the alternate parameter is known. This coupling between time delay and radial velocity results in a large magnitude for the time-frequency correlation parameter,

$$\rho = \frac{\pm 1}{\sqrt{1 + \frac{W^2}{15 f_c^2}}}, \tag{42}$$

where the upper and lower symbols in '±' indicate, respectively, an up-sweeping or down-sweeping trajectory of the instantaneous frequency. From (42), it can be seen that $\rho$ has a minimum magnitude of $|\rho| > \sqrt{15/19} \approx 0.89$ for the centered time-delay estimator achieved in the limit as the bandwidth increases to $2f_c$. At the other extreme, $\rho$ tends to a magnitude of one as the bandwidth is reduced to zero. In this limit ($W \to 0\,\text{Hz}$ and $|\rho| \to 1$), one of the eigenvalues in the Fisher information matrix in (27) tends to zero, so the matrix becomes singular and is not invertible, violating the regularity conditions [31, Sect. 17.14] required by the CRLB. A similar problem is encountered by the HFM pulse, but for all bandwidths.

**HFM Pulses:** The HFM pulse has been described as "optimally Doppler tolerant" [5,6] because the Doppler scale induced by constant radial velocity does not alter the shape of the instantaneous frequency, but only its starting and stopping frequency (e.g., see [1, pg. 463, Fig. 8.4]). The loss incurred by mismatch in Doppler between an echo and the replica in a matched filter then comes from a reduction in the effective pulse duration and bandwidth as a result of the reduced overlap. In the LFM pulse, Doppler mismatch also has the effect of changing the slope of the instantaneous frequency and therefore incurs an additional mismatch loss with the benefit of better estimation of radial velocity. Although the optimal Doppler tolerance of the HFM pulse is a boon for detection, it results in full coupling ($\rho = \pm 1$) between time delay and radial velocity at all bandwidths. This causes the CRLBs in (29) and (30) to be infinite, because the regularity conditions [31, Sect. 17.14] required for the CRLB to exist are not satisfied. In particular, the derivative of the likelihood function with respect to $\eta$ does not exist at its true value. This is most clearly seen when the characteristic parameters are written in terms of derivatives of the ambiguity function.[11] In this case, the envelope of the HFM ambiguity function in the Doppler-scale dimension decays from the origin with the form of a triangle function, which is not differentiable at its peak.

Similar to the discussion of estimating time delay with a CW pulse in Sect. 2.4.1, this does not mean that time delay and radial velocity cannot be jointly estimated from an HFM waveform. There are, however, implications with respect to how the errors are characterized. First, bounds on the variance must be obtained using other techniques (e.g., those from Barankin [32] or Ziv and Zakai [27]). Second, the existence of the CRLB carries with it the knowledge that maximum-likelihood estimates will tend to Gaussian distributions asymptotically as the number of samples increases [13, Sect. 7.5] with a variance defined by the CRLB. In the present scenario, the asymptotic condition can be used as an approximation for very high SNR (i.e., a single observation at a very high SNR can often be interpreted as many observations of weak signals). Because the CRLBs exist for the LFM waveform, the time-delay and radial-velocity estimates can be approximated as jointly Gaussian distributed, as was done in the example in [1, Sect. 8.5.5.1] to form a confidence

[11] See [18, pg. 300, Property 2] for the narrowband case or [1, pg. 549] for the broadband case for $\bar{f}$ and $\sigma_f^2$. The broadband case for $\bar{c}$, $\sigma_c^2$, and $\rho$ can be derived from [1, eq. 8.272].

ellipse. When the SNR is not high enough for the performance to be represented by the asymptotic distribution, a multivariate $t$-distribution with a shape parameter causing it to tend to a multivariate Gaussian distribution as SNR increases to infinity is an appropriate alternative.

When the CRLB does not exist, it is not clear what the asymptotic distribution might be. However, an analysis of delay estimation using a CW pulse (for which the ambiguity function falls off in the form of a triangle function) in [19, App. I] suggests the errors will, to first order, follow a double-exponential (i.e., Laplace) distribution. Although performance will improve with SNR, the errors will always be heavier tailed than Gaussian. When the SNR is not asymptotically high, a double-Weibull distribution designed to tend to a double-exponential distribution with increasing SNR is a reasonable alternative.

### 2.4.3 Modifications for one-way and bistatic propagation

In applications where there is only one-way propagation or in a bistatic geometry where the projector (source) and sensor array (receiver) are not co-located, the results in this report can be applied after appropriately considering the relationship between the Doppler scale in the measurement and the velocity being estimated.

For one-way propagation, the Doppler scale observed at the receiver is [1, pg. 52, eq. 2.26],

$$\eta_{\text{1-way}} = \frac{c_w - v_\text{r}}{c_w - v_\text{s}} \approx 1 + \frac{v}{c_w} \quad \text{[unitless]}, \tag{43}$$

where, similar to the descriptions in Sect. 2.1, $v_\text{s}$ is the radial velocity of the source platform, $v_\text{r}$ is the radial velocity of the receiver platform, and $v = v_\text{s} - v_\text{r}$ is the relative radial velocity. Solving this for relative radial velocity results in

$$v = c_w(\eta_{\text{1-way}} - 1) \quad \text{[units: m/s]}. \tag{44}$$

Using $\partial v/\partial \eta_{\text{1-way}} = c_w$, the CRLBs on the relative radial velocity estimated from a one-way observation can be obtained by multiplying the bounds on estimating $\eta$ found elsewhere in this report by $c_w^2$. Compared to the monostatic two-way scenario, which requires multiplication by $c_w^2/4$, these bounds on the variance are four times larger, as might be expected when halving the travel time of the measurement.

For bistatic sensing geometries, the relationship between Doppler scale and the velocity being estimated can be obtained from [33, eq. 9],

$$\eta_\text{bi} = \frac{(c_w + V_o \cos\theta_{o\text{s}})(c_w + V_\text{r} \cos\theta_{\text{r}o})}{(c_w - V_\text{s} \cos\theta_{\text{s}o})(c_w - V_o \cos\theta_{o\text{r}})} \quad \text{[unitless]}, \tag{45}$$

where the capital letters $V_\text{s}$, $V_\text{r}$ and $V_o$ [units: m/s] represent platform speeds, and the angle $\theta_{xy}$ [units: rad] is between the heading of platform $x$ and the angle pointing to platform $y$. The first-order Maclaurin-series approximation to (45) can be described as

$$\eta_\text{bi} \approx 1 + \frac{2\bar{v}_o}{c_w} + \frac{V_\text{s} \cos\theta_{\text{s}o}}{c_w} + \frac{V_\text{r} \cos\theta_{\text{r}o}}{c_w} \quad \text{[unitless]}, \tag{46}$$

where $\bar{v}_o$ [units: m/s] is the combined contribution of the OOI in the two different radials pointing toward the source and receiver. From [33, eq. 12], it is

$$\bar{v}_o = V_o \cos(\theta_{o\beta}) \cos(\beta/2) \quad \text{[units: m/s]} \tag{47}$$

where $\theta_{o\beta} = (\theta_{o\mathrm{s}} + \theta_{o\mathrm{r}})/2$ [units: rad] is the angle from the OOI heading to the bisector between the angles pointing to the source and receiver, and $\beta = \theta_{o\mathrm{s}} - \theta_{o\mathrm{r}}$ [units: rad] is the bistatic angle.

The contributions to (46) from the source and receiver are typically known, which allows estimation of $\bar{v}_o$ from the Doppler scale in the echo measured at a bistatic receiver. The partial derivative of $\bar{v}_o$ with respect to $\eta_{\mathrm{bi}}$ is the same as that for the two-way monostatic geometry (i.e., $c_w/2$), which implies the bounds on its estimation are the same as those found throughout this report.

### 2.4.4 Accounting for estimation of the angle of arrival

Many sonar systems include estimation of the arrival angle of the echo at a sensor array, which is (in general) the two-dimensional vector $\boldsymbol{\theta} = [\theta \;\; \phi]^T$ containing the azimuthal angle $\theta$ [units: rad] and the elevation angle $\phi$ [units: rad]. In this section, the CRLB analysis presented in Sect. 2.4 is extended to account for estimating one of the angles ($\theta$) under the assumption that the other is known. To simplify notation, dependence on $\phi$ is suppressed. As will be seen, the impact of simultaneously estimating the two angles can be assessed from these results. This analysis is also limited to scenarios for which the signal is narrowband with respect to the array processing and when the noise across the sensor array is independent. The general case of spatially correlated noise can be found in [15]. To maintain consistency with earlier definitions, let $S^{\mathrm{d}} = A^2/\lambda$ be the SNR after both beamforming and coherent detection processing, which implies that for a single sensor the signal amplitude is $A/N$ and the noise variance is $\lambda/N$, where $N$ is the array gain ($G^{\mathrm{a}}$), which is interpreted here as the size of the array in terms of the number of sensors exhibiting mutually independent noise. The signal observed on the $n$th sensor of $N$ is then described by extending (5) to

$$\tilde{u}_n(t) = \tfrac{A}{N} e^{j\psi} \mathring{s}(\eta[t - \tau - \alpha_n(\theta)])\, e^{-j\omega_c t}, \tag{48}$$

where $\alpha_n(\theta)$ [units: s] is an additional delay term that depends on the angle at which the echo impinges on the sensor array. The beamforming operation corrects for these delays and sums over the $N$ sensors to form (5), where the beam-output noise variance is $\lambda$. The pertinent modification of (5), however, comes from the delay terms describing which part of the echo is observed at each sensor. For example, the delays for a uniformly spaced linear array (ULA) are

$$\alpha_n(\theta) = \frac{(n - \bar{n}) d \cos\theta}{c_w} \quad \text{[units: s]} \tag{49}$$

for $n = 0,\ldots,N-1$, where $d$ [units: m] is the inter-sensor spacing and the array is placed in the horizontal plane so $\theta$ is also the conical angle of the wavefront impinging on the array ($\theta = 0\,\mathrm{rad}$ is forward array end-fire). The value of $\bar{n}$ dictates the origin of the array, which is the location for which the beamforming operation reconstructs the signal. It is often either one of the sensors (e.g., $\bar{n} = 0$ for the first sensor) or the geometric center of the array ($\bar{n} = (N-1)/2$).

In the basic analysis presented here, the sensors are assumed to be placed so that the noise observed on them is independent, as occurs in the ULA when the sensors are spaced every half wavelength, $d = \lambda_d/2$, where $\lambda_d = c_w/f_c$ [units: m] is the wavelength at the design frequency of the line array, which here is taken as the center frequency of the signal owing to the narrowband assumption. This simplifies (49) to

$$\alpha_n(\theta) = \frac{(n - \bar{n}) \cos\theta}{2 f_c} \quad \text{[units: s]}, \tag{50}$$

which now only depends on the angle of arrival and center frequency.

The CRLBs are derived as described in [1, Sect. 8.5.3–8.5.5] by first forming the Fisher information matrix (FIM). In addition to the partial derivatives with respect to time delay, Doppler scale and bulk phase, this requires use of the partial derivative of (48) with respect to $\theta$,

$$\frac{\partial \tilde{u}_n(t)}{\partial \theta} = -j \frac{\partial \alpha_n(\theta)}{\partial \theta} 2\pi f(t) \tilde{u}_n(t), \tag{51}$$

which includes evaluation at the true values of the parameters. Independence of the noise across the sensors allows forming the FIM simply by summing the single-sensor FIMs. This has the effect of accruing the terms

$$a_n = \frac{\partial \alpha_n(\theta)}{\partial \theta} \quad \text{[units: s/rad]}, \tag{52}$$

which represent the sensitivity of the time delays to arrival angle. Similar to the characteristic time-frequency parameters described in Sect. 2.3, the array delay sensitivities require the average,

$$\bar{a} = \frac{1}{N} \sum_{n=0}^{N-1} \frac{\partial \alpha_n(\theta)}{\partial \theta} \quad \text{[units: s/rad]} \tag{53}$$

and the average power,

$$P_a = \frac{1}{N} \sum_{n=0}^{N-1} \left[ \frac{\partial \alpha_n(\theta)}{\partial \theta} \right]^2 \quad \text{[units: s}^2\text{/rad}^2\text{]}. \tag{54}$$

The variance of the sensitivities is $\sigma_a^2 = P_a - \bar{a}^2$ [units: s$^2$/rad$^2$]. When the OOI is in the far-field of the sensor array, the acoustic waves carrying the echo can be assumed to be planar, for which the delay affecting the $n$th sensor is

$$\alpha_n(\theta) = \vec{u}(\boldsymbol{\theta}) \cdot \frac{(\vec{x}_\mathrm{o} - \vec{x}_n)}{c_w} \quad \text{[units: s]}, \tag{55}$$

where $\vec{u}(\boldsymbol{\theta})$ is a three-dimensional unit vector pointing in azimuth and elevation toward the OOI, $\vec{x}_n$ is the position of the $n$th sensor, $\vec{x}_\mathrm{o}$ is the array origin, and '$\cdot$' represents a dot product. By choosing the array origin as the geometric center of the array,

$$\vec{x}_\mathrm{o} = \frac{1}{N} \sum_{n=0}^{N-1} \vec{x}_n \quad \text{[units: m]}, \tag{56}$$

it can be seen that $\bar{a}$ in (53) equals zero, which also causes $P_a$ to equal $\sigma_a^2$. For the ULA with an origin at its geometric center, this results in

$$\sigma_a^2 = \frac{(N^2 - 1) \sin^2 \theta}{48 f_c^2} \quad \text{[units: s}^2\text{/rad}^2\text{]}. \tag{57}$$

The FIM for joint estimation of delay, Doppler scale, arrival angle, and bulk phase for this scenario can be shown to be

$$\mathrm{FIM}(\tau, \eta, \theta, \psi) = 8\pi^2 S^\mathrm{d} \begin{bmatrix} P_f & -\bar{r} & \bar{a}P_f & -\bar{f}/(2\pi) \\ -\bar{r} & P_c & -\bar{a}\bar{r} & \bar{c}/(2\pi) \\ \bar{a}P_f & -\bar{a}\bar{r} & P_a P_f & -\bar{a}\bar{f}/(2\pi) \\ -\bar{f}/(2\pi) & \bar{c}/(2\pi) & -\bar{a}\bar{f}/(2\pi) & 1/(4\pi^2) \end{bmatrix}. \tag{58}$$

Note that removing the third row and third column produces (27), the FIM when $\theta$ is known. When $\bar{a}$ is zero, as it is when the OOI is in the far-field and the array origin is at its geometric center, it is straightforward to see that $\theta$ is decoupled from the other parameters. This implies the results from (29)–(31) apply directly for estimation of delay and Doppler when the arrival angle is unknown and also must be estimated.

When $\bar{a} \neq 0\,\mathrm{s/rad}$, it can be shown[12] that the CRLB for estimating the time delay is

$$\mathrm{Var}\{\hat{\tau}\} \geq \frac{1 + \frac{\bar{a}^2\sigma_f^2(1-\rho^2)}{\sigma_a^2 P_f}}{8\pi^2 S^{\mathrm{d}}\sigma_f^2(1-\rho^2)} \quad [\text{units: } \mathrm{s}^2]. \tag{59}$$

Under the narrowband assumptions made earlier (for which $\sigma_f^2 \ll P_f$), the latter term in the numerator will be small enough to ignore, in which case the result is essentially the same as (29). Interestingly, the coupling arising when $\bar{a} \neq 0\,\mathrm{s/rad}$ has no effect on the CRLBs for Doppler scale,

$$\mathrm{Var}\{\hat{\eta}\} \geq \frac{1}{8\pi^2 S^{\mathrm{d}}\sigma_c^2(1-\rho^2)} \quad [\text{unitless}], \tag{60}$$

which is the same as (30), or angle,

$$\mathrm{Var}\left\{\hat{\theta}\right\} \geq \frac{1}{8\pi^2 S^{\mathrm{d}}\sigma_a^2 P_f} \quad [\text{units: rad}^2], \tag{61}$$

which is seen to equal the inverse of the $(3,3)$ element in (58) when $\bar{a} = 0\,\mathrm{s/rad}$. The off-diagonal entries of the inverse FIM provide an idea of how correlated two parameter estimates will be asymptotically as the number of observations or SNR increases. Even for $\bar{a} \neq 0\,\mathrm{s/rad}$, the covariance between $\hat{\theta}$ and $\hat{\eta}$ is asymptotically zero, implying independence when the estimates are Gaussian distributed. The correlation coefficient (formed by dividing the covariance by the standard deviations of the two estimates) between $\hat{\theta}$ and $\hat{\tau}$ has the limit

$$\rho_{\theta,\tau} \to \frac{-\bar{a}\sqrt{(1-\rho^2)\sigma_f^2}}{\sqrt{\sigma_a^2 P_f + \bar{a}^2(1-\rho^2)\sigma_f^2}}. \quad [\text{unitless}] \tag{62}$$

Even when the array origin is not its geometric center, this is likely to be close to zero given the $\sigma_a^2 P_f$ term in the denominator. Based on these results, the time-delay and Doppler parameters can essentially be treated as uncoupled from arrival angle, implying their estimates will be asymptotically independent.

The above analysis is identical to estimation of the elevation angle $\phi$ when $\theta$ is known—it can similarly be assumed to decouple from $\tau$ and $\eta$. When both angles are unknown, they therefore jointly decouple from the other parameters, but may be coupled themselves (e.g., for a line array the two angles couple so that only the conical angle can be estimated).

[12]The results presented in (59)–(63) were derived by partitioning (58) in a manner similar to that described in App. A.2 (i.e., using (A24)) with a three-by-three matrix in the upper left corner and using (A25)) to describe the upper-left sub-matrix of the inverse FIM as $\mathbf{G}$. The elements of the inverse FIM are then obtained from $\mathbf{G}^{-1}$, which is easily characterized from (58), using the corresponding terms of the cofactor and the determinant of the matrix as described in [34, Sect. 4.4].

Although it is not a focus of this report, the CRLB for estimating arrival angle with a ULA can be obtained by using (57) in (61) to produce

$$\mathrm{Var}\Big\{\hat{\theta}\Big\} \geq \frac{6f_c^2}{\pi^2 S^{\mathrm{d}}(N^2-1)\sin^2(\theta)P_f} \approx \frac{6}{\pi^2 S^{\mathrm{d}}(N^2-1)\sin^2(\theta)} \quad \text{[units: rad}^2\text{]}. \tag{63}$$

Exploitation of the narrowband assumption leads to $P_f/f_c^2 \approx 1$ and the approximation on the right. This result can be shown to be identical to that found in [16, eq. 14] or [14, eq. 17] after transformation to $\theta$ and appropriately accounting for the noise variance and SNR.[13]

# 3 Time-delay-based multiple-pulse estimation of radial velocity

LFM and HFM waveforms are useful in sonar detection because their bandwidth can improve performance in reverberation-limited conditions and their insensitivity to Doppler [5, 6] allows the use of a single matched filter for detection across a large span of radial velocities. The coupling of their ambiguity functions in the delay and Doppler dimensions, however, hinders estimation of these parameters when both are unknown by imparting a bias in delay that depends on the radial velocity. An example of the matched-filter response for an LFM pulse to echoes from OOIs exhibiting different (relative) radial velocities is shown in Fig. 2. When sensing is performed with multiple pulses, one approach to resolving this problem is to use the biased time-delay measurements to jointly estimate the two unknown parameters. The approach is presented and analyzed in this section.

Throughout the pulse train, the OOI is assumed to have constant (but unknown) radial velocity. For non-zero radial velocity, the range of the OOI will be different for pulses projected at different times. This requires choosing a particular reference within the pulse train for which the travel time (i.e., delay) and corresponding OOI range are being estimated. The time and range related to this reference are denoted using a '$\star$' subscript; e.g., $r_\star$ is the OOI range being estimated. It is convenient to interpret these parameters as if they were related to projection of a hypothetical reference pulse. For example, suppose this reference pulse is projected at time $t_\star^{\mathrm{tx}}$, arrives at the OOI at time $t_\star^{\mathrm{ooi}}$ when it is at range $r_\star$, and the echo from the OOI then impinges on the sensor array at time $t_\star$. Although one might expect that placing this reference pulse in the middle of the pulse train can minimize the bounds related to range estimation, this is not the case for waveforms for which time delay and Doppler are coupled. As will be seen in Sect. 4.4, this intuition only holds when the dimensions are uncoupled. For time-delay-based estimation, the choice of $t_\star^{\mathrm{tx}}$ is seen in Sect. 3.4 to affect the CRLB for estimating range and the correlation coefficient between the range and radial velocity estimates.

Given the large number of time-related terms required to describe the pulses and evaluate estimation performance, a list of the definitions is presented in Table 2 (pg. 30).

## 3.1 Geometric modeling for multiple pulses

The time at which the echo from a sonar pulse is observed at a monostatic sonar platform is typically described in terms of the time at which the pulse was transmitted and the range of the

[13] E.g., equating phases using (50) with $\bar{n} = 0$ at center frequency $f_c$ and [14, eq. 3] sampled at $t = nT$, it can be seen that $2\pi f_c \alpha_n(\theta) = \pi n \cos\theta = \omega_0 nT$. Transforming to $\theta$ therefore requires multiplying [14, eq. 17] by $[\partial\theta/\partial\omega_0]^2 = T^2/[\pi^2\sin^2(\theta)]$ and noting that the SNR after processing is $S^{\mathrm{d}} = Nb_0^2/(2\sigma^2)$, which produces (63).

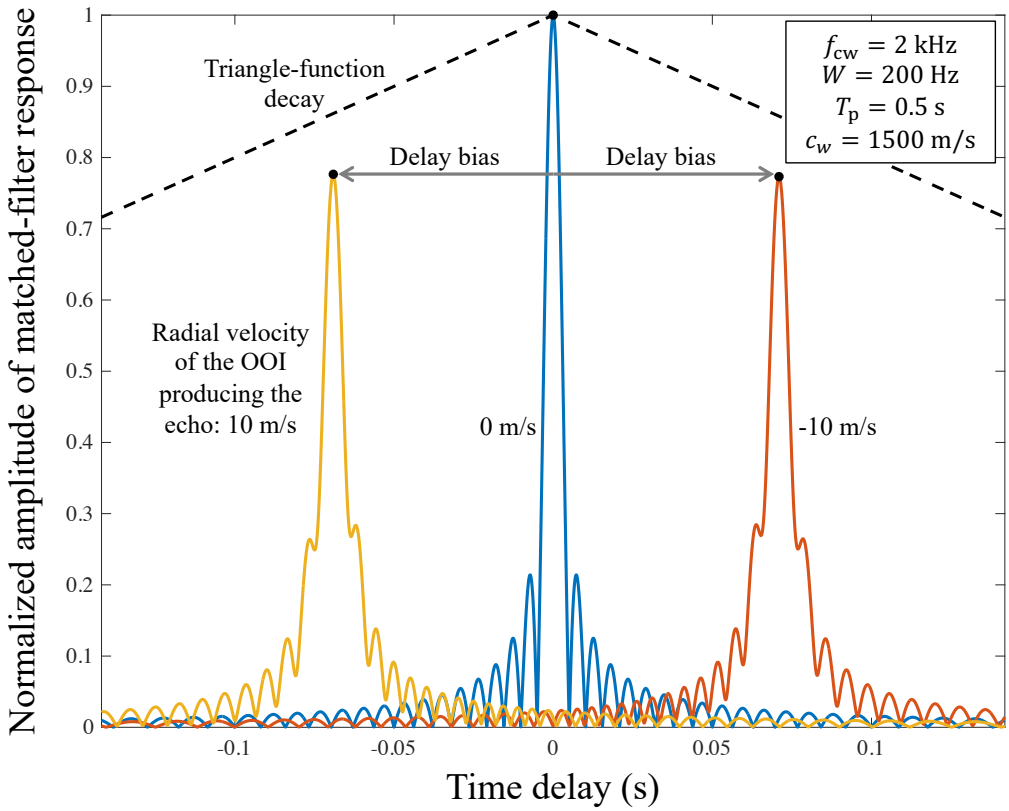


Figure 2: Response of a matched filter using a zero-Doppler replica to echoes from OOIs exhibiting different radial velocities when using an up-sweeping LFM pulse. The delay biases (the black asterisks) are obtained from (81).

OOI when the pulse reflects off of it. Here, however, it must be presented in terms of the relative radial velocity (or Doppler scale), the time at which the echo from a reference pulse is observed, and the delay between projection of the current pulse and the reference pulse. The primary unknown parameters in this scenario are the range of the OOI when it first interacts with the reference pulse (or the equivalent time delay) and the relative radial velocity or Doppler scale. Note that the choice of range or delay and radial velocity or Doppler scale depends on the application—each option has been employed in this report. This purely geometric modeling assumes a constant speed of sound, direct-path propagation, and constant relative radial velocity between the sonar platform and OOI. In contrast to the use of the center of the pulse as a time origin in Sect. 2.3 to define the characteristic time-frequency parameters, here the time at which the $m$th pulse is projected ($t_m^{\text{tx}}$) refers to the onset time of the pulse. This is important because it is how such wavetrains are typically described and it simplifies the analysis when waveforms have different durations.

Consider only the radial dimension between a stationary monostatic sonar platform and an OOI with radial velocity $v$ (where $v > 0\,\text{m/s}$ when the OOI is closing range). If the sonar platform is in motion, let the following analysis be in its coordinate system (so it is always at the origin) and define the radial velocity of the OOI as relative to the sonar platform. Let the hypothetical reference pulse be projected at time $t_\star^{\text{tx}}$ and suppose it reaches the OOI at range $r_\star > 0\,\text{m}$ at time

$$t_\star^{\text{ooi}} = t_\star^{\text{tx}} + \frac{r_\star}{c_w} \quad \text{[units: s]}, \tag{64}$$

Table 2: Definitions of the time-related variables used to describe multiple pulses, all of which have units of seconds. Relevant equations are referenced where appropriate. Note that the hat notation in $\hat{t}_m^{\mathrm{tx}}$, $\hat{\delta}_m$, and $\hat{t}_m$ refers to the middle of the $m$th pulse rather than an estimate of an unknown parameter.

$T_m =$ the duration of the $m$th pulse

$t_m^{\mathrm{tx}} =$ the time at which the $m$th pulse is projected

$t_\star^{\mathrm{tx}} =$ the time at which a hypothetical reference pulse is projected

$t_m^{\mathrm{ooi}} =$ the time at which the $m$th pulse impinges on the OOI (70)

$t_\star^{\mathrm{ooi}} =$ the time at which the reference pulse impinges on the OOI and when the OOI is at range $r_\star$ (64)

$\hat{t}_m^{\mathrm{tx}} = t_m^{\mathrm{tx}} + T_m/2 =$ the time at which the center of the $m$th pulse is projected (114)

$\delta_m = t_m^{\mathrm{tx}} - t_\star^{\mathrm{tx}} =$ the pulse offset time, which is the time delay between projecting the $m$th pulse and the reference pulse (67)

$\hat{\delta}_m = \delta_m + T_m/2 =$ the time delay between the middle of the $m$th pulse and the onset of the reference pulse (115)

$\Delta =$ time between pulses when they are projected at regular intervals

$t_\star =$ the time at which the echo from the reference pulse arrives at the sensor array (65)

$t_m =$ the time at which the echo from the $m$th pulse arrives at the sensor array (74) & (85)

$\hat{t}_m = t_m + T_m/2$ the time at which the echo from the center of the $m$th pulse arrives at the sensor array (A1)

$\tau_\star = t_\star - t_\star^{\mathrm{tx}} = 2r_\star/c_w =$ the time delay observed for the hypothetical reference pulse (111)

$\tau_m = t_m - t_m^{\mathrm{tx}} + \tau_m^{\mathrm{b}} =$ the time delay at which the echo from the $m$th pulse is measured when accounting for any delay biases (87)

$\tau_m^{\mathrm{b}} =$ the delay bias incurred by mismatch in the matched filter (76) & (81) for, respectively, HFM and LFM pulses

$b_m = \tau_m^{\mathrm{b}} c_w/(2v) =$ delay-bias per unit Mach number [units: s], which isolates the effect of the delay bias to waveform characteristics (82)

$d_m = b_m - \delta_m =$ the combination of the two delay terms according to how they impact estimation (91)

$\bar{t}^{\mathrm{tx}} =$ the centroid of the pulse train with respect to time-delay estimation (103)

where $c_w$ [units: m/s] is the speed of sound in water. The echo from this pulse is then observed at the stationary monostatic sonar at time

$$t_\star = t_\star^{\mathrm{tx}} + \frac{2r_\star}{c_w} \quad \text{[units: s]}. \tag{65}$$

The range of the OOI from the sonar platform at time $t$ can be described relative to $r_\star$ as a function of time by

$$r_t = r_\star - v\big(t - t_\star^{\mathrm{ooi}}\big) \quad \text{[units: m]}. \tag{66}$$

In this formulation, a negative range is interpreted as the OOI being on the other side of the sonar platform compared to its position at time $t_\star^{\mathrm{ooi}}$.

Suppose that the $m$th pulse is projected at time

$$t_m^{\mathrm{tx}} = t_\star^{\mathrm{tx}} + \delta_m \quad \text{[units: s]}, \tag{67}$$

where $\delta_m$ [units: s] is the delay between the $m$th pulse and the reference pulse. The wavefront associated with the onset of the $m$th pulse propagates to range

$$r_t = c_w\big[t - (t_\star^{\mathrm{tx}} + \delta_m)\big] \quad \text{[units: m]} \tag{68}$$

for times $t \geq t_\star^{\mathrm{tx}} + \delta_m$. The time at which this wavefront meets the OOI can be obtained by equating (66) and (68) and solving for $t$, which yields

$$t_m^{\mathrm{ooi}} = \frac{1}{c_w + v}\big[r_\star + v t_\star^{\mathrm{ooi}} + c_w\big(t_\star^{\mathrm{tx}} + \delta_m\big)\big] \tag{69}$$

$$= t_\star^{\mathrm{tx}} + \frac{r_\star}{c_w} + \frac{c_w \delta_m}{c_w + v} \quad \text{[units: s]}. \tag{70}$$

The range at which this occurs,

$$r_m = r_\star - \frac{c_w v \delta_m}{c_w + v} \quad \text{[units: m]} \tag{71}$$

can be obtained by using (70) in (66) or (68). The time at which the echo from the $m$th pulse is observed at the sonar platform is then

$$t_m = t_m^{\mathrm{ooi}} + \frac{r_m}{c_w} \tag{72}$$

$$= t_\star + \left(\frac{c_w - v}{c_w + v}\right)\delta_m \tag{73}$$

$$= t_\star + \frac{\delta_m}{\eta} \quad \text{[units: s]} \tag{74}$$

where $\eta$ [unitless] is the Doppler scale in a two-way monostatic geometry. This relationship to $\eta$ is obtained from (3) by noting $v = v_a - v_o$ and letting $v_a = 0\,\mathrm{m/s}$ for the stationary sonar platform. The modifications required to account for how the Doppler scale is related to radial velocity in one-way and bistatic propagation were covered in Sect. 2.4.3.

### 3.2 Modeling the delay measurements after matched filtering

As seen in Fig. 2, the peak response of a matched filter subject to mismatch in Doppler between the echo and the replica occurs at a time offset from the true delay. The origin of this can be seen from the shapes of the LFM and HFM ambiguity functions in Fig. 1, which represent the response of a fixed echo to a Doppler filter bank. The temporal response in the Doppler channel matched to the echo exhibits no bias in the delay measurement—the peak occurs at the origin. However, the mismatched Doppler channels exhibit a bias in delay (i.e., the peak is not at the origin) that depends on radial velocity. From the discussion found on [1, pg. 518], the response of a single matched filter to an echo with different radial velocities is simply a reflection of the ambiguity function in the temporal dimension. This implies that for up-sweeping FM pulses and echoes for which $v > 0\,\mathrm{m/s}$ (closing range), the delay bias in a matched filter using a zero-Doppler replica will be negative. This can also be discerned from the instantaneous frequency of the pulse as follows: (i) echoes from closing objects have an instantaneous frequency that is scaled higher than the zero-Doppler replica; and (ii) for up-sweeping FM pulses, applying a negative delay to the zero-Doppler replica (i.e., shifting it left) aligns the time-frequency content of the echo and replica (to the extent possible). Similar arguments explain the sign of the delay bias for down-sweeping pulses or opening objects.

When a sequence of identical pulses is projected, it is straightforward to estimate the radial velocity from the biased time-delay measurements. However, the time-delay bias must be accounted for when using dissimilar pulses or when an unbiased estimate of the OOI range is desired. Using the narrowband ambiguity function [1, Sect. 8.3.5.2] or converting from the range-based result of [29], the delay bias for an LFM pulse can be approximated by

$$\tau_m^{\mathrm{b}} \approx \frac{\mp T_p f_c}{W} \cdot \frac{2v}{c_w} \quad \text{[units: s]}, \tag{75}$$

where the upper and lower signs in the $\mp$ symbol represent, respectively, up- and down-sweeping waveforms. The delay bias in (75) is indexed by $m$ to account for wavetrains with dissimilar pulses. This form illustrates how the pulse duration, center frequency, bandwidth and the radial velocity affect the delay bias. Although the narrowband approximation in (75) is useful in the performance analyses considered here, it is generally not accurate enough in practice except for very small radial speeds.

Before obtaining a more accurate approximation for the LFM pulse, it is helpful to consider the results presented in [35] for the optimally Doppler tolerant HFM pulse. In [35], the bias was obtained from the delay that best aligns the instantaneous frequencies of a Doppler scaled echo and a zero-Doppler replica. Adapting the result in [35, eq. 26] from range to time delay and accounting for their use of the alternative convention for the sign of relative radial velocity (recall that here $v > 0\,\mathrm{m/s}$ for closing OOIs) results in

$$\tau_m^{\mathrm{b}} = \frac{\mp T_p f_c}{W}\left(1 - \frac{1}{\eta}\right) \quad \text{[units: s]} \tag{76}$$

$$\approx \frac{\mp T_p f_c}{W} \cdot \frac{2v}{c_w} \quad \text{[units: s]} \tag{77}$$

Note that the result in (76) retains the underlying relationship on the Doppler scale $\eta$ [unitless]. When $|v| \ll c_w$, the approximation in (77) is seen to be identical to that for the LFM pulse in (75). As noted above for the LFM pulse, although (77) is accurate enough for the analysis presented here, the more accurate version in (76) should be used in practice.

For an HFM pulse, imparting the delay in (76) causes the instantaneous frequencies to align perfectly over their common frequency band. For LFM pulses, however, matching the instantaneous frequencies of a Doppler scaled echo and a time-shifted zero-Doppler replica is more difficult owing to the change in the sweep rate (i.e., Doppler scaling produces a sweep rate of $\beta_\eta = \eta W/T_p$ [units: Hz/s] that differs from the $\beta = W/T_p$ of the zero-Doppler replica). The approach taken for the LFM pulse is to center the two instantaneous frequencies over their common frequency band. When $\eta > 1$, this causes the instantaneous frequencies to match at

$$f_{\text{mid}} = \frac{\eta f_0 + f_1}{2} = \frac{(\eta+1)f_c}{2} - \frac{(\eta-1)W}{4} \quad \text{[units: Hz]} \tag{78}$$

where $f_0$ and $f_1$ are the low and high frequencies of the zero-Doppler LFM replica. When $\eta < 1$, the sign of the second term changes. The delay required to match the two instantaneous frequencies at $f_{\text{mid}}$ can then be shown to be

$$\tau_m^{\text{b}} = \frac{\mp T_p f_c}{W}\left(1 - \frac{1}{\eta}\right)\left[\frac{\eta + \eta^{-1}}{2} - \frac{W}{4f_c}\left|\eta - \eta^{-1}\right|\right] \quad \text{[units: s]} \tag{79}$$

$$\approx \frac{\mp T_p f_c}{W}\left(1 - \frac{1}{\eta}\right)\left[1 + \frac{2v^2}{c_w^2} - \frac{W}{f_c}\cdot\frac{c_w|v|}{c_w^2 - v^2}\right] \quad \text{[units: s]} \tag{80}$$

$$\approx \frac{\mp T_p f_c}{W}\left(1 - \frac{1}{\eta}\right) \quad \text{[units: s]}. \tag{81}$$

Ignoring the second-order terms produces (81), which is the same result obtained for the HFM pulse in (76).

As noted in (77), the delay bias is approximately proportional to radial velocity. To simplify notation in the analysis presented in the following sections, define the parameter

$$b_m = \frac{\mp T_p f_c}{W} \quad \text{[units: s]} \tag{82}$$

so

$$\tau_m^{\text{b}} = b_m\left(1 - \frac{1}{\eta}\right) \quad \text{[units: s]}. \tag{83}$$

This isolates the waveform-dependent components of the delay bias for the $m$th pulse into the parameter $b_m$.[14] Recalling the approximation from (77), $b_m$ can be interpreted as the delay bias per unit Mach number (i.e., $\tau_m^{\text{b}}$ is approximately $b_m$ multiplied by the effective Mach number for two-way propagation, $v/[c_w/2]$).

Although the approximations in (76) and (81) will often be adequate, it is important to verify their validity by ensuring the errors are small relative to the accuracy of the time-delay measurements (e.g., the square root of the CRLB on time delay when Doppler is known). This is particularly important when using alternative processing such as an extended HFM matched filter [36] or for low time-bandwidth-product pulses where inaccuracies near the edges of the frequency band affect the instantaneous-frequency representation of the pulse. As a final note, when using a Doppler filter bank to estimate time delays (e.g., for a Doppler-sensitive high time-bandwidth-product LFM pulse), the time-delay estimates should be unbiased and the delay-bias multiplier set to zero.

[14] $b_m$ is similar to $\lambda$ in [35, eq. 30].

### 3.3 Least-squared-error estimators of range and radial velocity

The relationships derived in the previous sections provide the means for estimating Doppler scale and OOI range using the arrival times of the echoes from multiple pulses. To accomplish this, the time-delay measurement from the $m$th pulse must be described in terms of the unknown parameters. Using (65) in (73), the arrival time of the $m$th echo is

$$t_m = t_\star^{\text{tx}} + \frac{2r_\star}{c_w} + \frac{\delta_m}{\eta} \tag{84}$$

$$= t_m^{\text{tx}} + \frac{2r_\star}{c_w} - \left(1 - \frac{1}{\eta}\right)\delta_m \quad \text{[units: s]}, \tag{85}$$

where (85) is obtained by noting that $t_\star^{\text{tx}} = t_m^{\text{tx}} - \delta_m$ from (67).

The time delay between transmission of the $m$th pulse and when its echo is measured at the sonar, accounting for the bias in delay induced by use of a zero-Doppler matched filter, is then

$$\tau_m = t_m - t_m^{\text{tx}} + \tau_m^{\text{b}} \tag{86}$$

$$= \frac{2r_\star}{c_w} + (b_m - \delta_m)\left(1 - \frac{1}{\eta}\right) \quad \text{[units: s]}. \tag{87}$$

To simplify the analysis, define the approximate radial velocity parameter to be estimated as

$$v_\star = \frac{c_w}{2}\left(1 - \frac{1}{\eta}\right) = \frac{v}{1 + v/c_w} \quad \text{[units: m/s]}. \tag{88}$$

When the radial speed is small relative to the speed of sound ($|v| \ll c_w$), then $v_\star$ is an accurate surrogate for radial velocity. When it is not, an estimate of the radial velocity can be obtained from the inverse relationship,

$$v = \frac{v_\star}{1 - v_\star/c_w} \quad \text{[units: m/s]}. \tag{89}$$

With $v_\star$ representing radial velocity, the time-delay measurements can be written as linear functions of the unknown parameters,

$$\tau_m = \frac{2}{c_w}[r_\star + (b_m - \delta_m)\, v_\star] \quad \text{[units: s]}. \tag{90}$$

This simplifies estimation of $r_\star$ and $v_\star$ from the time delays measured over multiple pulses through the application of standard linear models (e.g., estimating the parameter vector $\mathbf{x}$ when noise-free measurements have the form $\mathbf{y} = \mathbf{A}\mathbf{x}$). Placing the measurement times in the vector $\boldsymbol{\tau} = [\tau_1\ \tau_2\ \cdots\ \tau_M]^T$, the pulse offset times in the vector $\boldsymbol{\delta} = [\delta_1\ \delta_2\ \cdots\ \delta_M]^T$, the delay-bias multipliers in the vector $\mathbf{b} = [b_1\ b_2\ \cdots\ b_M]^T$, and defining the vector of ones $\mathbf{1} = [1\ 1\ \cdots\ 1]^T$, the linear model across $M$ pulses can be written as

$$\boldsymbol{\tau} = \frac{2}{c_w}\begin{bmatrix}\mathbf{1} & \mathbf{d}\end{bmatrix}\begin{bmatrix} r_\star \\ v_\star \end{bmatrix} \quad \text{[units: s]}, \tag{91}$$

where $\mathbf{d} = \mathbf{b} - \boldsymbol{\delta}$ combines the two delay terms and has $d_m = b_m - \delta_m$ [units: s] as its $m$th element. In order to estimate the unknown parameters, there must be at least two measurements and the columns of the model matrix $\mathbf{A} = (2/c_w)[\mathbf{1}\ \mathbf{d}]$ must be linearly independent. For example, if

identical pulses are projected (i.e., all pulses have the same delay-bias multiplier), they cannot all be projected simultaneously. Conversely, simultaneously projected pulses must have some diversity in their delay-bias multipliers.

In practice, the time-delay measurements have errors. To represent this, let the estimates of the time delays be

$$\hat{\boldsymbol{\tau}} = \boldsymbol{\tau} + \mathbf{e}, \tag{92}$$

where $\mathbf{e}$ is a vector of errors. The approach taken to estimate the unknown parameters depends on the statistical characterization of $\mathbf{e}$. If the pulses are orthogonal (e.g., disjoint in either their temporal or spectral support), as is assumed here, the measurement errors will be uncorrelated. The errors will typically have zero mean because the delay biases are already included in (91). However, their variances can differ when different pulses are used or when conditions change between pulses and SNR is affected. This can be accounted for by defining the covariance matrix of $\mathbf{e}$ as being diagonal, $\boldsymbol{\Lambda} = \mathrm{E}[\mathbf{e}\mathbf{e}^T] = \mathrm{diag}\{\lambda_1, \ldots, \lambda_M\}$, where $\lambda_m$ [units: s$^2$] is the variance of $\hat{\tau}_m$, the $m$th time-delay measurement. The off-diagonal terms are zero because the noise is uncorrelated. Given the diagonal form of $\boldsymbol{\Lambda}$, the parameters can be estimated using a weighted least-squared-error (LSE) approach. Following the discussion in the penultimate paragraph of Sect. 2.4.2, it is reasonable to assume the errors are Gaussian distributed when the SNR is high, in which case the maximum likelihood estimate is the same as a weighted LSE solution.

The weighted LSE solution to a set of linear equations is found by whitening both sides of (91) (e.g., by pre-multiplying by $\boldsymbol{\Lambda}^{-1/2}$) followed by pre-multiplying both sides by the pseudo-inverse of the whitened model matrix (i.e., pre-multiply by $\left(\boldsymbol{\Lambda}^{-1/2}\mathbf{A}\right)^+ = (\mathbf{A}^T\boldsymbol{\Lambda}^{-1}\mathbf{A})^{-1}\mathbf{A}^T\boldsymbol{\Lambda}^{-1/2}$). This results in

$$\hat{v}_\star = \frac{c_w}{2M\sigma_d^2}\left(\mathbf{d} - \bar{d}\mathbf{1}\right)^T \mathbf{W}\hat{\boldsymbol{\tau}} \quad \text{[units: m/s]} \tag{93}$$

as an estimate of the radial velocity and

$$\hat{r}_\star = \frac{c_w}{2M\sigma_d^2}\left[\left(\sigma_d^2 + \bar{d}^2\right)\mathbf{1} - \bar{d}\,\mathbf{d}\right]^T \mathbf{W}\hat{\boldsymbol{\tau}} \quad \text{[units: m]} \tag{94}$$

for the estimate of the OOI range when it first interacts with the reference pulse. The diagonal matrix $\mathbf{W} = M\boldsymbol{\Lambda}^{-1}/(\mathbf{1}^T\boldsymbol{\Lambda}^{-1}\mathbf{1})$ has as its $m$th element

$$w_m = \frac{\lambda_m^{-1}}{\frac{1}{M}\sum_{m=1}^{M}\lambda_m^{-1}} = \frac{\check{\lambda}}{\lambda_m} \quad \text{[unitless]}, \tag{95}$$

where

$$\check{\lambda} = \frac{1}{\frac{1}{M}\sum_{m=1}^{M}\frac{1}{\lambda_m}} \quad \text{[units: s}^2\text{]} \tag{96}$$

is the harmonic mean of the measurement variances. This weighting matrix acts to emphasize measurements with lower variances and limit the contributions of those with higher ones. If the measurements have the same variance, then $\mathbf{W}$ simplifies to an identity matrix. The terms

$$\bar{d} = \frac{\mathbf{1}^T\mathbf{W}\mathbf{d}}{M} = \frac{1}{M}\sum_{m=1}^{M} w_m d_m \quad \text{[units: s]} \tag{97}$$

and

$$\sigma_d^2 = \frac{\mathbf{d}^T\mathbf{W}\mathbf{d}}{M} - \bar{d}^2 = \frac{1}{M}\sum_{m=1}^{M} w_m(d_m - \bar{d})^2 \quad \text{[units: s}^2\text{]} \tag{98}$$

are, respectively, the weighted average and variance of the combined pulse-offset-time and delay-bias terms.

Before evaluating the performance of these estimators, note that $\bar{d}$ and $\sigma_d^2$ can be decomposed into similar components over the pulse offset times ($\bar{\delta}$ & $\sigma_\delta^2$) and delay-bias multipliers ($\bar{b}$ & $\sigma_b^2$):

$$\bar{d} = \bar{b} - \bar{\delta} \quad \text{[units: s]} \tag{99}$$

and

$$\sigma_d^2 = \sigma_b^2 + \sigma_\delta^2 - 2\rho_{b\delta}\sigma_b\sigma_\delta \quad \text{[units: s}^2\text{]}, \tag{100}$$

where

$$\rho_{b\delta} = \frac{1}{M\sigma_b\sigma_\delta}\sum_{m=1}^{M} w_m(b_m - \bar{b})(\delta_m - \bar{\delta}) \quad \text{[unitless]} \tag{101}$$

is a weighted sample correlation coefficient between the two.

The average over the delays $\delta_1, \ldots, \delta_M$ can also be related to the time at which the hypothetical reference pulse occurs within the pulse train according to

$$\bar{\delta} = \bar{t}^{\,\mathrm{tx}} - t_\star^{\mathrm{tx}} \quad \text{[units: s]}, \tag{102}$$

where

$$\bar{t}^{\,\mathrm{tx}} = \frac{1}{M}\sum_{m=1}^{M} w_m t_m^{\mathrm{tx}} \quad \text{[units: s]} \tag{103}$$

is the centroid of the pulse train with respect to time-delay estimation (i.e., it weights the pulse onset times according to their time-delay estimation performance).

### 3.4 Performance bounds

By including the delay biases in the modeling, the delay estimates (for $\tau_m$) are unbiased. Coupling this with the linearity of the weighted LSE estimates implies $\hat{v}_\star$ and $\hat{r}_\star$ are also unbiased. The variances of the two estimators,

$$\mathrm{Var}\{\hat{v}_\star\} = \frac{c_w^2\check{\lambda}}{4M\sigma_d^2} \quad \text{[units: m}^2\text{/s}^2\text{]} \tag{104}$$

and

$$\mathrm{Var}\{\hat{r}_\star\} = \frac{c_w^2\check{\lambda}}{4M}\left(1 + \frac{\bar{d}^2}{\sigma_d^2}\right) \quad \text{[units: m}^2\text{]}, \tag{105}$$

can also be easily obtained owing to the linear relationships. As might be expected, these results imply performance improves as the number of pulses increases ($M \uparrow$), as the underlying delay estimates improve ($\check{\lambda} \downarrow$), or when the spread of the combined delay terms increases ($\sigma_d \uparrow$). Evaluation of (104) and (105) requires knowledge of the variance of the time-delay measurements. This is typically obtained through the use of CRLBs formed when Doppler is assumed to be known (e.g., from Sect. 2.4.1), despite the apparent contradiction. Although it is often small, the loss arising from mismatch in Doppler between the echo and matched-filter replica should be included as a reduction in SNR, which will act to increase $\check{\lambda}$.

It is clear from the result in (105) that estimation of range depends on when the hypothetical reference pulse is projected. Noting from (99) and (102) that $\bar{d} = \bar{b} - \left(\bar{t}^{\,\mathrm{tx}} - t_\star^{\mathrm{tx}}\right)$, it is tempting to set $t_\star^{\mathrm{tx}} = \bar{t}^{\,\mathrm{tx}} - \bar{b}$ so $\bar{d} = 0\,\mathrm{s}$. When this can be managed, the range estimate achieves its lowest variance and is a factor of $M$ smaller than that for a single pulse having time-delay variance equal to the harmonic average over all the pulses. However, recalling that the delay-bias multiplier for an LFM pulse is $b_m = \mp T_p f_c / W$, it is clear that this could place the reference pulse outside of the wavetrain. When other factors do not dictate how to choose $t_\star^{\mathrm{tx}}$, it will be set to the centroid, $t_\star^{\mathrm{tx}} = \bar{t}^{\,\mathrm{tx}}$, even though it leads to a higher variance in the range estimate.

Examining (104), the inverse dependence on $M$ can also be seen for the variance of the radial velocity estimate. However, the spread of the delay terms (i.e., $\sigma_d^2$) can play an important role either when similar pulses have large delays between them or when simultaneous or closely spaced pulses have diversity in their delay-bias multipliers. As an example of the latter scenario, recall that up- and down-sweeping LFM or HFM pulses have delay-bias multipliers with opposing signs. If the delay-bias multipliers are negatively correlated with the pulse offset times, then (100) dictates that $\sigma_d^2$ will be larger than if they are positively correlated. As will be seen in Sect. 5.4, this leads to better performance for a down-up LFM pulse pair than for an up-down pair.

The correlation coefficient between the range and radial velocity estimates can be shown to equal

$$\text{Corr. Coeff.}\{\hat{r}_\star, \hat{v}\} = \frac{-\bar{d}}{\sqrt{\sigma_d^2 + \bar{d}^2}} \quad \text{[unitless]}. \tag{106}$$

Similar to the variance on the range estimate, designing the pulses so $|\bar{d}|$ is small has the advantage of reducing the correlation between the range and radial velocity estimates.

### 3.4.1 Radial-velocity estimation with a uniform pulse train

When a sequence of identical pulses is projected and their echoes have the same SNR, the variances of the time-delay measurement errors and the delay biases are constant. The latter results in $\sigma_d^2 = \sigma_\delta^2$ because $\sigma_b^2 = 0\,\mathrm{s}^2$. This simplifies the variance in (104) of the radial-velocity estimate to

$$\mathrm{Var}\{\hat{v}_\star\} = \frac{c_w^2 \sigma_\tau^2}{4 M \sigma_\delta^2} \quad \text{[units: } \mathrm{m}^2/\mathrm{s}^2\text{]}, \tag{107}$$

where $\check{\lambda} = \sigma_\tau^2$ is the variance of one time-delay measurement.

From [1, eq. 8.270] or from the discussion following (31), the CRLB for unbiased estimation of time delay when Doppler is known with a frequency-modulated waveform and a deterministic

signal model implies

$$\sigma_\tau^2 \geq \frac{1}{8\pi^2 S^{\mathrm{d}} \sigma_f^2} \quad \text{[units: s}^2\text{]}, \tag{108}$$

where $S^{\mathrm{d}}$ is the SNR after coherent detection processing of a single pulse and $\sigma_f^2$ characterizes the frequency variation over time. For example, $\sigma_f^2 = W^2/12$ for an LFM waveform with bandwidth $W$ and for HFM waveforms when $W/f_c$ is not too large. Using this in (107) produces

$$\mathrm{Var}\{\hat{v}\} \geq \frac{c_w^2}{32\pi^2 M S^{\mathrm{d}} \sigma_\delta^2 \sigma_f^2} = \frac{3c_w^2}{8\pi^2 M S^{\mathrm{d}} W^2 \sigma_\delta^2} \quad \text{[units: m}^2\text{/s}^2\text{]} \tag{109}$$

as a lower bound on the variance of multiple-pulse radial-velocity estimation when using the basic FM pulses. Although this does not necessarily achieve the inverse dependence on center frequency of the CW pulse (e.g., see (32)), it can be significantly better than a single LFM pulse when the pulses are spread over a long period of time. For example, if the pulses are projected with a constant repetition interval of $\Delta$ [units: s], the variance

$$\sigma_\delta^2 = \frac{\Delta^2 (M^2 - 1)}{12}, \quad \text{[units: s}^2\text{]} \tag{110}$$

which is approximately proportional to the square of the total temporal span of the pulse train. In Sect. 5.2.3, the result in (109) is seen to be very similar to the CRLB for incoherent echoes developed in Sect. 4.3 (in fact it is identical for HFM pulses). This implies the time-delay-based estimator of radial velocity will be efficient if the individual-pulse time-delay estimates are efficient (e.g., as occurs when SNR is high enough).

# 4 Cramér-Rao lower bounds when estimation employs multiple orthogonal pulses

Coherent detection processing in active sonar entails matched filtering the measured data, where the replica used in the matched filter is constructed from the projected pulse and based on an assumed Doppler scaling. When an active sonar projects multiple pulses in a wavetrain, the processing approach depends on the assumptions made regarding the bulk phase observed in the echoes from each pulse (e.g., $\psi$ in (1) for a single pulse). If the bulk phase is expected to change from one pulse's echo to the next in an unknown manner, the inter-pulse processing is described as incoherent.[15] However, if the bulk phase is constant across all of the echoes, the standard matched filtering is applied with the sequence of pulses treated as a single continuous waveform. These two scenarios will be referred to as having incoherent or coherent echoes. The terms comprising the Fisher information matrix (FIM) and Cramér-Rao lower bound are developed in this section when estimating radial velocity and time delay from multiple pulses under these two coherency assumptions.

Determining which phase condition applies requires considering how the sensing geometry and propagation change from when one pulse is projected to the next (e.g., see [1, Sect. 7.2.3.1]). When multiple pulses are projected in rapid succession, it is reasonable to assume their echoes will have

[15] For example, extending the derivation of the matched filter as a generalized likelihood ratio detector in [1, Sect. 8.2.3] to account for multiple orthogonal pulses with different unknown bulk-phase terms would result in a sum of the squared moduli of the single-pulse matched-filter responses. This discards the phase after single-pulse matched filtering and is therefore considered incoherent multiple-pulse processing.

the same bulk phase—if they do not, then the echo from a single pulse is not likely to follow the model in (1). However, this may not always be the case, as it is possible for pulses at different frequencies to be subject to different propagation effects. At the other extreme, when pulses are separated by large gaps of time (e.g., across multiple pings), the bulk phases of their echoes are most likely different.

In contrast to the development in Sect. 3 where the range ($r_\star$) of the OOI was estimated, the CRLBs derived in this report are based around estimating the time delay

$$\tau_\star = \frac{2r_\star}{c_w} \quad \text{[units: s]} \tag{111}$$

associated with the reference pulse for a two-way monostatic sensing geometry. The tools required to evaluate the multiple-pulse CRLBs for coherent and incoherent echoes are presented in Sects. 4.2 & 4.3, respectively. Restricting consideration to orthogonal pulses allows formulating the results as a combination of the individual-pulse characteristic time-frequency parameters.

For coherent echoes, this is a straightforward extension of the characteristic time-frequency parameters as they were defined in (11)–(13). The timing of the pulses is seen in Sect. 4.2 to affect the Doppler-scale-related terms; a derivation of the results can be found in App. A.1. The analysis for incoherent echoes is more complicated. It requires allowing the echo from each pulse to have a different bulk phase, which increases the dimension of the FIM to $M+2$ when there are $M$ pulses. The CRLBs are formed from the diagonal elements associated with the delay and Doppler scale parameters found in the inverse of the FIM formed over all $M+2$ unknown and coupled parameters. Although the general form of the pertinent partition of the inverse FIM is presented in Sect. 4.3, its derivation is relegated to App. A.2.

The bounds formed using the FIM terms shown in Sects. 4.2 and 4.3 are applied in Sect. 5 to several examples, in most cases aiming to obtain significant improvements in multiple-pulse estimation of radial velocity when time delay is unknown.

### 4.1 Characterizing the pulses

To support the following discussion, the reader is referred to Table 2 (pg. 30) for definitions of the temporal parameters related to the projected pulses and their echoes, which are the same as those used in Sect. 3. Suppose the $m$th pulse has duration $T_m$ [units: s] and an instantaneous frequency $f_m(t)$ [units: Hz] described for the interval $t \in (-T_m/2, T_m/2)$, so the center of the pulse is its time origin. Because this is the same time origin used in Sect. 2.3, the characteristic time-frequency parameters of the basic sonar pulses found in Table 1 (pg. 16) can be applied here to evaluate multiple pulses. They are identified by using the subscript $m$; for example, the average time (in units of periods) for the $m$th pulse is simply

$$\bar{c}_m = \frac{1}{T_m} \int_{-T_m/2}^{T_m/2} t f_m(t)\, \mathrm{d}t \quad \text{[unitless]} \tag{112}$$

from (12).

As shown in App. A, the FIM terms for multiple pulses can be described by straightforward combinations of the individual-pulse

- characteristic time-frequency parameters ($\bar{f}_m$, $P_{f_m}$, $\bar{c}_m$, $P_{c_m}$, and $\bar{r}_m$),
- SNR ($S_m^{\mathrm{d}}$), and
- time difference ($\hat{\delta}_m$) between the individual-pulse center and the onset of the reference pulse,

for $m = 1, \ldots, M$.

Especially when pulse trains employ different pulse types or when there are large time gaps between pulses, the individual-pulse SNRs can be expected to differ. Define the total linear-quantity SNR across the $M$ pulses as

$$S_{\mathrm{tot}}^{\mathrm{d}} = \sum_{m=1}^{M} S_m^{\mathrm{d}} \quad \text{[unitless]}, \tag{113}$$

where $S_m^{\mathrm{d}}$ is the SNR of the $m$th pulse. The individual-pulse SNRs weight their respective contributions to the FIM and the total SNR in (113) facilitates characterizing the multiple-pulse CRLBs for coherent echoes in a similar form to the single-pulse results found in (29)–(31).

When projecting multiple pulses, it is common to characterize them by the times at which they are projected (e.g., $t_m^{\mathrm{tx}}$ [units: s] as the onset time of the $m$th pulse). Exploiting the characteristic time-frequency parameters from Sect. 2.3 requires defining the time at which the center of the $m$th pulse is projected. It is simply the onset time plus half the pulse width,

$$\hat{t}_m^{\mathrm{tx}} = t_m^{\mathrm{tx}} + \frac{T_m}{2} = t_\star^{\mathrm{tx}} + \delta_m + \frac{T_m}{2} = t_\star^{\mathrm{tx}} + \hat{\delta}_m. \quad \text{[units: s]} \tag{114}$$

As will be seen, it is convenient to use (67) to incorporate the onset time of the reference pulse ($t_\star^{\mathrm{tx}}$ [units: s]) into (114) and define

$$\hat{\delta}_m = \delta_m + \frac{T_m}{2} = t_m^{\mathrm{tx}} - t_\star^{\mathrm{tx}} + \frac{T_m}{2} \tag{115}$$

as the time difference between the center of the $m$th pulse and the onset of the reference pulse.

## 4.2 Bounds for coherent echoes

When the bulk phase across a set of echoes is constant, they can be processed coherently so each echo contributes information to the phase estimate. This generally occurs by implementing a Doppler filter bank using replicas constructed from the full set of pulses. It is important that the replicas are formed correctly accounting for the effect of radial motion on the inter-pulse transmission delays as described in Sect. 3.1. Although the pulses might span a significant period of time, the model from (1) is still assumed to hold, so the echo from the OOI has the form $Ae^{j\psi}\mathring{s}(\eta[t - \tau_\star])$, where $\mathring{s}(t)$ is the analytic signal of the multiple-pulse waveform and the time delay of interest is $\tau_\star$ from (111).

Using the definitions in (11)–(13), it is straightforward to show (see App. A.1) that the multiple-

pulse characteristic time-frequency parameters are

$$\bar{f} = \frac{1}{S^{\mathrm{d}}_{\mathrm{tot}}} \sum_{m=1}^{M} S^{\mathrm{d}}_m \bar{f}_m \quad \text{[units: Hz]}, \tag{116}$$

$$P_f = \frac{1}{S^{\mathrm{d}}_{\mathrm{tot}}} \sum_{m=1}^{M} S^{\mathrm{d}}_m P_{f_m} \quad \text{[units: Hz}^2\text{]}, \tag{117}$$

$$\bar{c} = \frac{1}{S^{\mathrm{d}}_{\mathrm{tot}}} \sum_{m=1}^{M} S^{\mathrm{d}}_m \left( \bar{c}_m + \hat{\delta}_m \bar{f}_m \right) \quad \text{[unitless]}, \tag{118}$$

$$P_c = \frac{1}{S^{\mathrm{d}}_{\mathrm{tot}}} \sum_{m=1}^{M} S^{\mathrm{d}}_m \left( P_{c_m} + 2\hat{\delta}_m \bar{r}_m + \hat{\delta}^2_m P_{f_m} \right) \quad \text{[unitless]}, \text{ and} \tag{119}$$

$$\bar{r} = \frac{1}{S^{\mathrm{d}}_{\mathrm{tot}}} \sum_{m=1}^{M} S^{\mathrm{d}}_m \left( \bar{r}_m + \hat{\delta}_m P_{f_m} \right) \quad \text{[units: Hz]} \tag{120}$$

where $\hat{\delta}_m = \delta_m + T_m/2$ represents the time difference between the center of the $m$th pulse and the onset of the reference pulse.

These can be used in (14)–(16) to obtain $\sigma^2_f$, $\sigma^2_c$, and $\rho$, which then allow forming the CRLBs in (29)–(31) to represent the limits of unbiased coherent multiple-pulse joint estimation of the parameters after replacing $S^{\mathrm{d}}$ with the total SNR from (113).

### 4.3 Bounds for incoherent echoes

When the bulk phase of the echo from one pulse is expected to differ from the others, the number of unknown, coupled parameters in the estimation problem increases to $M + 2$ to account for the $M$ bulk phase terms, which are denoted by the vector $\boldsymbol{\psi} = [\psi_1 \cdots \psi_M]^T$. Fortunately, the structure of the matrix allows a simple characterization of the 2-by-2 partition of the inverse FIM associated with the time delay ($\tau_\star$) and Doppler scale ($\eta$) parameters. As shown in (A33) from App. A.2, this results in

$$\left\{ \mathrm{FIM}^{-1}(\tau_\star, \eta, \boldsymbol{\psi}) \right\}_{\tau_\star, \eta} = \frac{1}{8\pi^2} \left\{ \sum_{m=1}^{M} S^{\mathrm{d}}_m \begin{bmatrix} \sigma^2_{f_m} & -\sigma_{f_m}\sigma_{c_m}\rho_m - \hat{\delta}_m \sigma^2_{f_m} \\ -\sigma_{f_m}\sigma_{c_m}\rho_m - \hat{\delta}_m \sigma^2_{f_m} & \sigma^2_{c_m} + 2\hat{\delta}_m \rho_m \sigma_{f_m}\sigma_{c_m} + \hat{\delta}^2_m \sigma^2_{f_m} \end{bmatrix} \right\}^{-1}. \tag{121}$$

The CRLBs for time-delay and Doppler scale are obtained from, respectively, the first and second diagonal elements of (121). As previously described, the bounds for range and radial velocity are then obtained after multiplying by $c^2_w/4$. As will be seen in the examples in Sect. 5, this form often simplifies to the point where the inverse of the 2-by-2 matrix in (121) can be obtained analytically.[16] However, it is quite simple to evaluate computationally in the general case.

[16] Recall from linear algebra that the inverse of a 2-by-2 matrix is

$$\begin{bmatrix} a & b \\ c & d \end{bmatrix}^{-1} = \frac{1}{ad - bc} \begin{bmatrix} d & -b \\ -c & a \end{bmatrix}. \tag{122}$$

### 4.4 Effect of changing the time of the reference pulse

In the CRLB analysis presented in this report, the time delay being estimated is that associated with a (hypothetical) reference pulse having onset time $t_\star^{\text{tx}}$ [units: s]. In Sect. 2.3, this was set to the center of the projected pulse, which produces symmetry for LFM pulses and simplifies the analysis over multiple pulses. However, the manner in which $t_\star^{\text{tx}}$ is set typically depends on the application. The results presented in Sect. 4.2 for multiple coherent echoes provide the tools required to assess how changing $t_\star^{\text{tx}}$ alters the CRLBs.

For a single pulse, the time delay between the middle of the pulse and the onset time of the reference pulse is $\hat{\delta} = t^{\text{tx}} + \frac{T_p}{2} - t_\star^{\text{tx}}$ from (115), where $T_p$ [units: s] is the duration and $t^{\text{tx}}$ [units: s] is the onset time of the one projected pulse considered here. Setting $t_\star^{\text{tx}}$ to the center of the pulse results in $\hat{\delta} = 0\,\text{s}$. Setting $M = 1$ in (116)–(120) produces the characteristic time-frequency parameters for a shifted time origin,

$$\bar{c}_\delta = \bar{c} + \hat{\delta}\bar{f} \quad \text{[unitless]}, \tag{123}$$

$$P_{c_\delta} = P_c + 2\hat{\delta}\bar{r} + \hat{\delta}^2 P_f \quad \text{[unitless], and} \tag{124}$$

$$\bar{r}_\delta = \bar{r} + \hat{\delta}P_f \quad \text{[units: Hz]}, \tag{125}$$

where the subscript $\delta$ implies $\hat{\delta} \neq 0\,\text{s}$. The parameters without a direct time dependence (i.e., $\bar{f}$, $P_f$ and $\sigma_f^2$) do not depend on $\hat{\delta}$ and therefore do not change when the time origin shifts. The other parameters, however, have the form

$$\sigma_{c_\delta}^2 = \sigma_c^2 + 2\hat{\delta}\rho\sigma_c\sigma_f + \hat{\delta}^2\sigma_f^2 \quad \text{[unitless]} \tag{126}$$

and

$$\rho_\delta = \frac{\rho\sigma_c + \hat{\delta}\sigma_f}{\sigma_{c_\delta}} = \frac{\rho\sigma_c + \hat{\delta}\sigma_f}{\sqrt{\sigma_c^2 + 2\hat{\delta}\rho\sigma_c\sigma_f + \hat{\delta}^2\sigma_f^2}} \quad \text{[unitless]}. \tag{127}$$

Setting $\hat{\delta} = 0\,\text{s}$ clearly simplifies (126) and (127) to their original characteristic time-frequency parameters, for which the time origin is the center of the pulse.

The sub-matrix of the inverse FIM for $\tau$ and $\eta$ from (28) is then seen to be

$$\left\{\text{FIM}^{-1}(\tau,\eta,\psi)\right\}_{\tau,\eta} = \frac{\begin{bmatrix} \sigma_c^2 + 2\hat{\delta}\rho\sigma_c\sigma_f + \hat{\delta}^2\sigma_f^2 & \rho\sigma_c\sigma_f + \hat{\delta}\sigma_f^2 \\ \rho\sigma_c\sigma_f + \hat{\delta}\sigma_f^2 & \sigma_f^2 \end{bmatrix}}{8\pi^2 S^{\text{d}}\sigma_f^2\sigma_c^2(1-\rho^2)}. \tag{128}$$

As expected, setting $\hat{\delta}$ to zero yields (28) and it can be seen that changes to $t_\star^{\text{tx}}$ do not affect estimation of Doppler, only time delay and the correlation between the estimates. If a waveform does not have time-frequency coupling when the origin is the center of the pulse (i.e., $\rho = 0$), it can be seen that the correlation is proportional to $\hat{\delta}$ (and therefore depends on $t_\star^{\text{tx}}$) and that the CRLB for estimation of time delay (or range) is minimized at the middle of the pulse (i.e., when $\hat{\delta} = 0\,\text{s}$).

To build intuition on how changing the reference-pulse time affects time-delay estimation performance for waveforms with coupling between time delay and Doppler, consider the onset of the projected pulse, for which $t_\star^{\text{tx}} = t^{\text{tx}}$ and $\hat{\delta} = T_p/2$. Using this in (123)–(127) for an LFM pulse

will produce the results presented in [1, Sect. 8.5]. More importantly, because $\hat{\delta}$ is positive, using a waveform with a negative value of $\rho$ (e.g., a down-sweeping LFM or HFM) will provide better estimation of the OOI range when the projected pulse first interacts with it than one for which $\rho > 0$. Conversely, when the time delay associated with the end of the pulse is of interest, $t_\star^{\text{tx}} = t^{\text{tx}} + T_p$, $\hat{\delta} = -T_p/2$ and a pulse for which $\rho > 0$ would be desirable (e.g., an up-sweeping LFM or HFM). An intuitive explanation for this effect is that time-delay estimation is best when the onset time of the reference pulse aligns with the highest frequencies in a waveform as they are the most sensitive to Doppler. An extension of this to the case of predicting the range of an OOI with a uniform pulse train is examined in Sect. 5.2.6 to corroborate the recommended use [11, 29] of up-sweeping FM pulses in tracking rather than down-sweeping ones.

# 5 Examples

Several examples are presented in this section, exploring different approaches to estimating radial velocity and time delay using multiple pulses. In Sect. 5.1, it is seen how combining concurrently projected CW pulses can improve time-delay estimation, which is a weakness of individual CW pulses that are not short in duration. Generic results for a uniform pulse train are presented in Sect. 5.2, with LFM and PLFM examples and an explanation for why up-sweeping FM pulses are better for predicting range than down-sweeping ones (Sect. 5.2.6). Dividing an LFM pulse up into constituent sub-pulses is examined in Sect. 5.3, where the potential gain is seen to depend on bandwidth-dependent spreading losses. Various combinations of up- and down-sweeping LFM pulses are shown to provide significant improvement to radial-velocity estimation in Sect. 5.4 and illustrate the unexpected result that a down-up LFM pulse pair is better than an up-down one. Finally, the common practice of projecting CW- and FM-pulse pairs is examined in Sect. 5.5 and reveals the expected potential for improvements to un-biased time-delay estimation.

Throughout these examples it is seen that combining multiple pulses can lead to outsize improvements (i.e., more reduction than accounted for by the $M$-fold increase in total SNR) to estimation performance when there is diversity across the pulses. As might be expected for waveforms of the same type, spectral diversity improves time-delay estimation and temporal diversity aids estimation of radial velocity. Similar improvement can also be obtained by combining different types of pulses, if they have the right type of diversity (e.g., combining up- and down-sweeping FM pulses).

When possible, the essential results of the examples are presented and discussed at the beginning of each section, delaying the supporting material and derivations in order to make the analysis more accessible. Finally, it should be noted that the focus of these examples is solely on estimation of time delay and/or radial velocity. Many of the waveform combinations have disadvantages limiting their utility in certain applications that are not discussed in any detail.

## 5.1 CW comb waveform

A disadvantage of CW pulses is their poor resolution in time (equivalently range), as was seen in Sect. 2.4.1, and their susceptibility to reverberation when the OOI has low Doppler. An alternative can be found in *comb* waveforms [37, 38] formed by simultaneously projecting multiple CW pulses. Although both coherent and incoherent processing approaches exist [37], the focus in this analysis is on the former.

Suppose a comb waveform has duration $T_p$ [units: s] and comprises $M$ equal-amplitude CW

pulses with the $m$th at frequency $f_m$ [units: Hz]. From the entries in the CW-pulse column in Table 1 (pg. 16), the characteristic time-frequency parameters for the $m$th pulse are

$$\bar{f}_m = f_m \quad \text{[units: Hz]}, \tag{129}$$

$$\sigma^2_{f_m} = 0, \text{ which leads to } P_{f_m} = f_m^2 \quad \text{[units: Hz}^2\text{]}, \tag{130}$$

$$\bar{c}_m = \frac{T_p f_m}{2} \quad \text{[unitless]}, \tag{131}$$

$$\sigma^2_{c_m} = \frac{T_p^2 f_m^2}{12} \quad \text{[unitless], which leads to } P_{c_m} = \frac{T_p^2 f_m^2}{3} \quad \text{[unitless], and} \tag{132}$$

$$\rho_m = 0 \quad \text{[unitless], which leads to } \bar{r}_m = \frac{T_p f_m^2}{2} \quad \text{[units: Hz]}. \tag{133}$$

Letting $\hat{\delta}_m = 0\,\text{s}$ sets the reference time to the center of the pulse. Using these to obtain the multiple-pulse parameters in Sect. 4.2 under the assumption of a constant SNR (i.e., $S^{\text{d}}_m = S^{\text{d}}_{\text{tot}}/M$) leads to

$$\bar{f} = \frac{1}{M}\sum_{m=1}^{M} f_m \quad \text{[units: Hz]}, \tag{134}$$

$$\sigma_f^2 = \frac{1}{M}\sum_{m=1}^{M} (f_m - \bar{f})^2 \quad \text{[units: Hz}^2\text{]}, \tag{135}$$

$$\sigma_c^2 = \frac{T_p^2}{12}\left(4\sigma_f^2 + \bar{f}^2\right) \quad \text{[unitless], and} \tag{136}$$

$$\rho = \sqrt{\frac{3\sigma_f^2}{4\sigma_f^2 + \bar{f}^2}} \quad \text{[unitless]}. \tag{137}$$

Although the individual pulses all have $\sigma^2_{f_m} = 0\,\text{Hz}^2$, the combined pulse has a frequency variation in (135) related to the spread of the individual frequencies. If the $M$ equal-amplitude CW pulses are uniformly spaced throughout a frequency band having width $W$ [units: Hz], the frequency variance is $\sigma_f^2 = W^2(M+1)/[12(M-1)]$ [units: Hz$^2$], which is greater than the $W^2/12$ achieved by an LFM pulse with an equivalent bandwidth. However, the form of $\rho$ in (137) suggests that the potential improvement in time-delay esitmation comes at the cost of an increase in the coupling between time delay and Doppler.

Using (135) and (137) in (29) and noting $S^{\text{d}}_{\text{tot}} = MS_0$ from (113) results in

$$\text{Var}\{\hat{\tau}\} \geq \frac{\left(1 + 4\sigma_f^2/\bar{f}^2\right)}{8\pi^2 S^{\text{d}}_{\text{tot}}\sigma_f^2\left(1 + \sigma_f^2/\bar{f}^2\right)} \quad \text{[units: s}^2\text{]} \tag{138}$$

for the CLRB on time-delay estimation with the comb waveform when the radial velocity is unknown. In contrast to the bound for a single CW pulse in (35), which is proportional to $T_p^2$, this is inversely proportional to the frequency variance. Using the above result for $\sigma_f^2$ when the frequencies are uniformly spaced, (138) becomes comparable to the CRLB for an LFM pulse with known Doppler in (36). As seen in [39], the pulses do not need to be equally weighted, which can accentuate or dampen the improvement, depending on how the overall spectrum is shaped. However, it is important to recall that the CRLB represents small errors and that it fails when large

errors are common (see the discussion in Sect. 2.2). Large errors are more likely to occur when there are high sidelobes in the ambiguity or autocorrelation function, which is a distinct concern for comb waveforms [39]. It is not uncommon for other considerations to play an important role in the design of comb waveforms, including reverberation suppression, envelope consistency, and the size/extent/location of the sidelobes [37–40]. The potential performance in time-delay estimation indicated by (138) is one factor.

The CRLB for estimating radial velocity,

$$\mathrm{Var}\{\hat{v}\} \geq \frac{3c_w^2}{8\pi^2 S_{\mathrm{tot}}^{\mathrm{d}} T_p^2 \bar{f}^2 \left[1 + \sigma_f^2/\bar{f}^2\right]} \quad \text{[units: m}^2\text{/s}^2\text{]}, \tag{139}$$

is obtained by using the above parameters in (31). Compared to (32), this result is marginally better than $M$ observations of a CW pulse at the average frequency (or one observation with an SNR $M$ times larger) with the inclusion of the term in brackets in the denominator of (139). It is also identical to the bound obtained when the echoes are assumed to be incoherent and the results of Sect. 4.3 are employed.

## 5.2 Sequences of identical pulses

Suppose a train of $M$ identical pulses is projected with consistent conditions between pulses so their echoes have the same SNR ($S_0^{\mathrm{d}}$). Let the duration and bandwidth of an individual pulse be, respectively, $T_0$ [units: s] and $W_0$ [units: Hz]. Each pulse has the same characteristic time-frequency parameters, which will also be denoted by a subscript '0' (e.g., $\bar{f}_0$ or $\sigma_{c_0}^2$). As such, they must be projected with no overlap in time and therefore satisfy the orthogonality requirements of Sect. 4. When the pulses are close together in time and the echoes are assumed to be coherent, this scenario might represent the use of a wavetrain to be processed coherently with a Doppler filter bank, in which case the bounds on performance described in Sect. 4.2 apply. When the time between pulses is large, however, the echoes are likely to have different bulk phases. This is representative of scenarios where echoes from multiple consecutive pings are used to estimate radial velocity and refine estimates of time delay and requires use of the results presented in Sect. 4.3.

The performance bounds for radial-velocity estimation in these two cases are illustrated in Fig. 3 for a sequence of equally spaced LFM pulses. As expected, the performance of the pulse train is always better than using a single pulse with an unknown time delay (black solid line). In this example, coherent processing is expected to achieve better radial-velocity estimation performance than a single pulse with a known time delay (black dotted line). However, incoherent processing only achieves this benchmark when the pulses have enough separation in time. The time-delay-based performance bounds from Sect. 3.4 (gray dotted lines) illustrate the efficacy of the approach in that they are very close to the CRLBs for incoherent pulses.

From a design perspective, the performance bounds only need to be low enough for the environmental conditions (e.g., Doppler spreading) to dominate the estimation errors. Although these vary with many factors (e.g., sea-state, internal-wave conditions, platform motion, etc.), they can be quite small under calm conditions or at short range (e.g., spreading standard deviations well under 1 m/s). Assuming Gaussian-distributed estimation errors and a 95% confidence interval of 0.1 m/s ($\approx$ 0.2 kn) requires a standard deviation in the radial-velocity estimator of approximately 0.025 m/s. As seen in Fig. 3, this performance might be achieved either using coherent processing

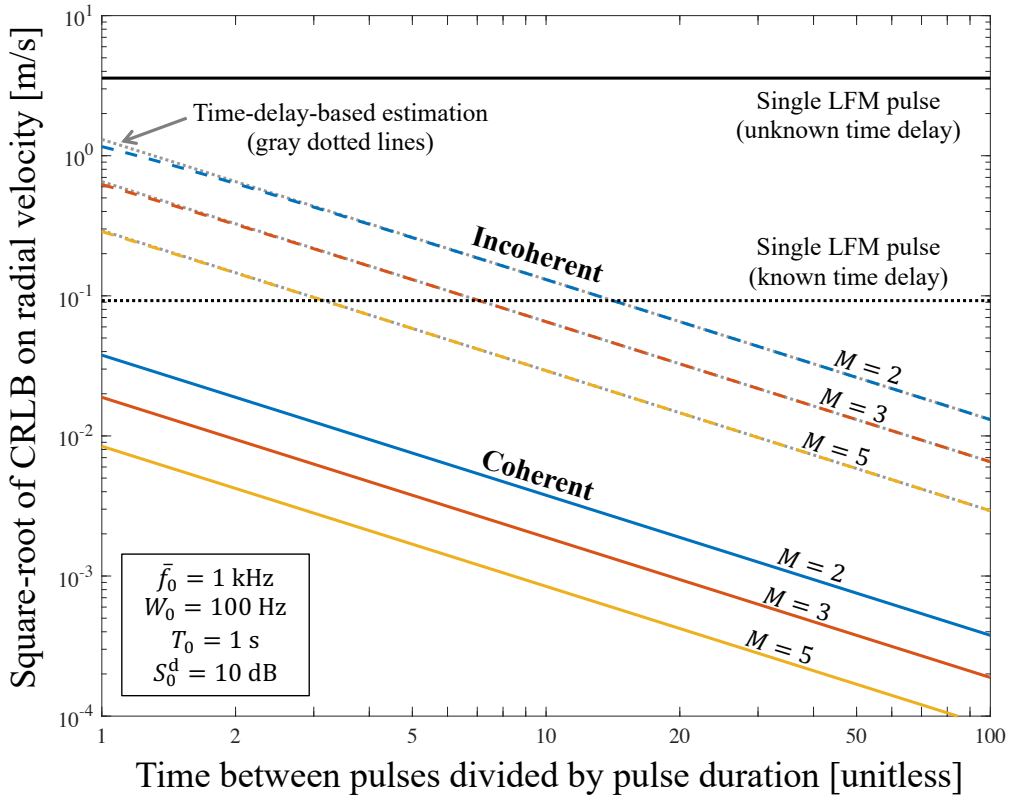


Figure 3: Square root of the CRLB for unbiased estimation of radial velocity for a uniform, equally spaced LFM pulse train as a function of the time between pulses relative to the pulse duration.

with only a small separation between pulses or with incoherent processing and larger separations (e.g., across multiple pings).

The themes seen in this example are supported by the equations for the bounds derived for coherent echoes in Sect. 5.2.2 and those for the incoherent case in Sect. 5.2.3. As will be seen, center frequencies will typically drive performance in the former, whereas bandwidths drive performance in the latter.

### 5.2.1 Characterizing the pulse train

Although the example shown in Fig. 3 assumed the pulses were projected with a constant time separation, the theoretical results will be seen to depend only on the average and variance of $\hat{\delta}_m$ from (115), which is the time between the center of the $m$th pulse and the onset time of the reference pulse. Because the pulses are identical, the average simplifies to

$$\hat{\delta} = \frac{1}{M}\sum_{m=1}^{M}\hat{\delta}_m = \bar{\delta} + \frac{T_0}{2} = \bar{t}^{\mathrm{tx}} + \frac{T_0}{2} - t_\star^{\mathrm{tx}} \quad \text{[units: s]} \tag{140}$$

where $\bar{\delta} = \frac{1}{M}\sum_{m=1}^{M}\delta_m$ [units: s] and $\bar{t}^{\mathrm{tx}} = \frac{1}{M}\sum_{m=1}^{M}t_m^{\mathrm{tx}}$ [units: s]. When the reference pulse onset is at the center of the pulse train, it can be seen that $t_\star^{\mathrm{tx}} = \bar{t}^{\mathrm{tx}} + \frac{T_0}{2}$ so $\bar{\delta} = -T_0/2$ and $\hat{\delta} = 0\,\mathrm{s}$, which leads to additional simplification in the bounds for time delay.

Noting that $\hat{\delta}_m = \delta_m + T_0/2$, it is clear that the variance formed over $\hat{\delta}_m$ is identical to that formed over $\delta_m$ or $t_m^{\text{tx}}$,

$$\sigma_{\hat{\delta}}^2 = \sigma_{\delta}^2 = \frac{1}{M}\sum_{m=1}^{M}\left(\delta_m - \bar{\delta}\right)^2 = \frac{1}{M}\sum_{m=1}^{M}\delta_m^2 - \bar{\delta}^2 = \frac{1}{M}\sum_{m=1}^{M}\left(t_m^{\text{tx}} - \bar{t}^{\text{tx}}\right)^2 \quad \text{[units: s}^2\text{]}. \tag{141}$$

The representation of the variance as a sample power minus the squared mean is provided in (141) as it is often an easier form to evaluate. As noted in (110), $\sigma_{\delta}^2 = \Delta^2(M^2-1)/12$ [units: s$^2$] when there is a constant pulse repetition interval of $\Delta$ [units: s].

### 5.2.2 Coherent echoes

If the bulk phase of the echoes from repeated projection of a pulse is assumed to be constant, CRLBs are formed using the characteristic time-frequency parameters defined in Sect. 4.2. Using constant parameters in (116)–(120) leads to the result

$$\sigma_c^2\left(1-\rho^2\right) = \sigma_{c_0}^2\left(1-\rho_0^2\right) + \sigma_{\delta}^2 P_{f_0} \quad \text{[unitless]}. \tag{142}$$

The CRLB on radial velocity estimation is then obtained from (31) as

$$\text{Var}\{\hat{v}\} \geq \frac{c_w^2}{32\pi^2 M S_0^{\text{d}}\left[\sigma_{c_0}^2\left(1-\rho_0^2\right) + \sigma_{\delta}^2 P_{f_0}\right]} \quad \text{[units: m}^2\text{/s}^2\text{]}. \tag{143}$$

Beyond the improvement in total SNR (a factor $M$), this illustrates how increasing the time between pulse transmissions, which increases $\sigma_{\delta}^2$, improves estimation of radial velocity. Recalling that $P_{f_0} = \sigma_{f_0}^2 + \bar{f}_0^2$, it can also be seen that performance will typically be driven by the center frequency of the pulses, compared with the bandwidth dependence observed for a single LFM pulse in (40). Additionally, this result applies to HFM pulse trains even though the bound does not exist for single pulses (recall $\rho_0 = \pm 1$ for HFM pulses).

The terms contributing to the CRLB for time-delay estimation for the uniform pulse train have the form

$$\sigma_f^2\left(1-\rho^2\right) = \frac{\sigma_{f_0}^2\left[\sigma_{c_0}^2(1-\rho_0^2)\right]}{\sigma_{\delta}^2 P_{f_0} - 2\hat{\delta}(1-\rho_0)\sigma_{c_0}\sigma_{f_0} + \left[\sigma_{c_0} + \hat{\delta}\sigma_{f_0}\right]^2} \quad \text{[units: Hz}^2\text{]}. \tag{144}$$

By setting the time-delay origin (for estimation) to that associated with the center of the wavetrain (i.e., $\bar{\delta} = -T_0/2$ or $\hat{\delta} = 0\,\text{s}$), the result in (144) simplifies to

$$\sigma_f^2\left(1-\rho^2\right) = \sigma_{f_0}^2\left[1 - \frac{\rho_0^2}{1 + \sigma_{\delta}^2 P_{f_0}/\sigma_{c_0}^2}\right] \quad \text{[units: Hz}^2\text{]}. \tag{145}$$

Using this in (29), the CRLB for time-delay estimation is seen to be

$$\text{Var}\{\hat{\tau}\} \geq \frac{1}{8\pi^2 M S_0^{\text{d}}\sigma_{f_0}^2\left[1 - \frac{\rho_0^2\sigma_{c_0}^2}{\sigma_{c_0}^2 + \sigma_{\delta}^2 P_{f_0}}\right]} \quad \text{[units: s}^2\text{]}. \tag{146}$$

As $\sigma_{\delta}^2$ is increased, time-delay estimation performance tends to that obtained by a single pulse with known Doppler and an SNR $M$ times larger (i.e., the term in brackets tends to one).

The correlation coefficient between time delay and Doppler estimates in this scenario (i.e., $\hat{\delta} = 0\,\mathrm{s}$) is

$$\rho = \frac{\rho_0}{\sqrt{1 + \sigma_\delta^2 P_{f_0}/\sigma_{c_0}^2}} \quad \text{[unitless]}. \tag{147}$$

This illustrates how the use of multiple pulses can significantly reduce the correlation between the two estimates.

### 5.2.3 Incoherent echoes

When the bulk phase differs from one echo to the next, the CRLBs need to be constructed from the results presented in Sect. 4.3. Using constant characteristic time-frequency parameters in (121) produces

$$\left\{\mathrm{FIM}^{-1}(\tau_\star, \eta, \boldsymbol{\psi})\right\}_{\tau_\star,\eta} = \frac{1}{8\pi^2 M S_0^{\mathrm{d}}} \begin{bmatrix} \sigma_{f_0}^2 & -\sigma_{f_0}\sigma_{c_0}\rho_0 - \hat{\delta}\sigma_{f_0}^2 \\ -\sigma_{f_0}\sigma_{c_0}\rho_0 - \hat{\delta}\sigma_{f_0}^2 & \sigma_{c_0}^2 + 2\rho_0\hat{\delta}\sigma_{f_0}\sigma_{c_0} + \left(\sigma_\delta^2 + \hat{\delta}^2\right)\sigma_{f_0}^2 \end{bmatrix}^{-1} \tag{148}$$

where $\hat{\delta} = \bar{\delta} + T_0/2$ [units: s] from (140). The determinant of the matrix within the brackets in (148) is

$$|\cdot| = \sigma_{f_0}^2\left[\sigma_{c_0}^2\left(1-\rho_0^2\right) + \sigma_\delta^2\sigma_{f_0}^2\right], \tag{149}$$

which does not depend on $\hat{\delta}$. Using this to construct the CRLB on radial velocity from the $(2,2)$ element of (148) as described in Sect. 4.3 results in

$$\mathrm{Var}\{\hat{v}\} \geq \frac{c_w^2}{32\pi^2 M S_0^{\mathrm{d}}\left[\sigma_{c_0}^2\left(1-\rho_0^2\right) + \sigma_\delta^2\sigma_{f_0}^2\right]} \quad \text{[units: } \mathrm{m}^2/\mathrm{s}^2\text{]}. \tag{150}$$

This only differs from the case of coherency between echoes in the last term in the denominator, which contains $\sigma_{f_0}^2$ here and $P_{f_0} = \sigma_{f_0}^2 + \bar{f}_0^2$ in (143). As is often the case, incoherent processing results in performance driven (inversely) by bandwidth rather than center frequency.

Making the simplification described in Sect. 5.2.2 with respect to $\hat{\delta} = 0\,\mathrm{s}$ results in a CRLB for estimating time delay of

$$\mathrm{Var}\{\hat{\tau}\} \geq \frac{1}{8\pi^2 M S_0^{\mathrm{d}}\sigma_{f_0}^2\left[1 - \frac{\rho_0^2\sigma_{c_0}^2}{\sigma_{c_0}^2 + \sigma_\delta^2\sigma_{f_0}^2}\right]} \quad \text{[units: } \mathrm{s}^2\text{]}. \tag{151}$$

The result in (151) is similar to that seen in (146), with the exception of the $P_{f_0}$ term found within the brackets, which is replaced here by $\sigma_{f_0}^2$. However, the difference only acts to slow the convergence of the term in brackets to one. In the limit as $\sigma_\delta^2 \to \infty$, the CRLBs in (146) and (151) tend to the same limit, which is $M$ times smaller than that for a single pulse with known Doppler. By increasing the separation between pulses, the lack of coherency between the echoes eventually has a negligible impact on estimation of the time delay.

Similar to the coherent/incoherent-echo differences noted above, the correlation coefficient between time delay and Doppler estimates can be shown to be

$$\rho = \frac{\rho_0}{\sqrt{1 + \sigma_\delta^2 \sigma_{f_0}^2 / \sigma_{c_0}^2}} \quad \text{[unitless]}, \tag{152}$$

which is (147) with the $P_{f_0}$ replaced by $\sigma_{f_0}^2$.

As a final note, the large-$\sigma_\delta^2$ limits in (150) and (151) are precisely the bounds obtained for time-delay-based estimation found in Sect. 3.4. This does not imply these estimators achieve the bound (i.e., that they are efficient), because the results from Sect. 3.4 utilize bounds on single-pulse time-delay estimation. However, it suggests that they might at high SNR and after accounting for the small SNR losses from mismatch between the echo and matched-filter replica.

### 5.2.4 Uniform LFM pulse trains

Suppose $M$ LFM pulses having duration $T_p$, center frequency $f_c$, and bandwidth $W$ are projected with a pulse repetition interval of $\Delta$ [units: s]. Assuming the echoes are coherent results in the CRLB

$$\mathrm{Var}\{\hat{v}\} \geq \frac{3c_w^2}{8\pi^2 S_{\mathrm{tot}}^{\mathrm{d}} f_c^2 \Delta^2 (M^2-1)\left[1 + \frac{W^2}{12 f_c^2} + \frac{T_p^2 W^2}{15\Delta^2 (M^2-1) f_c^2}\right]} \quad \text{[units: m}^2\text{/s}^2\text{]} \tag{153}$$

on radial velocity. The narrowband case for the coherent combination of an LFM pulse train was evaluated in [22] and results[17] in nearly the same form—the third term inside the brackets in (153), which arises from $\sigma_{c_0}^2(1-\rho_0^2)$ in (143), is zero in [22] owing to the value of $\rho_0 \to 1$ if the LFM pulse is assumed to be narrowband.

If the echoes are incoherent, the CRLB on radial velocity from (150) is

$$\mathrm{Var}\{\hat{v}\} \geq \left[\frac{45c_w^2}{8\pi^2 S^{\mathrm{d}} T_p^2 W^2}\right] \frac{1}{1 + \frac{(M-1)^2\Delta^2}{12T_p^2}} \quad \text{[units: m}^2\text{/s}^2\text{]}, \tag{154}$$

where the term in brackets is the single-pulse bound when time-delay is unknown from (40). This exhibits the anticipated inverse dependence on the squared bandwidth and illustrates the improvement in performance as the number of pulses ($M$) or their spacing relative to their duration ($\Delta/T_p$) increases.

### 5.2.5 Waveform triplets

To demonstrate that the pulses in an identical pulse train do not need to be projected with a constant repetition interval, consider the case of triplets of identical pulses with duration $T_p$ [units: s] and varying inter-pulse delays. Let the onset times of the three pulses be 0 s, $\gamma_1 T_p$, and $(\gamma_1 + \gamma_2)T_p$, where $\gamma_1$ and $\gamma_2$ are unitless factors greater than or equal to one. It is then straightforward to show that

$$\hat{\delta} = \frac{T_p(4\gamma_1 + 2\gamma_2 + 3)}{6} - t_\star^{\mathrm{tx}} \quad \text{[units: s]} \tag{155}$$

[17] To equate the results for the CRLB on velocity in [22, eq. 46] to (153), note that $M = 2N+1$, $W = 2K\Delta f$, $S_{\mathrm{tot}}^{\mathrm{d}} = \mathrm{SNR}_{\mathrm{integr}}$, $\Delta = \mathrm{IPP}$, and $\Delta^2(M^2-1) = T_D^2$, with terms from [22] on the right sides of each equation.

and

$$\sigma_\delta^2 = \frac{2}{9} T_p^2 \left(\gamma_1^2 + \gamma_1\gamma_2 + \gamma_2^2\right) \quad \text{[units: s}^2\text{]}. \tag{156}$$

Setting $\gamma_1 = \gamma_2 = \gamma$ produces a constant time between pulses of $\Delta = \gamma T_p$ and (156) simplifies to $\sigma_\delta^2 = 2\gamma^2 T_p^2/3$, which is the same results as $\sigma_\delta^2 = \Delta^2(M^2-1)/12$ from (110) with $M = 3$.

These can be used in the results of Sects. 5.2.2 & 5.2.3 to obtain the bounds for estimating radial velocity and time delay. As an example, consider projecting HFM pulses, for which $\rho_0 = 1$ and so simplifies the multiple-pulse results. If the frequency band is $(f_0, f_1)$, then from Table 1 (pg. 16) $P_{f_0} = f_0 f_1$, and $\sigma_f^2 \approx (f_1 - f_0)^2/12$. Using (156) in (143) then yields

$$\mathrm{Var}\{\hat{v}\} \geq \frac{3c_w^2}{64\pi^2 S_0^{\mathrm{d}} f_0 f_1 T_p^2 \left(\gamma_1^2 + \gamma_1\gamma_2 + \gamma_2^2\right)} \quad \text{[units: m}^2\text{/s}^2\text{]} \tag{157}$$

for coherent echoes and

$$\mathrm{Var}\{\hat{v}\} \geq \frac{9c_w^2}{16\pi^2 S_0^{\mathrm{d}} (f_1 - f_0)^2 T_p^2 \left(\gamma_1^2 + \gamma_1\gamma_2 + \gamma_2^2\right)} \quad \text{[units: m}^2\text{/s}^2\text{]} \tag{158}$$

from (150) for incoherent echoes where $S_0^{\mathrm{d}}$ is the linear-quantity SNR in the echo from a single pulse. Recalling that the CRLB on radial velocity when time delay is unknown does not exist for a single HFM pulse (Sect. 2.4.2), both of these scenarios represent an improvement even when $\gamma_1$ and $\gamma_2$ are not large.

### 5.2.6 Up-sweeping FM pulses are better for predicting range

An interesting result [11, 29] found when accounting for the effects of using a sequence of up- or down-sweeping FM pulses in a tracking algorithm to predict the position of an OOI is that up-sweeps provide better range estimation. This can be examined here by accounting for $\hat{\delta}$ in the CRLB for time delay, which leads to

$$\mathrm{Var}\{\hat{\tau}\} \geq \frac{\sigma_{c_0}^2 + 2\rho_0\hat{\delta}\sigma_{f_0}\sigma_{c_0} + \left(\sigma_\delta^2 + \hat{\delta}^2\right)\sigma_{f_0}^2}{8\pi^2 M S_0^{\mathrm{d}} \sigma_{f_0}^2 \left[\sigma_{c_0}^2(1-\rho_0^2) + \sigma_\delta^2\sigma_{f_0}^2\right]} \quad \text{[units: s}^2\text{]} \tag{159}$$

when the echoes are assumed to be incoherent. For waveforms where $|\rho_0| \approx 1$, this can be approximated by

$$\mathrm{Var}\{\hat{\tau}\} \geq \frac{\left[\frac{\sigma_{c_0}}{\sigma_{f_0}} + \mathrm{sign}\{\rho_0\}\,\hat{\delta}\right]^2 + \sigma_\delta^2}{8\pi^2 M S_0^{\mathrm{d}} \sigma_{f_0}^2 \sigma_\delta^2} \quad \text{[units: s}^2\text{]}, \tag{160}$$

where $\rho_0$ is positive for up-sweeps and negative for down-sweeps.

Suppose the $M$ pulses used in the estimation are projected every $\Delta$ [units: s] with onset times $t_m^{\mathrm{tx}} = (m-1)\Delta$ [units: s] for $m = 1,\ldots,M$ and that the onset time of the reference pulse (the one for which the range is being estimated) is $t_\star^{\mathrm{tx}} = M\Delta$ [units: s]. This represents a prediction of the

range of the OOI corresponding to the time at which the next pulse is to be projected. For this scenario,

$$\hat{\delta} = \bar{\delta} + \frac{T_p}{2} = \frac{1}{M}\sum_{m=1}^{M} t_m^{\text{tx}} - t_\star^{\text{tx}} + \frac{T_p}{2} = \frac{-(M+1)\Delta}{2} + \frac{T_p}{2} < 0 \quad \text{[units: s]}, \tag{161}$$

so the value of $\hat{\delta}$ is negative (recall that $\Delta \geq T_p$ for identical pulses) and has a magnitude that is roughly half the temporal span of the pulse train. In (160), choosing a waveform for which $\rho_0$ is positive (e.g., an up-sweeping FM) when $\hat{\delta}$ is negative is clearly better than one for which $\rho_0$ is negative. Conversely, if the projection time of the pulse prior to those being used were of interest (e.g., the retrodiction problem for which $t_\star^{\text{tx}} = -\Delta$), then $\hat{\delta} > 0\,\text{s}$ and choosing a waveform for which $\rho_0$ is negative (e.g., a down-sweeping FM) is better than one with $\rho_0 > 0$.

This result corroborates the analysis found in [11,29], which considers the problem in the context of a tracker. These authors describe the result as depending on the sign of the correlation between estimates of range and radial velocity—in particular that better performance is achieved when the signs differ between the correlation for a single pulse and that characterizing the prior information in the tracker because there is less overlap in the uncertainty when they are combined. An alternative explanation introduced in Sect. 4.4 can be found in noting that having the highest frequencies in the waveform (which provide the most information on Doppler) closer to the time of the reference pulse provides the best performance. In the context of multiple pulses, any reference times after the center of the pulse train are closer to the higher frequencies in up-sweeps than those found in down-sweeps. This interpretation directly implies that up-sweeping pulses are better for prediction, down-sweeping ones for retrodiction, and suggests a weakening of the effect as the reference pulse becomes more distant.

The utility of the simple result found in (160) is that it can provide guidance on how frequently a pulse should be projected in order to minimize the CRLB on predicting OOI range at the next update. Given $\zeta = W/f_c$ [unitless] for an LFM or HFM pulse and a fixed number of pulses ($M$) to be used in the prediction, the optimal pulse repetition interval (PRI) is

$$\Delta_{\text{opt}} = \frac{1}{M+1}\left(\frac{2f_c}{W} + 1\right) T_p \quad \text{[units: s]}. \tag{162}$$

For example, using $M = 3$ echoes from a waveform with 100 Hz of bandwidth centered at 2 kHz (i.e., $\zeta = 1/20$) should have a PRI of $\Delta_{\text{opt}} = 10.25 \cdot T_p$ [units: s]. When the range scale (dictating the minimum time between pulses) does not permit projecting pulses so rapidly, an analysis using the general results in Sect. 4.3 might reveal if placing them in different frequency bands achieves similar results.

As a final note, recall that the performance of the time-delay-based estimator presented in Sect. 3.4 depended on $\bar{d} = \bar{b} - \bar{\delta}$. Noting that $\sigma_{c_0}/\sigma_{f_0} \approx T_p f_c/W$ [units: s] for LFM and HFM waveforms, which is essentially the same as $|\bar{b}|$ for these waveforms, it can be seen that the term within the brackets in the numerator of (160) is very similar to $\bar{d}$. This suggests the time-delay-based estimator has similar behavior.

### 5.2.7 Uniform PLFM pulse trains

Recall that the power-law FM (PLFM) pulse described in Sect. 2.3.1 can represent the basic CW ($p = 0$), LFM ($p = 1$), and HFM ($p = -1$) sonar waveforms. It also provides some measure of

control of the Doppler and delay characteristics for a given waveform bandwidth, as was detailed in [7] in terms of the ambiguity function. The authors in [7] described a reduction in performance under reverberation-limited conditions as a consequence of this benefit, which suggests not letting $p$ get too close to zero. Up-sweeping PLFM pulses are examined here in Figs. 4 & 5 for multiple-pulse estimation of delay and Doppler through the CRLBs for incoherent echoes. These figures also convey the inherent compromise between estimating Doppler and delay when using only one of the basic sonar pulses. The bounds shown in the figures are formed from the incoherent-echo results found in (150) and (151) using the characteristic time-frequency parameters of the PLFM pulse presented in Sect. 2.3.2. Each echo had SNR $\approx 17.3\,\mathrm{dB}$, center frequency $f_c = 2\,\mathrm{kHz}$, bandwidth $W = 200\,\mathrm{Hz}$, and duration $T_p = 0.2\,\mathrm{s}$. The SNR was chosen using (32) so the square root of the CRLB for estimating radial velocity with a single CW pulse at $f_c$ was $0.1\,\mathrm{m/s}$.

In Fig. 4, the square root of the CRLB on unbiased estimators of time delay is shown as a function of $p$ for a single pulse (solid blue line), two consecutive pulses (reddish-brown line), and five consecutive pulses (gold line). The solid lines represent the case where both the time delay and radial velocity of the echo are unknown. The blue dotted line is for a single pulse when the radial velocity is known. The poor performance expected for time-delay estimation with CW pulses is evident at $p = 0$, but also seen near $p = -1$ for a single HFM pulse. The latter occurs because these results assume concurrent estimation of radial velocity and the HFM has full coupling ($\rho = 1$) between delay and Doppler, as was discussed in Sect. 2.4.2. Using multiple HFM pulses, however, demonstrates performance only marginally worse than that of the LFM pulse. An interesting result is seen here and in Fig. 5 in the small magnitude of the slope of the multiple-pulse bounds except when $p$ nears zero. This implies that there may be little to gain in multiple-pulse estimation performance by modifying $p$ from the basic LFM or HFM waveforms.

The dotted blue line in Figs. 4 or 5 represents the bound when one parameter is known. As described in Sect. 3, this result is useful in radial-velocity estimation when a (biased) time-delay estimate is obtained from a single matched filter (e.g., with a zero-Doppler replica) and any mismatch with the echo is absorbed as a reduction in SNR. The results seen in Fig. 5 illustrate that unbiased estimation with multiple pulses can still have a higher variance than a biased estimate from a single pulse, although separating the pulses more in time can change this, as was shown in Fig. 3.

The blue dots in these figures are obtained using the standard single-pulse results and confirm the corresponding PLFM cases. Near $p = 0$ in Fig. 5 (detailed in the inset graph), the PLFM results might be expected to tend to the standard CW pulse results using $f_0$ (when $p \to 0$ from below) or $f_1$ (when $p \to 0$ from above). However, using the asymptotic values of the waveform parameters found at the end of Sect. 2.3.2 as $p \to 0$ from above with $f_0$ and $f_1$ held constant, the CRLB for estimating radial velocity when delay is also unknown can be shown to be four times larger than (32) (replacing $f_c$ with $f_1$). The factor of four arises from the limit shown in (26), $\rho \to \sqrt{3}/2$, which leads to $1/(1-\rho^2) \to 4$. In Fig. 5, the limits on the square root of the CRLB for a single PLFM pulse with unknown time delay (solid blue line) tend to points twice as large as those observed when time delay is assumed to be known (using $M$ pulses results in a factor $2/\sqrt{M}$). This abnormality occurs because the bandwidth of the PLFM in this example is fixed; letting it tend to zero with $p$ (in particular, $W \propto p^2$) produces the result expected from (32). However, this negates the desirable bandwidth-related properties of the PLFM.

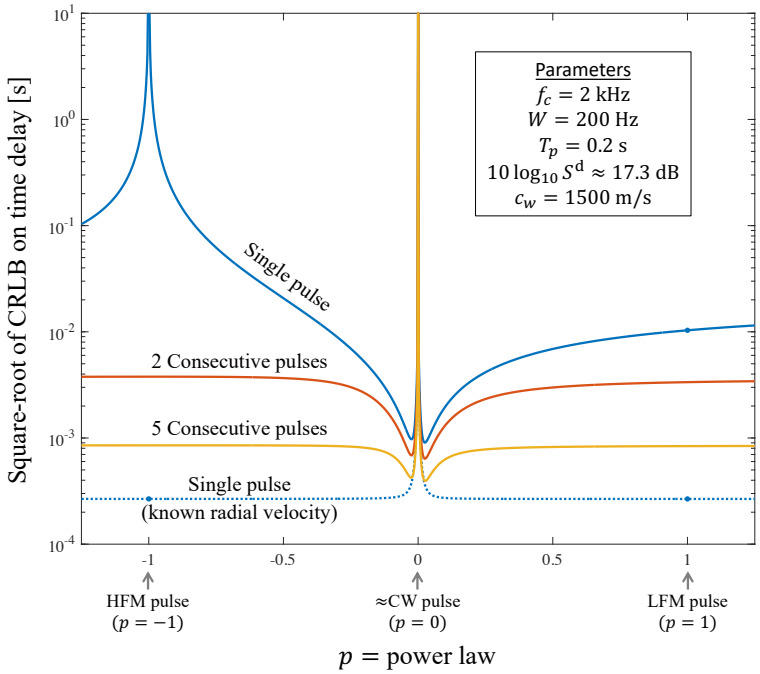


Figure 4: Square root of the CRLB for estimation of time delay as a function of the power law in a PLFM waveform for 1, 2, and 5 consecutive pulses with incoherent echoes. Solid lines represent the case of unknown radial velocity.

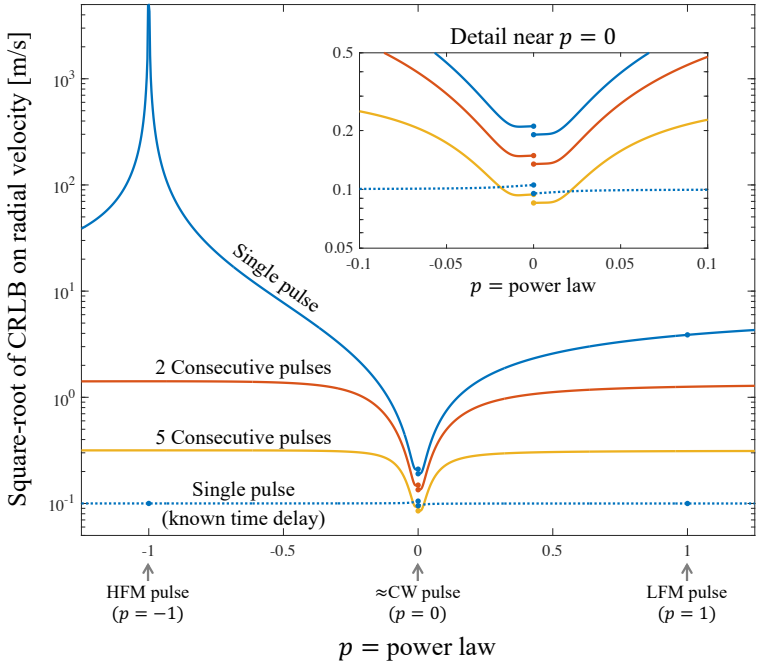


Figure 5: Square root of the CRLB for estimation of radial velocity as a function of the power law in a PLFM waveform for 1, 2, and 5 consecutive pulses with incoherent echoes. Solid lines represent the case of unknown time delay.

## 5.3 Reconstituting an LFM pulse

Consider an LFM pulse with duration $T_p$, bandwidth $W$, and center frequency $f_c$. It can be described as comprising $M$ consecutive LFM sub-pulses with each occupying $1/M$ of the duration and $1/M$ of the bandwidth. Performance bounds for estimation of radial velocity from the sub-pulses are examined in this section, initially under the assumption that the echo from the OOI is a single-path reflection from a point target. With no spreading losses, the SNR in each sub-pulse echo is $S_m^{\mathrm{d}} = S_{\mathrm{tot}}^{\mathrm{d}}/M$ under both noise- and reverberation-limited conditions. As might be expected, coherent processing of the sub-pulses achieves the full-pulse coherent-processing result found in Sect. 2.4.2. In Sect. 5.3.2, the bound for incoherent processing is found to be nominally $M^2/5$ times greater than the full-pulse coherent-processing result when $M$ is three or larger, owing to the compounding of the reduced SNR and the reduced temporal resolution of each sub-pulse. In Sect. 5.3.3, it is seen that the bound from Sect. 3.4 for the time-delay-based approach to estimating radial velocity from multiple pulses is only marginally larger than the CRLB for incoherent echoes, which potentially provides a nearly efficient estimation approach (i.e., the estimator will nearly meet the bound at high SNR).

These results imply coherent processing of the full pulse is the best approach for estimating radial velocity when there is no spreading. As discussed in Sect. 5.3.2, temporal spreading losses would typically encourage incoherent processing after splitting the full pulse in half and sometimes in thirds. However, at some point the $M^2/5$ multiplicative-factor increase in the bound becomes too much to counter.

Although the results presented here are derived for an up-sweeping LFM, they apply to a down-sweeping one as well. In support of the analysis presented in this section, the characteristic time-frequency parameters of the sub-pulses are presented in Sect. 5.3.4 along with a number of intermediate terms encountered when the results are derived.

### 5.3.1 Coherent echoes

Using the characteristic time-frequency parameters for the sub-pulses (as defined in Sect. 5.3.4) in the parameters for coherent echoes from (116)–(120) with a constant SNR will produce (after prodigious amounts of algebra) the results shown in Table 1 (pg. 16) for the full LFM pulse duration, bandwidth, and center frequency. Although this exercise is left to the diligent reader, the veracity of the claim is straightforward to demonstrate numerically.

### 5.3.2 Incoherent echoes and the impact of spreading loss

Using the definitions and intermediate terms found in Sect. 5.3.4, the inverse FIM from (121) for $M$ equal-SNR incoherent echoes can be shown to be

$$\left\{\mathrm{FIM}^{-1}(\tau_\star, \eta, \boldsymbol{\psi})\right\}_{\tau_\star,\eta} = \frac{3M^2}{2\pi^2 S_{\mathrm{tot}}^{\mathrm{d}}} \left\{ \begin{bmatrix} W^2 & -T_p W f_c \\ -T_p W f_c & T_p^2 f_c^2 + T_p^2 W^2 \frac{(5M^2-4)}{15M^2} \end{bmatrix} \right\}^{-1}, \tag{163}$$

where $S_{\mathrm{tot}}^{\mathrm{d}}$ [unitless] is the SNR for the full LFM pulse. Inverting this, taking the second diagonal and scaling it by $c_w^2/4$ then produces the CRLB for estimation of the radial velocity when the

echoes are incoherent,

$$\mathrm{Var}\{\hat{v}\} \geq \left[\frac{45c_w^2}{8\pi^2 S_{\mathrm{tot}}^{\mathrm{d}} T_p^2 W^2}\right] \frac{M^2}{5-\frac{4}{M^2}} \quad \text{[units: m}^2/\text{s}^2\text{]}. \tag{164}$$

The term in brackets is the bound for the full pulse from (40), which would be attained if the sub-pulse echoes were coherent. The remaining part of (164), the function $M^2/(5-4/M^2)$, characterizes the factor by which the bound increases when the sub-pulse echoes are incoherent. The first few values of this function are

$$\begin{array}{rcccccccc} M & = & 1 & 2 & 3 & 4 & 5 & 6 & \\ \frac{M^2}{5-\frac{4}{M^2}} & = & 1 & 1 & 1.98 & 3.37 & 5.17 & 7.36 & \rightarrow \frac{M^2}{5}. \end{array} \tag{165}$$

Interestingly, it equals one for both $M = 1$ and $M = 2$, which implies there may be no loss when the LFM is split in half and processed incoherently. However, any additional deconstruction leads to a bound that tends toward a factor $M^2/5$ larger than that for coherent processing.

In scenarios where spreading losses (which increase with bandwidth) cause the SNR at bandwidth $W/M$ to be greater than $S_{\mathrm{tot}}^{\mathrm{d}}/M$ (e.g., see [41, Fig. 9(a)] for an example obtained from experimental data), there may be some gain in performance when $M$ is small. Suppose the SNR observed for the full LFM pulse is represented by an unspread total SNR ($S_{\mathrm{unspr}}^{\mathrm{d}}$ [unitless]) reduced by a factor $L_{\mathrm{esl}}(W)$ [unitless] to account for the spreading,

$$S_{\mathrm{tot}}^{\mathrm{d}} = \frac{S_{\mathrm{unspr}}^{\mathrm{d}}}{L_{\mathrm{esl}}(W)} \quad \text{[unitless]}. \tag{166}$$

The loss term is unity (i.e., no loss) when $W = 0\,\mathrm{Hz}$ and is generally assumed to be monotonically increasing with bandwidth. The SNR in one of $M$ sub-pulses of the LFM is then

$$S_m^{\mathrm{d}} = \frac{S_{\mathrm{unspr}}^{\mathrm{d}}}{M L_{\mathrm{esl}}(W/M)} = \frac{S_{\mathrm{tot}}^{\mathrm{d}} L_{\mathrm{esl}}(W)}{M L_{\mathrm{esl}}(W/M)} \geq \frac{S_{\mathrm{tot}}^{\mathrm{d}}}{M} \quad \text{[unitless]}. \tag{167}$$

When there is no spreading, $L_{\mathrm{esl}}(W) = L_{\mathrm{esl}}(W/M) = 1$ and the result presented in (164) holds. As in the unspread case, the $M$ in the denominator accounts for a reduction in the total energy of a single sub-pulse in noise-limited scenarios or the increase in the temporal extent of the sonar resolution cell in the reverberation-limited case.

When there is spreading, the total SNR achieved by $M$ sub-pulses having the SNR in (167) is

$$M S_m^{\mathrm{d}} = \frac{S_{\mathrm{unspr}}^{\mathrm{d}}}{L_{\mathrm{esl}}(W/M)} \quad \text{[unitless]}. \tag{168}$$

Using this in lieu of $S_{\mathrm{tot}}^{\mathrm{d}}$ in (164) and forming the ratio between the CRLB using $M$ sub-pulses and that for the full pulse results in

$$\frac{\text{CRLB with } M \text{ sub-pulses}}{\text{CRLB for full pulse}} = \frac{L_{\mathrm{esl}}(W/M) M^2}{L_{\mathrm{esl}}(W)[5-4/M^2]} \quad \text{[unitless]}. \tag{169}$$

If the effect of the spreading is strong enough, this ratio will be less than one (clearly it is unity when $M = 1$) and sub-pulse processing can be expected to yield a better estimate of radial velocity

than full-pulse processing. The logarithmic-quantity energy spreading loss often used in the sonar equation is

$$\mathsf{ESL}(W) = 10\log_{10} L_{\text{esl}}(W) \quad \text{[units: dB]}. \tag{170}$$

Converting (169) to decibels then illustrates that sub-pulse processing is beneficial when

$$\mathsf{ESL}(W) - \mathsf{ESL}\left(\frac{W}{M}\right) > 20\log_{10}(M) - 10\log_{10}\left(5 - \frac{4}{M^2}\right) \quad \text{[units: dB]}. \tag{171}$$

Note that this assumes the spreading only impacts estimation of radial velocity through a reduction in SNR.

Suppose the difference in the spreading losses is approximated by

$$\mathsf{ESL}(W) - \mathsf{ESL}\left(\frac{W}{M}\right) \approx \mathcal{M}\log_{10}(M), \tag{172}$$

where $\mathcal{M}$ is the slope of the loss in units of decibels per decade change in bandwidth. Setting $\mathcal{M} = 10\,\text{dB/decade}$ yields the asymptotic regime (i.e., high bandwidth) of exponential- or Gaussian-shaped spreading [1, pg. 609, Fig. 8.34] and the results of [41, Fig. 9(a)] illustrate a case where $\mathcal{M} < 10\,\text{dB/decade}$. Using this model for the spreading loss implies that incoherent sub-pulse processing might improve estimation of radial velocity when the spreading-loss slope satisfies

$$\mathcal{M} > 20 - \frac{10\log_{10}\left(5 - \frac{4}{M^2}\right)}{\log_{10} M} \quad \text{[units: dB/decade]}. \tag{173}$$

The first few values of the right side of (173) are

$$\begin{array}{rcccccl} M & = & 2 & 3 & 4 & 5 & \\ \mathcal{M} & > & 0 & 6.2 & 8.8 & 10.2 & \text{dB/decade.} \end{array} \tag{174}$$

This suggests there will be an improvement to radial-velocity estimation by splitting an LFM pulse in half and possibly in thirds or fourths when the full-bandwidth waveform is subject to nominal spreading and remains in the asymptotic regime where (172) holds. For $M \geq 5$, the spreading losses need to be exceedingly large and the reduced bandwidth ($W/M$) may bring the spreading out of the asymptotic regime, which yields smaller values of $\mathcal{M}$. Although some gains in radial-velocity estimation are attainable through sub-pulse processing of a high-bandwidth LFM pulse when it is subject to temporal spreading, there is a limit beyond which performance will degrade.

### 5.3.3 Time-delay-based estimation

In addition to the definitions and intermediate terms found in Sect. 5.3.4, the time-delay-based estimation approach requires defining the delay bias per unit Mach number from (82) for the $m$th (up-sweeping LFM) sub-pulse,

$$b_m = \frac{-(T_p/M)\bar{f}_m}{W/M} = \frac{-T_p\bar{f}_m}{W} \quad \text{[units: s]}, \tag{175}$$

and the net delay affecting the $m$th sub-pulse,

$$d_m = \frac{T_p}{M}\left(1 + \frac{M}{2} - m - \frac{M\bar{f}_m}{W}\right) \quad \text{[units: s]}, \tag{176}$$

from (91). When using these definitions, the variance in the net delay across the sub-pulses from (98) is

$$\sigma_d^2 = \frac{T_p^2(M^2-1)}{3M^2} \quad \text{[units: s}^2\text{]}, \tag{177}$$

where each has the same variance in its time-delay estimate (i.e., $\check{\lambda}$, which depends on the sub-pulse SNR and bandwidth, is constant). The variance of each time-delay estimate is obtained from (36) and used with (177) in (104) to obtain the bound

$$\text{Var}\{\hat{v}\} \geq \left[\frac{45c_w^2}{8\pi^2 S_{\text{tot}}^{\text{d}} T_p^2 W^2}\right] \frac{M^2}{5-\frac{5}{M^2}} \quad \text{[units: m}^2\text{/s}^2\text{]} \tag{178}$$

on the variance of the radial-velocity estimate. Note that (178) only differs from (164) by having a '5' in the $5/M^2$ term in the denominator rather than a '4'. This represents a minor penalty for the time-delay-based approach: the bound in (178) is $\approx 7\%$ higher than (164) when $M = 2$ and less than 1% higher when $M = 5$.

### 5.3.4 Characterizing the sub-pulses

In support of the results presented in the previous sections, definitions of the sub-pulses comprising the full LFM pulse, their characteristic time-frequency parameters, and other intermediate terms are presented in this section. Those not delving into the derivations are encouraged to skip ahead to Sect. 5.4, which examines pairs of up- and down-sweeping LFM pulses.

Decomposing an up-sweeping LFM pulse into $M$ sub-pulses results in the $m$th sub-pulse having

$$\text{duration } T_m = \frac{T_p}{M} \quad \text{[units: s]}, \tag{179}$$

$$\text{bandwidth } W_m = \frac{W}{M} \quad \text{[units: Hz]}, \tag{180}$$

$$\text{center frequency } \bar{f}_m = f_c - \frac{W}{2} + \left(m-\frac{1}{2}\right)\frac{W}{M} \quad \text{[units: Hz], and} \tag{181}$$

$$\text{onset time } t_m^{\text{tx}} = (m-1)\frac{T_p}{M} - \frac{T_p}{2} \quad \text{[units: s]} \tag{182}$$

for $m = 1,\ldots,M$. From the LFM-pulse column in Table 1 (pg. 16) this leads to the characteristic time-frequency parameters

$$\sigma_{f_m}^2 = \frac{W^2}{12M^2} \quad \text{[units: Hz}^2\text{]}, \tag{183}$$

$$\bar{c}_m = \frac{T_p W}{12M^2} \quad \text{[unitless]}, \tag{184}$$

$$\sigma_{c_m}^2 = \frac{T_p^2 \bar{f}_m^2}{12M^2}\left(1+\frac{\zeta_m^2}{15}\right) \quad \text{[unitless], and} \tag{185}$$

$$\rho_m = \frac{1}{\sqrt{1+\zeta_m^2/15}} \quad \text{[unitless]}, \tag{186}$$

where $\zeta_m = W_m/\bar{f}_m$ [unitless]. It is also useful to note that

$$\rho_m \sigma_{c_m} \sigma_{f_m} = \frac{T_p W \bar{f}_m}{12M^2} \quad \text{[units: Hz]}, \tag{187}$$

which conveniently does not depend on $\zeta_m$. In addition to the characteristic time-frequency parameters, the pertinent time delay parameters from Table 2 (pg. 30) are required. Assuming a reference time at the center of the pulse (i.e., $t_\star^{\text{tx}} = 0\,\text{s}$) leads to

$$\delta_m = (m-1)\,\frac{T_p}{M} - \frac{T_p}{2} \quad \text{or} \quad \hat{\delta}_m = \left(m - \frac{1}{2}\right)\frac{T_p}{M} - \frac{T_p}{2} \quad \text{[units: s]} \tag{188}$$

as the time delay between, respectively, the onset or center of the $m$th sub-pulse and the onset of the reference pulse.

When the sub-pulses have the same SNR, a number of intermediate terms with the FIM or its inverse simplify into averages over various quantities describing the sub-pulses. To facilitate derivation of the results presented in the previous sections, the following intermediate terms are presented for the reconstituted LFM pulse. The pertinent frequency-related terms are

$$\frac{1}{M}\sum_{m=1}^{M} \bar{f}_m = f_c \quad \text{[units: Hz]}, \quad \frac{1}{M}\sum_{m=1}^{M} \sigma_{f_m}^2 = \frac{W^2}{12M^2} \quad \text{[units: Hz}^2\text{]}, \tag{189}$$

and

$$\frac{1}{M}\sum_{m=1}^{M} \bar{f}_m^2 = f_c^2 + \frac{W^2(M^2-1)}{12M^2} \quad \text{[units: Hz}^2\text{]}. \tag{190}$$

The average of the time-in-units-of-periods variance is

$$\frac{1}{M}\sum_{m=1}^{M} \sigma_{c_m}^2 = \frac{T_p^2 f_c^2}{12M^2}\left[1 + \frac{W^2}{12 f_c^2}\left(1 - \frac{1}{5M^2}\right)\right] \quad \text{[unitless]}. \tag{191}$$

Terms related to the sub-pulse delays include

$$\hat{\delta} = \frac{1}{M}\sum_{m=1}^{M} \hat{\delta}_m = 0 \quad \text{[units: s]} \quad \text{and} \quad \sigma_{\hat{\delta}}^2 = \frac{T_p^2(M^2-1)}{12M^2} \quad \text{[units: s}^2\text{]}. \tag{192}$$

Finally, the relevant cross-terms include

$$\frac{1}{M}\sum_{m=1}^{M} \hat{\delta}_m \bar{f}_m = \frac{W T_p (M^2-1)}{12M^2} \quad \text{[unitless]}, \tag{193}$$

$$\frac{1}{M}\sum_{m=1}^{M} \rho_m \sigma_{c_m} \sigma_{f_m} = \frac{T_p W f_c}{12M^2} \quad \text{[units: Hz]}, \tag{194}$$

and

$$\frac{1}{M}\sum_{m=1}^{M} \rho_m \sigma_{c_m} \sigma_{f_m} \hat{\delta}_m = \left(\frac{T_p W}{12M^2}\right)^2 (M^2-1) \quad \text{[unitless]}. \tag{195}$$

## 5.4 Pairs of up- and down-sweeping LFM pulses

The time-frequency correlation coefficient ($\rho$) of an LFM or HFM pulse, as seen in Table 1 (pg. 16), is positive for up-sweeping waveforms and negative for down-sweeping ones. This diversity suggests that combining up- and down-sweeping waveforms could improve estimation of radial velocity. Consecutively projecting these pulses produces what have been termed up-down (rooftop) and down-up (vee) LFM or HFM waveforms. Concurrent projection with full overlap in frequency produces a cross or X waveform. Although the focus of this section is on LFM pulses, the results are similar for HFM pulses. As discussed in the following sections, each of these combinations has the desired effect of producing a CRLB for estimation of radial velocity driven (inversely) by center frequency as opposed to bandwidth. The bounds are presented in Table 3 and Fig. 6 relative to the CRLB for radial velocity estimation using a CW pulse with the same total duration ($T_p$) and center frequency ($f_c$), which from (32) is

$$\mathrm{Var}\{\hat{v}\} \geq \frac{3c_w^2}{8\pi^2 S_{\mathrm{tot}}^{\mathrm{d}} T_p^2 f_c^2} \quad \text{[units: } \mathrm{m}^2/\mathrm{s}^2\text{]}. \tag{196}$$

These results assume the total duration ($T_p$) and total SNR ($S_{\mathrm{tot}}^{\mathrm{d}}$) are the same across all examples.

Although simultaneously projected up- and down-sweeping LFM pulses are not orthogonal when they occupy the same frequency band, their correlation is small. In this analysis, they are assumed to be orthogonal, which allows evaluation of the X-LFM and the time-delay-based approach to estimating radial velocity (which requires the time-delay estimates to be independent). In most scenarios, the bulk-phase will be the same for waveforms such as these that have similar frequency content and are projected concurrently or consecutively. However, when the probability of detection from the individual pulses is reasonably high, incoherent processing such as the time-delay-based approach of Sect. 3 is appealing for its reduced computational complexity (i.e., it only requires two matched filters as opposed to a Doppler filter bank). As seen in Sect. 5.4.2, the X-LFM waveform has advantages in these scenarios over the up-down and down-up waveforms.

Table 3: CRLB for estimating radial velocity from a pair of up- and down-sweeping LFM pulses with bandwidth $W$, center frequency $f_c$, and total duration $T_p$ relative to that for a CW pulse with the same duration and center frequency as a function of $\zeta = W/f_c$. The upper and lower signs in the $\pm$ symbols in the consecutive-projection column represent, respectively, the up-down and down-up sequences.

| **Bulk phase or processing** | **Consecutive projection** | **Concurrent projection** |
|---|---|---|
| Coherent | $\dfrac{1}{1 \mp \zeta/2 + \zeta^2/10}$ | $\dfrac{1}{1 + 3\zeta^2/20}$ |
| Incoherent | $\dfrac{4}{1 \mp \zeta + 19\zeta^2/60}$ | $\dfrac{1}{1 + \zeta^2/15}$ |
| Time-delay-based | $\dfrac{4}{1 \mp \zeta + \zeta^2/4}$ | 1 |

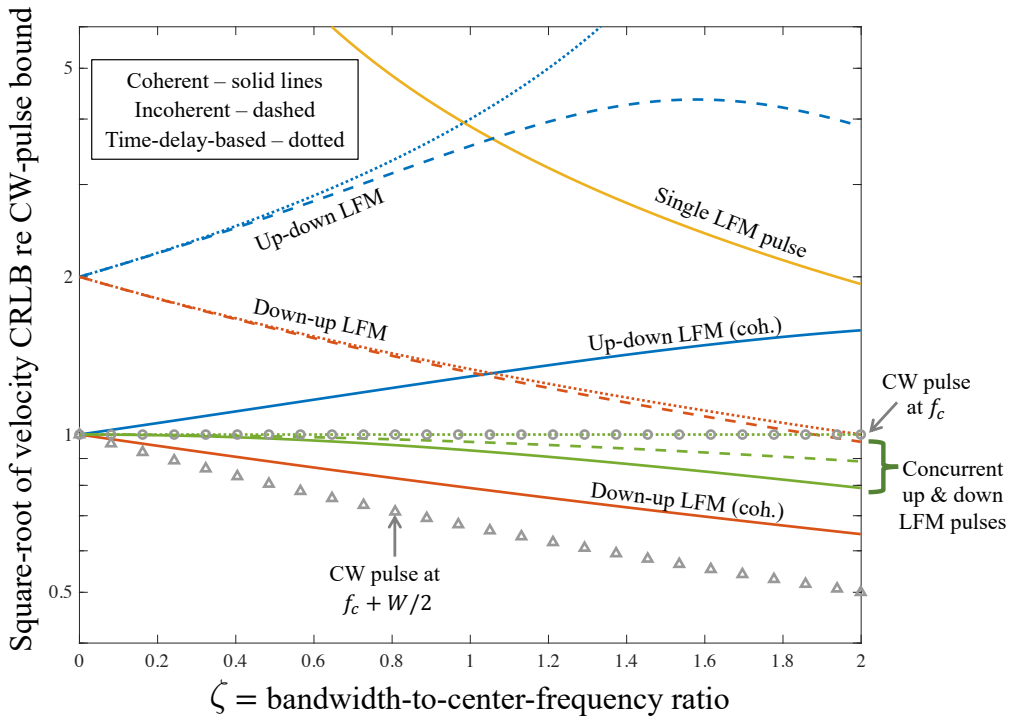


Figure 6: Square root of the CRLB for unbiased estimation of radial velocity relative to that for a CW pulse for combinations of up- and down-sweeping LFM pulses as a function of the bandwidth-to-center-frequency ratio ($\zeta$).

### 5.4.1 Up-down and down-up LFM waveforms

Consider consecutively projecting one LFM of each sweep direction (i.e., an up-down LFM or a down-up LFM), where the two pulses occupy the same frequency band and have duration $T_p/2$ so the total transmit duration is $T_p$. The pertinent time and delay parameters required to derive the various performance bounds are found in Table 4. Using these with the characteristic time-frequency parameters of up- and down-sweeping LFM pulses from Table 1 (pg. 16) in the results of Sects. 3 and 4 leads to the results seen in Fig. 6. Equations for the bounds can be formed by multiplying the functions found in Table 3 under the consecutive-projection column by the CW-pulse bound in (196). Note that the upper and lower symbols in $\mp$ refer to, respectively, the up-down and down-up waveforms.

As might be expected, the coherent results tend to that of the CW pulse as bandwidth is reduced (i.e., the corresponding equations in Table 3 tend to one as $\zeta \to 0$). Similarly, both of the incoherent results for consecutive projection tend to a bound four times larger. As $\zeta \to 0$, this represents the case of using two CW pulses with each having half the SNR ($S^{\mathrm{d}}_{\mathrm{tot}}/2$) and half the duration ($T_p/2$), which leads to the factor-of-four increase:

$$\mathrm{Var}\{\hat{v}\} \geq \underbrace{\frac{1}{2}}_{\text{two pulses}} \cdot \frac{3c_w^2}{8\pi^2 \underbrace{\left(\frac{S^{\mathrm{d}}_{\mathrm{tot}}}{2}\right)}_{\text{half the SNR}} \underbrace{\left(\frac{T_p}{2}\right)^2}_{\text{half the duration}} f_c^2} = 4 \cdot \frac{3c_w^2}{8\pi^2 S^{\mathrm{d}}_{\mathrm{tot}} T_p^2 f_c^2} \quad [\text{units: m}^2/\text{s}^2]. \tag{197}$$

With the exception of the time-delay-based approach for an up-down LFM waveform with a high

bandwidth-to-center-frequency ratio, the bounds are dominated by the center frequency as opposed to the bandwidth dependence of a single LFM pulse seen in (40). Compared to using an equivalent-duration single LFM pulse (gold line), the coherent pairs of up- and down-sweeping pulses (solid blue and reddish-brown lines) are significantly better when they are not strongly broadband. Although the down-up LFM pair is better than an equivalent duration CW pulse at the center frequency, it is not as good as placing the CW at the highest frequency in the band (i.e., at $f_c + W/2$).

It is also interesting to note that the down-up LFM waveform has lower bounds than the up-down LFM waveform, which corroborates the observations in [42] when using similarly constructed HFM pulses. This is seen to arise from the negative correlation of the terms comprising the products $\hat{\delta}_m \bar{r}_m$ in (119) and $\rho_m \hat{\delta}_m$ in (121) for the up-down LFM as opposed to their positive correlation for the down-up pulse. The latter causes an increase in the information in these terms when they are combined across the two pulses. The former results in the minus signs seen in Table 3, which act to increase the CRLB. From a more practical perspective, this can also be explained by the highest frequencies in each LFM occurring at the beginning and end of the down-up waveform rather than in the middle as for the up-down waveform. This has the effect of increasing the variance of the temporal character of the pulse in units of periods (i.e., $\sigma_c^2$) because there are more zero crossings (i.e., shorter periods or higher frequencies) at the extremes in time.

Table 4: Pertinent time and delay parameters for the different LFM pulse pairs

| | | **Consecutive** | | **Consecutive** | | **Concurrent** | |
|---|---|---|---|---|---|---|---|
| **Parameter** | **Units** | Up | Down | Down | Up | Up | Down |
| $T_m$ | s | $T_p/2$ | $T_p/2$ | $T_p/2$ | $T_p/2$ | $T_p$ | $T_p$ |
| $\delta_m$ | s | $-T_p/2$ | 0 | $-T_p/2$ | 0 | $-T_p/2$ | $-T_p/2$ |
| $\hat{\delta}_m$ | s | $-T_p/4$ | $T_p/4$ | $-T_p/4$ | $T_p/4$ | 0 | 0 |
| $b_m$ | s | $-\frac{T_p f_c}{2W}$ | $\frac{T_p f_c}{2W}$ | $\frac{T_p f_c}{2W}$ | $-\frac{T_p f_c}{2W}$ | $-\frac{T_p f_c}{W}$ | $\frac{T_p f_c}{W}$ |
| $\sigma_d^2$ | s$^2$ | $\frac{T_p^2 f_c^2}{4W^2}\left(1-\zeta+\frac{\zeta^2}{4}\right)$ | | $\frac{T_p^2 f_c^2}{4W^2}\left(1+\zeta+\frac{\zeta^2}{4}\right)$ | | $\frac{T_p^2 f_c^2}{W^2}$ | |

### 5.4.2 X-LFM waveform

An advantage of the up-down and down-up LFM pulses is that they have constant envelopes, which allows operating the projector near its maximum source power level. When this is not a concern, projecting the up- and down-sweeping LFM pulses concurrently, with each having amplitude a factor $1/\sqrt{2}$ smaller than that for a single pulse, has some advantages. The X-LFM waveform is one in which the pulses have the same temporal and spectral support. This causes the two pulses to be weakly correlated rather than orthogonal, which makes the analysis an approximation to performance and might lead to reverberation from one pulse affecting the other. As such, it is useful to also consider concurrent projection of the pulses in the frequency bands $(f_c - W, f_c)$ and $(f_c, f_c + W)$ so they are orthogonal owing to frequency diversity, but use twice the bandwidth. Interestingly, when the expanded frequency band does not alter the individual-pulse SNRs, the velocity-estimation bounds for these two scenarios are identical[18] (i.e., they both result in the equations shown in the right-most column in Table 3). As seen in Fig. 6, the concurrently

[18] In Table 4, the values of $b_m$ for the frequency-diverse pulses are $-T_p(f_c - W/2)/W$ and $T_p(f_c + W/2)$ when the up-sweep is in the lower frequency band.

projected LFM results fall between the bounds for coherent consecutively projected up and down LFM pulses. However, the incoherent processing does not incur the factor-of-four increase in the CRLB owing to the pulse durations of the two individual pulses not being halved. When incoherent processing is employed, this result supports using concurrently projected up- and down-sweeping LFM pulses as opposed to projecting them in sequence.

### 5.5 FM-CW pulse pair

A common practice in active sonar systems is to transmit both a CW pulse and an FM pulse in the same ping [9, 10]. The CW pulse provides a high quality estimate of radial velocity and the FM pulse lends some protection when reverberation limits detection of the CW echo. Although the FM pulse by itself has difficulty with unbiased estimation of time delay when Doppler is unknown (as described in Sect. 2.4.2), it can provide a biased estimate with low variance that can be used across multiple pings to resolve the ambiguity.

When an OOI is detected by both waveforms, the techniques presented in Sect. 4 can be applied to determine how much the CW and FM pulse can benefit from each other when jointly estimating time delay and radial velocity. In the example presented in Figs. 7 and 8, an up-sweeping LFM pulse ending at frequency $f_1 = 1.9\,\text{kHz}$ was immediately followed by a CW pulse at $f_{\text{cw}} = 2\,\text{kHz}$. The LFM started at a frequency $f_0 = f_1 - W$ where the bandwidth was defined as a function of $\zeta = W/f_c$ according to

$$W = \frac{f_1}{0.5 + 1/\zeta}. \quad \text{[units: Hz]} \tag{198}$$

The two pulses are assumed to have the same duration ($T_{\text{fm}} = T_{\text{cw}} = 0.75\,\text{s}$) and SNR ($10\log_{10} S_{\text{fm}} = 10\log_{10} S_{\text{cw}} = 10\,\text{dB}$). The onset time of the reference pulse ($t_\star^{\text{tx}}$) is assumed to occur in the middle of the combined FM-CW pair.

The most common manner in which FM-CW waveforms might be employed is through an incoherent combination, such as using a radial-velocity estimate from the CW to refine estimation of the time delay from the LFM. The results seen in Fig. 7 illustrate how the bound on time-delay estimation for incoherent pulses from Sect. 4.3 (blue dashed line) comes close to the bound for the LFM by itself when Doppler is known (reddish-brown dash-dot line). However, Fig. 8 illustrates how incoherent use of the LFM pulse (blue dashed line) adds very little to the velocity estimation potential of the CW pulse by itself (gold line). Coherently combining the two pulses (solid blue line) provides only minimal improvement to radial-velocity estimation in this example until the LFM bandwidth is an appreciable fraction of its center frequency.

Where coherent combination of the pulses contributes significantly is when estimating time delay with LFM pulses that are not overly broadband (i.e., $\zeta$ is not too large). As seen in Fig. 7, combining the LFM and CW coherently tends toward the result achieved by consecutive CW pulses at 1.9 and 2 kHz (the black circle), which is itself somewhat above that achieved for simultaneous projection of the CW pulses in a comb waveform from (138). As explained for the comb waveforms, this occurs because the combined LFM-CW waveform spans the frequency band $(f_c - W/2, f_{\text{cw}})$ and it is the spread that drives performance.

Given the inherent difficulties in coherent and incoherent combination of FM and CW pulses (e.g., accounting for diverse SNRs and associating detections), the option of projecting a single

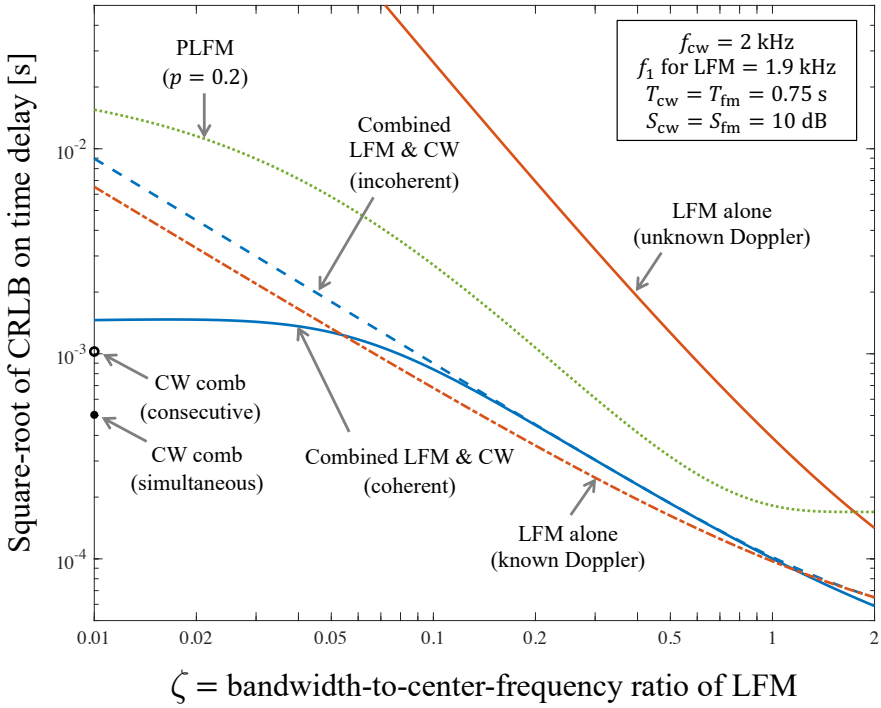


Figure 7: Square root of the CRLB for unbiased estimation of time delay when using an LFM-CW pulse pair as a function of the bandwidth-to-center-frequency ratio for the LFM.

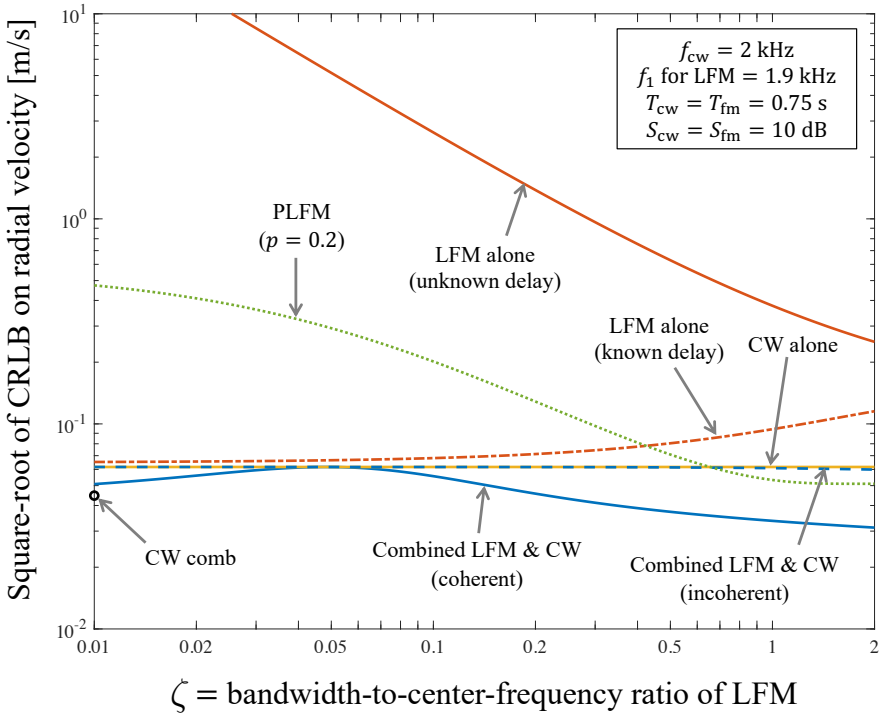


Figure 8: Square root of the CRLB for unbiased estimation of radial velocity when using an LFM-CW pulse pair as a function of the bandwidth-to-center-frequency ratio for the LFM.

pulse within the PLFM family becomes attractive. For example, consider a PLFM pulse spanning the total time and bandwidth of the FM-CW combination with a power law of $p = 0.2$. In Figs. 7 & 8, this PLFM (green dotted lines) is seen to provide better performance than the LFM alone and reasonable Doppler discrimination. Using [7, eq. 26], the loss in SNR relative to an LFM in reverberation for this pulse at these frequencies is less than 0.5 dB when $\zeta \leq 0.26$, which may be a reasonable compromise.

# 6 Summary

The focus of this report has been on performance bounds for estimating time delay and radial velocity in active sensing systems employing multiple frequency-modulated pulses. The bounds were formed under the assumption that both parameters were unknown and permitted the waveforms to be broadband. After reviewing existing results for bounds on single pulses and the use of multiple time-delay measurements to estimate radial velocity, the key multiple-pulse results were presented for the cases of coherent and incoherent echoes (i.e., when the echoes have, respectively, common or different bulk phases). Because the multiple-pulse results were presented in terms of the characteristic time-frequency parameters of the individual pulses and the times of their projection, they are straightforward to apply to diverse combinations of pulses. A number of examples were presented confirming existing lore and at times providing a greater understanding of why certain pulse combinations can provide a significant improvement in performance over their individual-pulse capabilities. These results should provide a useful tool for evaluating the accuracy with which time delay (equivalently range) and radial velocity can be estimated when using a particular set of waveforms in an active sensing system.

# References

[1] D. A. Abraham, *Underwater Acoustic Signal Processing: Modeling, Detection, and Estimation.* Springer, 2019.

[2] N. Levanon and E. Mozeson, *Radar Signals.* Wiley-Interscience, 2004.

[3] D. W. Ricker, *Echo Signal Processing.* Boston, Massachusetts: Kluwer Academic Publishers, 2003.

[4] S. D. Blunt and E. L. Mokole, "Overview of radar waveform diversity," *IEEE Aerospace and Electronic Systems Magazine*, vol. 31, no. 11, pp. 2–42, 2016.

[5] J. J. Kroszczynski, "Pulse compression by means of linear-period modulation," *Proceedings of the IEEE*, vol. 57, no. 7, pp. 1260–1266, 1969.

[6] R. A. Altes and E. L. Titlebaum, "Bat signals as optimally Doppler tolerant waveforms," *The Journal of the Acoustical Society of America*, vol. 48, no. 4, pp. 1014–1020, 1970.

[7] Y. Doisy, L. Deruaz, S. P. Beerens, and R. Been, "Target Doppler estimation using wideband frequency modulated signals," *IEEE Transactions on Signal Processing*, vol. 48, no. 5, pp. 1213–1224, May 2000.

[8] D. A. Hague, "Adaptive transmit waveform design using multitone sinusoidal frequency modulation," *IEEE Transactions on Aerospace and Electronic Systems*, vol. 57, no. 2, pp. 1274–1287, 2021.

[9] C. Rago, P. Willett, and Y. Bar-Shalom, "Detection-tracking performance with combined waveforms," *IEEE Transactions Aerospace and Electronic Systems*, vol. 34, no. 2, pp. 612–624, April 1998.

[10] D. Grimmett, "Multi-sensor placement to exploit complementary properties of diverse sonar waveforms," *9th International Conference on Information Fusion*, pp. 1–8, 2006.

[11] R. Niu, P. Willett, and Y. Bar-Shalom, "Tracking considerations in selection of radar waveform for range and range-rate measurements," *IEEE Transactions on Aerospace and Electronic Systems*, vol. 38, no. 2, pp. 467–487, 2002.

[12] M. A. Richards, J. A. Scheer, and W. A. Holm, *Principles of Modern Radar*. Raleigh, NC: SciTech Publishing, Inc., 2010.

[13] S. M. Kay, *Fundamentals of Statistical Signal Processing: Estimation Theory*. Prentice Hall PTR, 1993.

[14] D. Rife and R. Boorstyn, "Single tone parameter estimation from discrete-time observations," *IEEE Transactions on Information Theory*, vol. 20, no. 5, pp. 591–598, September 1974.

[15] A. Dogandzic and A. Nehorai, "Cramer-Rao bounds for estimating range, velocity, and direction with an active array," *IEEE Transactions on Signal Processing*, vol. 49, no. 6, pp. 1122–1137, June 2001.

[16] L. Brennan, "Angular accuracy of a phased array radar," *IRE Transactions on Antennas and Propagation*, vol. 9, no. 3, pp. 268–275, May 1961.

[17] C. E. Cook and M. Bernfeld, *Radar Signals: An Introduction to Theory and Applications*. New York: Academic Press, Inc., 1967.

[18] H. L. Van Trees, *Detection, Estimation, and Modulation Theory: Part III*. New York: John Wiley & Sons, Inc., 1971.

[19] R. Manasse, "Range and velocity accuracy from radar measurements," MIT Lincoln Laboratory, Group Report 312-26, February 3 1955.

[20] ——, "Summary of maximum theoretical accuracy of radar measurements," MITRE, Mitre Technical Series Report No. 2, April 1 1960.

[21] J. P. Ovarlez, "Cramer Rao bound computation for velocity estimation in the broad-band case using the Mellin transform," in *1993 IEEE International Conference on Acoustics, Speech, and Signal Processing*, vol. 1, 1993, pp. 273–276.

[22] T. Abatzoglou and G. Gheen, "Range, radial velocity, and acceleration MLE using radar LFM pulse train," *IEEE Transactions on Aerospace and Electronic Systems*, vol. 34, no. 4, pp. 1070–1083, 1998.

[23] P. Stinco, M. S. Greco, F. Gini, and M. Rangaswamy, "Ambiguity function and Cramer–Rao bounds for universal mobile telecommunications system-based passive coherent location systems," *IET Radar, Sonar & Navigation*, vol. 6, no. 7, pp. 668–678, August 2012.

[24] P. M. Morse and K. U. Ingard, *Theoretical Acoustics*. Princeton University Press, 1968.

[25] C. Shi, S. Salous, F. Wang, and J. Zhou, "Cramer-Rao lower bound evaluation for linear frequency modulation based active radar networks operating in a Rice fading environment," *Sensors*, vol. 16, no. 12, pp. 1–17, 2016.

[26] P. Swerling, "Parameter estimation for waveforms in additive Gaussian noise," *Journal of the Society for Industrial and Applied Mathematics*, vol. 7, no. 2, pp. 152–166, 1959.

[27] J. Ziv and M. Zakai, "Some lower bounds on signal parameter estimation," *IEEE Transactions on Information Theory*, vol. 15, no. 3, pp. 386–391, 1969.

[28] M. A. Ainslie, M. B. Halvorsen, and S. P. Robinson, "A terminology standard for underwater acoustics and the benefits of international standardization," *IEEE Journal of Oceanic Engineering*, vol. 47, no. 1, pp. 179–200, Jan 2022.

[29] R. J. Fitzgerald, "Effects of range-Doppler coupling on chirp radar tracking accuracy," *IEEE Transactions on Aerospace and Electronic Systems*, vol. AES-10, no. 4, pp. 528–532, 1974.

[30] S. Kramer, "Doppler and acceleration tolerances of high-gain, wideband linear FM correlation sonars," *Proceedings of the IEEE*, vol. 55, no. 5, pp. 627–636, May 1967.

[31] A. Stuart and J. K. Ord, *Kendall's Advanced Theory of Statistics*, 5th ed. New York: Oxford University Press, 1991, vol. 2.

[32] E. W. Barankin, "Locally best unbiased estimates," *Annals of Mathematical Statistics*, vol. 20, no. 4, pp. 447–501, 1949.

[33] H. Cox, "Fundamentals of bistatic active sonar," in *Underwater Acoustic Data Processing, NATO Science Series E*, Y. T. Chan, Ed. Kluwer Academic Publishers, 1989, pp. 3–24.

[34] G. Strang, *Linear Algebra and its Applications*, 3rd ed. San Diego: Harcourt Brace Jovanovich, Publishers, 1988.

[35] X. Song, P. Willett, and S. Zhou, "Range bias modeling for hyperbolic-frequency-modulated waveforms in target tracking," *IEEE Journal of Oceanic Engineering*, vol. 37, no. 4, pp. 670–679, Oct 2012.

[36] J. J. Murray, "On the doppler bias of hyperbolic frequency modulation matched filter time of arrival estimates," *IEEE Journal of Oceanic Engineering*, pp. 1–5, 2018.

[37] H. Cox and H. Lai, "Geometric comb waveforms for reverberation suppression," in *Proceedings of 1994 28th Asilomar Conference on Signals, Systems and Computers*, vol. 2, 1994, pp. 1185–1189.

[38] B. K. Newhall, "Continuous reverberation response and comb spectra waveform design," *IEEE Journal of Oceanic Engineering*, vol. 32, no. 2, pp. 524–532, 2007.

[39] D. A. Hague, "Adaptive comb waveform design for reverberation suppression," in *OCEANS 2022, Hampton Roads*, 2022, pp. 1–8.

[40] J. Alsup, "Comb waveforms for sonar," in *Conference Record of the Thirty-Third Asilomar Conference on Signals, Systems, and Computers (Cat. No.CH37020)*, vol. 2, 1999, pp. 864–869.

[41] J. R. Bates, S. M. Murphy, B. H. Maranda, and D. A. Abraham, "Signal-to-reverberation ratio comparison of linear frequency modulated continuous active sonar and pulsed active sonar," *IEEE Journal of Oceanic Engineering*, vol. 46, no. 2, pp. 654–664, 2021.

[42] F. Wang, S. Du, W. Sun, Q. Huang, and J. Su, "A method of velocity estimation using composite hyperbolic frequency-modulated signals in active sonar," *Journal of the Acoustical Society of America*, vol. 141, no. 5, pp. 3117–3122, May 2017.

[43] S. M. Kay, *Fundamentals of Statistical Signal Processing: Detection Theory.* Prentice Hall PTR, 1998.

# A FIM terms for multiple orthogonal pulses

Suppose that the $m$th pulse of $M$ has duration $T_m$ [units: s], bandwidth $W_m$ [units: Hz], center frequency $f_{cm}$ [units: Hz], and is projected with onset time $t_m^{\text{tx}}$ [units: s]. Let the characteristic time-frequency parameters of the $m$th pulse be represented with a subscript $m$ (e.g., $\bar{f}_m$ or $\sigma_{c_m}^2$).

From the definitions in Table 2 (pg. 30), recall that $t_m$ was the arrival time of the $m$th echo, $t_\star$ the arrival time of the echo from the reference pulse, and $\tau_\star = t_\star - t_\star^{\text{tx}}$ was the delay being estimated. To exploit the waveform definitions and characteristic time-frequency parameters presented in Sect. 2.3, the arrival time of the center of the $m$th pulse needs to be defined in terms of the parameters being estimated (i.e., $\tau_\star$ and $\eta$). If the development of (74) is repeated using $\hat{\delta}_m$ in place of $\delta_m$, this is seen to be

$$\hat{t}_m = t_\star + \frac{\hat{\delta}_m}{\eta} \quad \text{[units: s]}, \tag{A1}$$

where

$$\hat{\delta}_m = \delta_m + \frac{T_m}{2} \quad \text{[units: s]} \tag{A2}$$

is the delay between transmission of the center of the $m$th pulse and the onset of the reference pulse (recall $\delta_m = t_m^{\text{tx}} - t_\star^{\text{tx}}$ was the delay between the onset times).

The $m$th echo is then represented by extending (5) to

$$\tilde{u}_m(t) = A_m e^{j\psi_m} \mathring{s}_m\big(\eta[t - \hat{t}_m]\big)\, e^{-j2\pi f_{cm} t}, \tag{A3}$$

where the bulk phase ($\psi_m$) is initially assumed to be different across the echoes and the analytic function $\mathring{s}_m(t)$ is assumed to be centered in time about $t = 0\,\text{s}$, as was done in Sect. 2.3. Comparing (5) and (A3), it is clear that the difference between the analysis presented here and the single-pulse case is the dependence of $\hat{t}_m$ on $\eta$ that is captured in (A1). As will be seen, this has an impact on the FIM entries related to $\eta$.

Suppose the $M$ pulses are mutually orthogonal so

$$\int_{-\infty}^{\infty} \mathring{s}_m^*\big(t - \hat{t}_m^{\text{tx}}\big)\, \mathring{s}_n\big(t - \hat{t}_n^{\text{tx}}\big)\, \mathrm{d}t = 0 \;\text{ for }\; m \neq n. \tag{A4}$$

This is commonly achieved through diversity in time or frequency, but can also be attained when the pulses occupy the same time-frequency space. The measured data can then be modeled by extending (4) to the sum

$$\tilde{x}(t) = \sum_{m=1}^{M} \tilde{u}_m(t) + \tilde{v}_m(t), \tag{A5}$$

where $\tilde{v}_m(t)$ is the complex envelope of the noise affecting the $m$th echo after projection onto the time-frequency space of the $m$th signal. For example, when the pulses are projected concurrently in non-overlapping frequency bands, $\tilde{v}_m(t)$ can be formed by bandpass filtering to the frequency band of the $m$th signal before basebanding. The orthogonality between the pulses implies the noise in (A5) is uncorrelated from pulse to pulse and therefore independent if it is Gaussian distributed.

The scaling convention used in [1, Sect. 8.5.3] for frequency-modulated waveforms required the discrete-time replica to have unit energy (recall footnote 7 (pg. 10)) when sampled at $\mathrm{d}t = 1/W_m$,

$$\sum_n |\mathring{s}_m(n\,\mathrm{d}t)|^2 = 1. \tag{A6}$$

This in turn yields

$$\int_{-\infty}^{\infty} |\mathring{s}_m(t)|^2\,\mathrm{d}t \approx \frac{1}{W_m} \tag{A7}$$

and

$$S_m^{\mathrm{d}} = \frac{A_m^2}{\lambda_m} \quad \text{[unitless]} \tag{A8}$$

for the SNR after coherent detection processing of the $m$th pulse, where $\lambda_m$ is the variance of the complex envelope of the noise, $\tilde{v}_m(t)$.

The steps described in Sect. 2.2.1 (in particular after (5)) for constructing a vector $\mathbf{x}$ representing the measurements can be extended to this multiple-pulse scenario by simply stacking the measurements from each pulse, where those that are contemporaneous in time are first projected onto the time-frequency space of the respective signal. The independence of the noise between pulses, the assumption of a flat noise power spectral density within the band, and setting the sampling rate for each pulse equal to its bandwidth implies the covariance matrix of $\mathbf{x}$ is a diagonal matrix with each pulse's entries equal to the variance of its noise ($\lambda_m$).

Assuming the parameters $\theta_i$ and $\theta_j$ only enter the mean of $\mathbf{x}$, as is the case for all of the echo parameters in the deterministic-signal model, their FIM entry is formed from the first term in (8). Using the above characterization of the noise covariance matrix for $M$ orthogonal pulses produces the FIM entry

$$\mathrm{FIM}_{\theta_i,\theta_j} \approx \sum_{m=1}^{M} \frac{2W_m}{\lambda_m} \mathrm{Real}\left\{ \int_{-\infty}^{\infty} \frac{\partial \tilde{u}_m^*(t)}{\partial \theta_i} \frac{\partial \tilde{u}_m(t)}{\partial \theta_j}\,\mathrm{d}t \right\}, \tag{A9}$$

which is simply the sum over the $M$ individual-pulse FIM entries. After accounting for the dependence of $\hat{t}_m$ on $\eta$, the multiple-pulse FIM entries can be described in terms of the individual-pulse characteristic time-frequency parameters. The following sections present the FIM terms for the two cases of coherency and incoherency between echoes.

## A.1 Coherent echoes

When the bulk phase is the same across the pulses (i.e., $\psi_m = \psi$ is unknown but constant), the FIM can be described using the single-pulse form found in (27), a total SNR of

$$S_{\mathrm{tot}}^{\mathrm{d}} = \sum_{m=1}^{M} S_m^{\mathrm{d}} \quad \text{[unitless]}, \tag{A10}$$

and characteristic time-frequency parameters defined over the multiple pulses, which were presented in (116)–(120). A brief derivation of these results is presented here.

Following the single-pulse derivations of the FIM entries for $(\tau_\star, \psi)$ and $(\tau_\star, \tau_\star)$ in [1, Sect. 8.5.3], it is straightforward to show that (A9) results in a weighted sum over the single-pulse terms for $\bar{f}$ and $P_f$. For example, the latter has the form

$$P_f = \frac{1}{S^{\mathrm{d}}_{\mathrm{tot}}} \sum_{m=1}^{M} S^{\mathrm{d}}_m P_{f_m} \quad \text{[units: Hz}^2\text{]}. \tag{A11}$$

As mentioned above, the terms entailing $\eta$ must account for how it enters into $\hat{t}_m$, which differs from the single-pulse scenario. From (A1), it can be seen that

$$\frac{\partial \hat{t}_m}{\partial \eta} = \frac{-\hat{\delta}_m}{\eta^2} \quad \text{[units: s]}. \tag{A12}$$

The derivative of the complex envelope of the $m$th echo with respect to Doppler scale is then

$$\frac{\partial \tilde{u}_m(t)}{\partial \eta} = \frac{\partial(\eta[t-\hat{t}_m])}{\partial \eta} \frac{\mathring{s}'_m\big(\eta[t-\hat{t}_m]\big)}{\mathring{s}_m\big(\eta[t-\hat{t}_m]\big)} \tilde{u}_m(t) \tag{A13}$$

$$= \left[ t - \hat{t}_m + \frac{\hat{\delta}_m}{\eta} \right] \frac{\mathring{s}'_m\big(\eta[t-\hat{t}_m]\big)}{\mathring{s}_m\big(\eta[t-\hat{t}_m]\big)} \tilde{u}_m(t) \tag{A14}$$

$$\approx j2\pi(t-t_\star) f_m(t-\hat{t}_m) \tilde{u}_m(t), \tag{A15}$$

where the last line sets $\eta$ to its nominal value of one and exploits

$$\frac{\mathring{s}'_m(t)}{\mathring{s}_m(t)} \approx j2\pi f_m(t) \tag{A16}$$

from [1, pg. 550, eq. 8.278] for frequency-modulated waveforms with slowly varying amplitudes.

Using (A15) with the derivatives with respect to $\tau_\star$ and $\psi$ and exploiting (A7) for waveforms with a constant envelope, the terms in the FIM can be described using an integral with the form

$$G_m(k,l) = \frac{W_m}{T_m \lambda_m} \int_{-\infty}^{\infty} (t-t_\star)^k f_m^l(t-\hat{t}_m) |\tilde{u}_m(t)|^2 \, \mathrm{d}t \tag{A17}$$

$$= \frac{S^{\mathrm{d}}_m}{T_m} \int_{-T_m/2}^{T_m/2} (t+\hat{\delta}_m)^k f_m^l(t) \, \mathrm{d}t \quad \text{[units: Hz}^{l-k}\text{]} \tag{A18}$$

where $k$ and $l$ are integers taking on values of 0, 1 or 2. For example, (A11) is obtained from

$$P_f = \frac{1}{S^{\mathrm{d}}_{\mathrm{tot}}} \sum_{m=1}^{M} G_m(0,2) \quad \text{[units: Hz}^2\text{]}. \tag{A19}$$

The terms for which $k = 1$ or 2 produce

$$\bar{c} = \frac{1}{S^{\mathrm{d}}_{\mathrm{tot}}} \sum_{m=1}^{M} G_m(1,1) = \frac{1}{S^{\mathrm{d}}_{\mathrm{tot}}} \sum_{m=1}^{M} S^{\mathrm{d}}_m \Big( \bar{c}_m + \hat{\delta}_m \bar{f}_m \Big) \quad \text{[unitless]}, \tag{A20}$$

$$P_c = \frac{1}{S^{\mathrm{d}}_{\mathrm{tot}}} \sum_{m=1}^{M} G_m(2,2) = \frac{1}{S^{\mathrm{d}}_{\mathrm{tot}}} \sum_{m=1}^{M} S^{\mathrm{d}}_m \Big( P_{c_m} + 2\hat{\delta}_m \bar{r}_m + \hat{\delta}^2_m P_{f_m} \Big) \quad \text{[unitless]}, \tag{A21}$$

and

$$\bar{r} = \frac{1}{S^{\mathrm{d}}_{\mathrm{tot}}} \sum_{m=1}^{M} G_m(1,2) = \frac{1}{S^{\mathrm{d}}_{\mathrm{tot}}} \sum_{m=1}^{M} S^{\mathrm{d}}_m \Big( \bar{r}_m + \hat{\delta}_m P_{f_m} \Big) \quad \text{[units: Hz]}, \tag{A22}$$

which were presented in Sect. 4.2.

## A.2 Incoherent echoes

The FIM result found in (121) for pulses having different bulk phase terms is derived in this section. The $M+2$ coupled and unknown parameters for this problem are

$$\boldsymbol{\theta} = [\tau_\star \;\; \eta \;\; \psi_1 \cdots \psi_M]^T, \tag{A23}$$

where $\psi_m$ is the bulk phase from the $m$th echo. The matrix in (121) is the two-by-two sub-matrix formed from the $(\tau_\star, \eta)$ elements of the inverse FIM for $\boldsymbol{\theta}$. This can be obtained by describing the FIM for $\boldsymbol{\theta}$ as comprising a two-by-two block-matrix partition,

$$\mathrm{FIM}_{\boldsymbol{\theta}} = \begin{bmatrix} \mathbf{A} & \mathbf{B} \\ \mathbf{C} & \mathbf{D} \end{bmatrix} \tag{A24}$$

where $\mathbf{A}$ is a 2-by-2 matrix, $\mathbf{B} = \mathbf{C}^T$ is 2-by-$M$, and $\mathbf{D}$ is $M$-by-$M$. Using the formula for the inverse of a partitioned matrix found on [43, pg. 535], the 2-by-2 upper-left sub-matrix of the inverse FIM is

$$\mathbf{G} = \big( \mathbf{A} - \mathbf{B}\mathbf{D}^{-1}\mathbf{C} \big)^{-1}. \tag{A25}$$

The CRLBs for time-delay and velocity estimation are obtained from the diagonal elements of $\mathbf{G}$.

The elements of the FIM for this problem are an extension of those found in (27) to multiple pulses, similar to the development in App. A.1, but accounting for different phases. Because all of the pulses contribute to estimating $\tau_\star$ and $\eta$ in a manner that does not depend on the value of $\psi_m$, the two-by-two sub-matrix $\mathbf{A}$ has the same form as that implied by using (117), (119), and (120) in (27),

$$\mathbf{A} = 8\pi^2 \sum_{m=1}^{M} S^{\mathrm{d}}_m \begin{bmatrix} P_{f_m} & -\bar{r}_m - \hat{\delta}_m P_{f_m} \\ -\bar{r}_m - \hat{\delta}_m P_{f_m} & P_{c_m} + 2\hat{\delta}_m \bar{r}_m + \hat{\delta}^2_m P_{f_m} \end{bmatrix} \tag{A26}$$

where $\hat{\delta}_m = \delta_m + T_m/2$ [units: s] represents the difference between the time at which the center of the $m$th pulse is transmitted and the onset of the reference pulse. To describe the other sub-matrices in (A24), it is helpful to define the following vector and matrix terms. Place the SNRs of the individual pulses (i.e., ($S^{\mathrm{d}}_m$ for $m = 1, \ldots, M$) in the vector $\mathbf{s}$ and use them to form the diagonal matrix $\mathbf{S}$. Similarly use the delays $\hat{\delta}_m$ for $m = 1, \ldots, M$ to form the diagonal matrix $\boldsymbol{\Delta}$. Define the vectors $\mathbf{f}$, $\mathbf{p}_f$, $\mathbf{c}$, $\mathbf{p}_c$, and $\mathbf{r}$ as containing, respectively, $\bar{f}_m$, $P_{f_m}$, $\bar{c}_m$, $P_{c_m}$, and $\bar{r}_m$ for $m = 1, \ldots, M$. This allows describing (A26) as

$$\mathbf{A} = 8\pi^2 \begin{bmatrix} \mathbf{s}^T \mathbf{p}_f & -\mathbf{s}^T(\mathbf{r} + \boldsymbol{\Delta}\mathbf{p}_f) \\ -\mathbf{s}^T(\mathbf{r} + \boldsymbol{\Delta}\mathbf{p}_f) & \mathbf{s}^T\big(\mathbf{p}_c + 2\boldsymbol{\Delta}\mathbf{r} + \boldsymbol{\Delta}^2\mathbf{p}_f\big) \end{bmatrix}. \tag{A27}$$

The columns of $\mathbf{B}^T$ or $\mathbf{C}$ are formed by separate entries for each bulk phase. This essentially spreads out the terms seen in the sums in (116) and (118) into the $M$ rows of these matrics,

$$\mathbf{C} = \mathbf{B}^T = 4\pi \begin{bmatrix} -\mathbf{Sf} & \mathbf{S}(\mathbf{c} + \boldsymbol{\Delta}\mathbf{f}) \end{bmatrix}. \tag{A28}$$

The $m$th row of $\mathbf{C} = \mathbf{B}^T$ can also be obtained using the integral in (A18),

$$\{\mathbf{C}\}_{m\text{th row}} = 4\pi[-G_m(0,1) \quad G_m(1,1)]. \tag{A29}$$

Because the pulses are orthogonal and the background is assumed to be Gaussian distributed, the noise occluding the echo from one pulse can be assumed to be independent of that affecting another. This causes the dimension-$M$ matrix $\mathbf{D}$ to be diagonal, formed from the terms

$$\{\mathbf{D}\}_{m,m} = 2G_m(0,0) = 2S_m^{\mathrm{d}} \tag{A30}$$

for $m = 1, \ldots, M$. In matrix notation, $\mathbf{D} = 2\mathbf{S}$.

Using these matrix-vector notations to construct the FIM for $\boldsymbol{\theta}$ results in

$$\mathrm{FIM}_{\boldsymbol{\theta}} = 8\pi^2 \begin{bmatrix} \mathbf{s}^T\mathbf{p}_f & -\mathbf{s}^T(\mathbf{r} + \boldsymbol{\Delta}\mathbf{p}_f) & \frac{-1}{2\pi}\mathbf{f}^T\mathbf{S} \\ -\mathbf{s}^T(\mathbf{r} + \boldsymbol{\Delta}\mathbf{p}_f) & \mathbf{s}^T\left(\mathbf{p}_c + 2\boldsymbol{\Delta}\mathbf{r} + \boldsymbol{\Delta}^2\mathbf{p}_f\right) & \frac{1}{2\pi}(\mathbf{c} + \boldsymbol{\Delta}\mathbf{f})^T\,\mathbf{S} \\ \frac{-1}{2\pi}\mathbf{S}\mathbf{f} & \frac{1}{2\pi}\mathbf{S}(\mathbf{c} + \boldsymbol{\Delta}\mathbf{f}) & \frac{1}{4\pi^2}\mathbf{S} \end{bmatrix}. \tag{A31}$$

Note that when there is only one pulse, all the terms containing $\boldsymbol{\Delta}$ or $\boldsymbol{\Delta}^2$ are zero and (A31) simplifies to (27). The partitioned-matrix inverse formula yielding (A25) can then be employed to describe the upper-left 2-by-2 partition of the inverse FIM as

$$\mathbf{G} = \frac{1}{8\pi^2} \begin{bmatrix} \mathbf{s}^T\mathbf{p}_f - \mathbf{f}^T\mathbf{S}\mathbf{f} & -\mathbf{s}^T(\mathbf{r} + \boldsymbol{\Delta}\mathbf{p}_f) + \mathbf{f}^T\mathbf{S}\mathbf{c} + \mathbf{f}^T\mathbf{S}\boldsymbol{\Delta}\mathbf{f} \\ -\mathbf{s}^T(\mathbf{r} + \boldsymbol{\Delta}\mathbf{p}_f) & \mathbf{s}^T\left(\mathbf{p}_c + 2\boldsymbol{\Delta}\mathbf{r} + \boldsymbol{\Delta}^2\mathbf{p}_f\right) - \mathbf{c}^T\mathbf{S}\mathbf{c} \\ \quad +\mathbf{f}^T\mathbf{S}\mathbf{c} + \mathbf{f}^T\mathbf{S}\boldsymbol{\Delta}\mathbf{f} & \quad -2\mathbf{f}^T\boldsymbol{\Delta}\mathbf{S}\mathbf{c} - \mathbf{f}^T\boldsymbol{\Delta}\mathbf{S}\boldsymbol{\Delta}\mathbf{f} \end{bmatrix}^{-1}. \tag{A32}$$

Collapsing the vector inner products and matrix-vector quadratic and bi-linear forms into sums results in the simplification,

$$\mathbf{G} = \frac{1}{8\pi^2}\left\{\sum_{m=1}^{M} S_m^{\mathrm{d}} \begin{bmatrix} \sigma_{f_m}^2 & -\sigma_{f_m}\sigma_{c_m}\rho_m - \hat{\delta}_m\sigma_{f_m}^2 \\ -\sigma_{f_m}\sigma_{c_m}\rho_m - \hat{\delta}_m\sigma_{f_m}^2 & \sigma_{c_m}^2 + 2\hat{\delta}_m\rho_m\sigma_{f_m}\sigma_{c_m} + \hat{\delta}_m^2\sigma_{f_m}^2 \end{bmatrix}\right\}^{-1} \tag{A33}$$

as was presented in (121).